Effects of Microstructural Properties on Structural Color of Self-Assembled Colloidal Crystals

by

Tianyu Liu

A dissertation submitted in partial fulfillment
of the requirements for the degree of
Doctor of Philosophy
(Macromolecular Science and Engineering)
in The University of Michigan
2021

Doctoral Committee:

Professor Michael J. Solomon, Chair
Professor Sharon C. Glotzer
Professor Jay L. Guo
Professor Jinsang Kim

Tiany Liu

ltianyu@umich.edu

ORCID iD: 0000-0002-0093-8993

Dedication

To my mother, father, and Haozhu, the start of our new family. They have always supported me.

Acknowledgments

Firstly, I would like to thank my research advisor, Professor Mike Solomon. Mike has always been very supportive and patient about my professional development as a researcher. He has ensured that we maintained the high quality of research works and gave me the freedom to explore different directions. I have learned so much from him to grow as a scientist and develop my technical skills. Mike is also very compassionate and cared deeply about my career development after graduation. I am very appreciative of everything he has done for me, from allowing me to conducting industrial research, to encouraging me to develop my soft skills. I feel very fortunate to be his student. Thank you very much Mike for being such a great advisor!

I also want to thank my committee members, Prof. Sharon Glotzer, Prof. Jay Guo, and Prof. Jinsang Kim. Prof. Glotzer provided valuable technical insights into how simulation could support the experiments. Collaborations with Prof. Glotzer and her students yielded systematic research findings in our three projects. Prof. Guo shared invaluable knowledge of optical materials and measurement. The structural color research of his group gave me opportunities to learn more cutting-edge techniques in person. Prof. Kim taught me polymer knowledge through courses and shared resources in the polymer field. As the director of our Macro department, Prof. Kim provided us lots of learning opportunities both inside and outside of science.

I would also like to thank my research collaborators at the University of Michigan and during my industrial internship. Bryan VanSaders produced exciting MD simulation results in our

two collaboration projects. I have enjoyed discussing with him about our research and working together on the course project. Tianyu Liu is very helpful on the discoid project in setting up the optical instrument and helping with the measurements. He has the same name as me, and it has been a pleasure to collaborate with him. Fengyi Gao provided the MC simulation results quickly, which speeded up the progress of our discoid project. I have enjoyed talking with her about inside and outside of research, even just virtually. My BASF manager Qingling Zhao gave me opportunities to learn automotive coatings for structural color application. My Honeywell manager Hayim Abrevaya offered me the opportunity to continue to work on sustainable materials after my graduation.

I am also thankful for my labmates in the Solomon group – Yanliang Liu, Maria Ma, Yufei Wei, Keara Saud, Peng-Kai Kao, Joanne Beckwith, Mahesh Ganesan, Megan Szakasits, Joseph Ferrar, and Rachael Hamilton. Thank you for the friendly and supportive group environment. Although we worked on different research directions, we understood and encouraged each other about the ups and downs of research projects. During the almost six years in the group, I am very appreciative of the friendship of different members at different stages, where some graduated earlier than me, and some joined the group later than me.

Finally, I would like to thank my family. My mother and father have always supported me with the best resources they can provide. Their encouragement and compliment made me confident to pursue whatever I like. Making them proud of me has also motivated me to become better and better. In addition, I am very thankful to my partner Haozhu Wang. He has accompanied me since we were undergraduates. I greatly appreciate his sacrifice when he transferred to UMich and relocated to the Chicago area with me. His love and support make us ready to start as a family of husband, wife, and our dog Lucky.

Table of Contents

List of Figures

List of Tables

Abstract

This dissertation examines the relationship between colloidal microstructural properties and structural color, to guide the design of optical materials. Colloidal microstructures can interact with light to produce structural color, which is not prone to environmental degradation. The high stability of structural color provides great potential for optical applications such as coatings and displays. Previous studies in structural color from colloidal systems have primarily focused on controlling structural color wavelength by changing the dielectric periodicity of the material. However, the connection between colloidal microstructural properties and structural color reflectivity – particularly its magnitude – remains unclear. In this dissertation, we systematically and quantitatively investigate the effects of crystal thickness, defect density and structure, irregularity of particle size, and particle shape on structural color by experiment and simulation. The relationships can be applied to designing novel materials with tailored structural color properties.

First, we report how film thickness, defect density, and defect type in colloidal crystals quantitatively affect their structural color reflectivity. Colloidal crystals with different thicknesses are fabricated by self-assembling monosized polystyrene microspheres via solvent evaporation. We find that the structural color reflectivity increases as a function of the crystal thickness, until a plateau is reached at 78.8 ± 0.9%. We also model crystals via molecular dynamics and simulate their reflection spectra by the finite-difference time-domain method. The simulation results show

that the reduction in reflectivity scales with increased defect density and that stacking fault tetrahedra are most efficient in disrupting structural color. These findings can guide the efficient design of structural color materials and support defect engineering in colloidal crystals.

Second, we evaluate the role of irregular-sized spherical particles in determining crystal quality and structural color reflectivity. By evaporative self-assembly and molecular dynamics simulation, we control the volume fraction of irregular-sized particles – by choosing particles that are either larger or smaller than the base colloids comprising the self-assembled crystals. Then we quantify crystal quality from analysis of diffraction patterns obtained by Fast Fourier transform of the scanning electron microscope images. We find that small irregular particles are more detrimental to crystal quality and structural color reflectivity than large irregular particles. When incorporated with 10 vol% of irregular particles, the reflectivity of crystal films with large (small) irregular particles decreases by 18.4% ± 5.6% (27.5 ± 5.8%), and crystal quality reduced by 40.0 ± 4.5% (48.8 ± 6.0%). This study can be applied to predict the level of irregular-sized particles that can be tolerated in structural color materials at a specified reflectivity.

Finally, we explore the effect of particle anisotropy on structural color reflection from discoid packings. We prepare discoidal particles that vary in shape anisotropy and particle size by uniaxial compression of spheres. Discoids are self-assembled by evaporation into dense discoid packings, which exhibit non-iridescent structural colors. This coloration is a combination of backscattering and multilayer reflection. We find that the multilayer reflection displays progressively smaller peak height and broader bandwidth as the discoids become more anisotropic. In addition, Monte Carlo simulation is used to produce comparable discoid structures. The density profiles of the simulated structures in the wall-normal direction demonstrate that discoids with a higher shape anisotropy assemble into more disordered structures, which explains the less intense

structural color. Our findings demonstrate that tunable geometries of discoids increase the opportunities for spectral control of non-iridescent structural color materials.

Chapter 1 Introduction

1.1 Structural Color

Color plays an important role in our daily life, especially its aesthetic and signal functions. To color materials, pigments or dyes are usually used to selectively absorb specific wavelengths of light to achieve coloration. However, colors from pigments or dyes fade out due to environmental degradation such as photobleaching and oxidation [1]. By contrast, some colors in natural creatures such as butterflies [2], beetles [3], and cephalopods [4] do not fade under long-time sunlight exposure or at high temperatures. This kind of color, termed structural color, originates from the constructive interference of light on nanostructures units of creatures [5]. Structural color can be either iridescent or non-iridescent [6]. Iridescent structural color, which changes with viewing angle, is produced by a periodic nanostructure. For example, opals are close-packed crystals of silica spherical nanoparticles [7]. Non-iridescent structural color also exists. An example would be the beetle *A. graafi.* whose coloration raises from random arrays of anisotropic chitin nanoparticles [8].

Generally, the wavelength of iridescent structural color is determined by the Bragg equation [9], [10]:

$$m\lambda = 2d_{hkl}\sqrt{{n_{eff}}^2 - sin^2\theta} \quad (1)$$

Where m is the diffraction order, λ is the reflected wavelength of light, d_{hkl} is interlayer spacing along the $[hkl]$ direction, n_{eff} is the mean refractive index of crystals (composed of nanoparticles

and medium), and θ is the angle of incident light relative to the normal. Thus, different structural colors can be achieved by varying viewing angles, interlayer spacing, or materials with different refractive indexes.

The unique optical properties of structural color offers great potential for a variety of applications such as long-lasting coatings [11]–[13], sensors [14], [15], inks [16], [17], anticounterfeiting patches [18], [19], filters [20], and displays [21]. Compared with pigments, the manufacturing of structural color materials involves less toxic chemicals and uses more biocompatible materials [22]–[24].

1.2 Colloidal Particles and Self-Assembly

To mimic nature's strategies for structural color, scientists have synthesized colloidal particles that are analogues of biological building blocks. Colloids are microscopic particles ranging in size from 5 nm to 5 μm [25]. This range covers the length scales required for structural color – which is about half the wavelength of visible light, which ranges from about 380 nm to 750 nm [26]. Some common colloidal materials include silica, polystyrene, and poly(methyl methacrylate), which are synthesized by different approaches such as hydrolysis of alkyl silicates [27], suspension polymerization [28], and dispersion polymerization [29]. Polymeric colloidal particles, consisting of entangled and crosslinked polymer networks, can be synthesized in both spherical and anisotropic shapes, which offers great potential for approaching the building blocks observed in nature.

Colloidal particles can self-assemble into ordered structures by a variety of methods such as evaporation [9], electrophoretic deposition [30], sedimentation [31], and dipping deposition [32]. One of the simplest, most cost-effective, and widely used self-assembly methods is evaporation.

As the solvent evaporates, the capillary force drags the colloidal particles to form stable structures with the lowest surface energy [33],[34]. As a result, monodisperse spherical colloids pack into close-packed crystals with superior quality, which is the entropically favorable configuration [35]. Another significant advantage of evaporative self-assembly over other colloidal assembly methods is that it can produce very thick crystal film by tuning the volume fraction of particle suspension before evaporation.

Recent studies have demonstrated that colloidal particles and evaporative assembly methods provide controllable ways to produce structural color with a specific wavelength. However, the correlations between structural color reflectivity and colloidal crystal quality remain unclear. For colloidal systems of anisotropic particles, their orientation freedom may favor more disordered structures [36]. Among experimentally accessible anisotropic particles, the discoid microstructure and its structural color are less understood. The tunable aspect ratio of the discoid particles can be potentially used as an additional parameter to develop structure color.

1.3 Defects in Colloidal Crystals

Most colloidal crystals in nature and artificial systems contain intrinsic defects, which are caused by non-ideal conditions during the self-assembly process [37],[38]. Some levels of defects also occur even under conditions of equilibrium self-assembly. Colloidal crystals produced from hard spheres are theoretically expected to form the face-centered-cubic (fcc) phase with a low defect density. However, the very small difference between hexagonal close-packed (hcp) packings and fcc packings results in polycrystalline structures, which contain some planar faults [39], [40]. Moreover, irregularly sized particles introduced into the system by contamination or due to polydisperse particles produced during synthesis also cause defects in the self-assembled

colloidal crystals. Especially during evaporation, the loss of the solvation layer surrounding colloidal particles leads to shrinkage in the packing and thus generates microcracks [41]. Other commonly observed defects include vacancies and stacking fault tetrahedra [42], [43]. Understanding the effects of these intrinsic defects on colloidal crystals and structural color is critical to engineer colloidal crystals for optimal structural color applications. There is a gap in the literature because this question has not yet been the subject of investigation.

1.4 Thickness of Colloidal Crystals

Film thickness is an important parameter in engineering optical coatings. There have been several studies that investigated the thickness dependence of the stop band in the transmission spectra of periodic dielectric media [44], [45]. However, a systematical and quantitative study of correlating colloidal crystal thickness and structural color reflectivity has been lacking. Colloidal crystal layers without defects are of interest to compare with multilayer reflective materials. The reflectivity (R) of multilayer material can be approximated given by [46]:

$$R = [\frac{n_0(n_2)^{2N} - n_S(n_1)^{2N}}{n_0(n_2)^{2N} + n_s(n_1)^{2N}}]^2 \quad (2)$$

Where n_0, n_1, n_2 and n_s are the reflective index of the originating medium, the alternating sequence of high and low dielectric layers, and the terminating medium; N is the number of pairs of high and low dielectric layers. The multilayer reflection theory captures the reflectivity as a function of the number of layers. Thus, control over the number of layers or thickness of colloidal crystals may be valuable to tune structural color reflectivity.

1.5 Microstructure Characterization

Scanning electron microscope (SEM) is one of the most commonly used instruments to image colloid microstructures in which the particle scale is on the micrometer and submicrometer scale. The examined area is irradiated by a focused electron beam, and then signals are produced to show the surface of the specimen [47]. To increase the conductivity of the polymer specimen, a thin layer of gold is needed to sputter on the surfaces before taking SEM images. SEM is a useful characterization tool to measure the sizes of colloidal particles and inspect the microstructure from top views and cross sections of assembled structures. SEM images can be analyzed by imaging process software such as Fiji for conjugates Fast Fourier Transform (FFT) images. The spatial information in SEM images is converted into a power spectrum to quantify crystal quality.

1.6 Structural Color Measurement

Structural color intensity and hue can be characterized by the peak height and peak location of reflection spectra, which can be measured by UV/Vis spectrophotometry. Reflection measurements have two common setups – specular reflectance measurement by normal incidence and total reflectance measurement using an integrating sphere. The integrating sphere setup collects all light reflected into the backward hemisphere. Thus, it includes both the specular and the diffuse reflection. Specular reflection occurs at an angle identical to the incident angle in the opposite direction [48]. Diffuse reflection refers to the light scattered in many directions [49]. The reflection spectrum measured by the integrating sphere configuration has higher reproducibility and is less affected by unintentional operation variations between different operators, such as a small misalignment of samples. By contrast, the normal incidence measurement is suitable for detecting the variability of different areas in a specimen [50].

To make the perceived structural color displayable on a screen, the reflection spectra can be further converted into International Commission on Illumination (CIE) xyY or Red Green Blue (RGB) color space. To determine color properties, the measured reflectance R(λ) can be transformed to a point in the normalized CIE xyY color space (x and y coordinates define the color hue, and the Y value is the color luminance) via color matching functions [51]. The CIE color matching functions are spectral sensitivity curves of three light detectors that numerically describe the chromatic response of the standard observer under D65 illumination [52]. Colors perceived by the human eye depend on illumination and receptor cells [53]. To further derive a displayable color image, the CIE xyY point is converted to the RGB color space using ITU-R BT.709 primaries [54] via an open-source Python package Colour-Science [55].

1.7 Computer Simulation of Colloidal Assembly

Colloidal-scale computer simulation is a powerful tool to predict self-assembled structures to validate and complement experimental results. Molecular dynamics (MD) and Monte Carlo (MC) simulations are commonly used to investigate colloidal systems. MD simulation approximates realistic dynamics of colloidal systems and the interactions between hard particles. Thus MD simulation is suitable for investigating dynamical processes [56]. By contrast, the MC simulation of colloidal crystals is efficient for studying static quantities by constructing particle configurations in the equilibrium phase. Furthermore, MC simulation can be used for the assembly of anisotropic particles because it can incorporate both positions and orientations of the particles [57]. For both MC and MD simulation, HOOMD-blue is a well-developed simulation engine designed for particles in nano-scale and colloidal-scale. The computer simulation approach is particularly useful to produce crystals containing a single type of defect, which was not feasible

by an experimental approach. In this dissertation, the use of MD and MC simulation is pursued in collaboration with Glotzer group members Bryan Vansaders and Fengyi Gao.

1.8 Finite-Difference Time-Domain Simulation

Predicting the optical properties of colloidal structures is of paramount importance for structural color design. Finite-Difference Time-Domain (FDTD) method is widely used to model how light interacts with micro- and nano-scale structures. By breaking up the structure and the spacing surrounding it into small cells, the FDTD method is used to calculate the electromagnetic field, which is time evolved according to Maxwell's equation [58]. Then the reflection spectra of the modeled structure can be obtained by Fourier transformation of the calculated electromagnetic field [59]. FDTD method can be implemented in existing codes such as commercial software Lumerical FDTD solutions.

FDTD simulation is faster and cheaper than fabricating experimental samples and making measurements, especially if there is a need to evaluate lots of designs to optimize parameters. In addition, FDTD simulation can be used to verify experimentally obtained results and understand the microstructural features that mediate the specific optical response.

1.9 Organization of the Dissertation

This dissertation explores the relationship between colloidal crystal microstructure and its structural color. We produce structural color from colloidal crystals and dense discoid packings by evaporative self-assembly of colloidal spheres and discoids, respectively. By utilizing experiment and simulation approaches, we systematically and quantitatively investigated the effects of colloidal crystal thickness, defects, particles of irregular size, and particle shape on structural color.

In chapter 2, we examine how crystal thickness and different kinds of defects in colloidal crystals quantitatively affect structural color. We fabricate colloidal crystals of monosized polystyrene spheres by evaporation. The crystal thickness is varied by controlling the initial volume fraction of the colloidal suspension. By measuring crystal film thicknesses by profilometer and reflection spectra by UV/Vis spectrophotometer, we find that structural color reflectance increases rapidly from a small thickness to a critical thickness and then reaches a plateau value as the crystal gets thicker. The simulation results from modeling crystals via MD simulation and simulating reflectivity by FDTD simulation show a good agreement with experimental results. In addition, we identify common crystal defects in the self-assembled colloidal crystals by inspecting the microstructure by SEM. By molecular dynamics and FDTD simulation, we construct crystals with a single defect type of vacancies, planar faults, stacking fault tetrahedra, or microcracks. We find that the defect density correlates strongly with a reduction in structural reflectivity. This chapter address the gap in the literature discussed previously in Section 1.3 and 1.4.

In chapter 3, we investigate the sensitivity of colloidal crystal quality and structural color reflectivity to the size and volume of irregularly sized particles. We produce colloidal crystals incorporating specific quantities of irregularly sized particles by the evaporative assembly and MD simulation. The particles of irregular sizes are microspheres either a larger or smaller diameter than the base colloids. We quantify colloidal crystal quality by processing images from SEM and visualization software OVITO for experimental and simulation structures, respectively. Both crystal quality and structural color reflectivity decrease as the volume fraction of irregularly sized particles increases. The reduction is less sensitive to the volume fraction than the size of irregularly sized particles. This chapter address the gap in the literature discussed previously in Section 1.3.

In chapter 4, we characterize structural color and microstructure of anisotropic structures, which are self-assembled from discoid particles. The size and aspect ratio of discoids are controlled by initial sphere colloids and applied forces during uniaxial compression. We produce dense discoid packings by evaporative assembly and Monte Carlo simulation. The reflection spectra of experimental and simulation structures are obtained from spectrophotometry and FDTD simulation, respectively. We find that increasing the size of discoid particles leads to a redshift of reflection peak. Decreasing the aspect ratio of the discoids results in a lower reflection peak, which correlates with a more disordered structure. Compared to iridescent structural color from sphere crystals, the structural color from discoid is less angular-dependent. The discoid structural color is also multi-spectral because of the combination of Bragg and backscattering. This chapter address the gap in the literature discussed previously in Section 1.2.

Lastly, this dissertation is concluded in chapter 5 by summarizing our findings and suggesting future research directions to expand the work presented.

1.10 References

[1] H. A. Shindy, "Problems and solutions in colors, dyes and pigments chemistry: A Review," vol. 3, no. 2, pp. 97–105, 2019.

[2] V. Saranathan *et al.*, "Structure, function, and self-assembly of single network gyroid photonic crystals in butterfly wing scales," *Proc. Natl. Acad. Sci.*, vol. 107, no. 26, pp. 11676–11681, Jun. 2010.

[3] A. E. Seago, P. Brady, J. P. Vigneron, and T. D. Schultz, "Gold bugs and beyond: A review of iridescence and structural colour mechanisms in beetles (Coleoptera)," *Journal of the Royal Society Interface*, vol. 6, no. SUPPL. 2. Royal Society, 06-Apr-2009.

[4] L. M. Mäthger, E. J. Denton, N. J. Marshall, and R. T. Hanlon, "Mechanisms and behavioural functions of structural coloration in cephalopods," *Journal of the Royal Society Interface*, vol. 6, no. SUPPL. 2. Royal Society, 06-Apr-2009.

[5] J. Bin Kim, S. Y. Lee, J. M. Lee, and S.-H. Kim, "Designing Structural-Color Patterns Composed of Colloidal Arrays," *ACS Appl. Mater. Interfaces*, vol. 11, no. 16, pp. 14485–

14509, Apr. 2019.

[6] M. D. Shawkey, N. I. Morehouse, and P. Vukusic, “A protean palette: Colour materials and mixing in birds and butterflies,” *Journal of the Royal Society Interface*, vol. 6, no. SUPPL. 2. Royal Society, 06-Apr-2009.

[7] F. Marlow, Muldarisnur, P. Sharifi, R. Brinkmann, and C. Mendive, “Opals: Status and prospects,” *Angewandte Chemie – International Edition*, vol. 48, no. 34. John Wiley & Sons, Ltd, pp. 6212–6233, 10-Aug-2009.

[8] B. Q. Dong *et al.*, *Structural coloration and photonic pseudogap in natural random close-packing photonic structures*, vol. 18, no. 14. Springer Science & Business Media, 2010.

[9] H. Fudouzi and Y. Xia, “Colloidal Crystals with Tunable Colors and Their Use as Photonic Papers,” *Langmuir*, vol. 19, no. 23, pp. 9653–9660, Nov. 2003.

[10] A. Richel, N. P. Johnson, and D. W. McComb, “Observation of Bragg reflection in photonic crystals synthesized from air spheres in a titania matrix,” *Appl. Phys. Lett.*, vol. 76, no. 14, pp. 1816–1818, Apr. 2000.

[11] H. Cong, B. Yu, S. Wang, L. Qi, J. Wang, and Y. Ma, “Preparation of iridescent colloidal crystal coatings with variable structural colors,” *Opt. Express*, vol. 21, no. 15, p. 17831, Jul. 2013.

[12] K. Katagiri, Y. Tanaka, K. Uemura, K. Inumaru, T. Seki, and Y. Takeoka, “Structural color coating films composed of an amorphous array of colloidal particles via electrophoretic deposition,” *NPG Asia Mater.*, vol. 9, no. 3, pp. 1–4, 2017.

[13] F. Meng, M. M. Umair, K. Iqbal, X. Jin, S. Zhang, and B. Tang, “Rapid Fabrication of Noniridescent Structural Color Coatings with High Color Visibility, Good Structural Stability, and Self-Healing Properties,” *ACS Appl. Mater. Interfaces*, vol. 11, no. 13, pp. 13022–13028, Apr. 2019.

[14] S. Zhu *et al.*, “Synthesis of Cu-doped WO3 materials with photonic structures for high performance sensors,” *J. Mater. Chem.*, vol. 20, no. 41, p. 9126, Oct. 2010.

[15] S. Banisadr, A. Oyefusi, and J. Chen, “A Versatile Strategy for Transparent Stimuli-Responsive Interference Coloration,” *ACS Appl. Mater. Interfaces*, vol. 11, no. 7, pp. 7415–7422, Feb. 2019.

[16] J. Ge, J. Goebl, L. He, Z. Lu, and Y. Yin, “Rewritable photonic paper with hygroscopic salt solution as ink,” *Adv. Mater.*, vol. 21, no. 42, pp. 4259–4264, Nov. 2009.

[17] H. Hu, Q. W. Chen, H. Wang, R. Li, and W. Zhong, “Reusable photonic wordpad with water as ink prepared by radical polymerization,” *J. Mater. Chem.*, vol. 21, no. 34, pp. 13062–13067, Sep. 2011.

[18] H. S. Lee, T. S. Shim, H. Hwang, S. M. Yang, and S. H. Kim, "Colloidal photonic crystals toward structural color palettes for security materials," *Chem. Mater.*, vol. 25, no. 13, pp. 2684–2690, Jul. 2013.

[19] Y. Heo, S. Y. Lee, J. W. Kim, T. Y. Jeon, and S. H. Kim, "Controlled Insertion of Planar Defect in Inverse Opals for Anticounterfeiting Applications," *ACS Appl. Mater. Interfaces*, vol. 9, no. 49, pp. 43098–43104, Dec. 2017.

[20] N. Suzuki, E. Iwase, and H. Onoe, "Micropatterning of Multiple Photonic Colloidal Crystal Gels for Flexible Structural Color Films," *Langmuir*, vol. 33, no. 24, pp. 6102–6107, 2017.

[21] A. C. Arsenault, D. P. Puzzo, I. Manners, and G. A. Ozin, "Photonic-crystal full-colour displays," *Nat. Photonics*, vol. 1, no. 8, pp. 468–472, Aug. 2007.

[22] Y. I. Andreeva, A. S. Drozdov, A. F. Fakhardo, N. A. Cheplagin, A. A. Shtil, and V. V. Vinogradov, "The controllable destabilization route for synthesis of low cytotoxic magnetic nanospheres with photonic response," *Sci. Rep.*, vol. 7, no. 1, pp. 1–9, Dec. 2017.

[23] G. Kamita *et al.*, "Biocompatible and Sustainable Optical Strain Sensors for Large-Area Applications," *Adv. Opt. Mater.*, vol. 4, no. 12, pp. 1950–1954, Dec. 2016.

[24] J. W. Kim, J. S. Lee, and S. H. Kim, "Biodegradable Inverse Opals with Controlled Discoloration," *Adv. Mater. Interfaces*, vol. 5, no. 10, p. 1701658, May 2018.

[25] W. B. Russel, D. A. Saville, and W. R. Schowalter, *Colloidal Dispersions*. Cambridge university press, 1991.

[26] C. Starr, C. Evers, and L. Starr, *Biology: Concepts and Applications*. Cengage Learning, 2005.

[27] W. Stöber, A. Fink, and E. Bohn, "Controlled growth of monodisperse silica spheres in the micron size range," *J. Colloid Interface Sci.*, vol. 26, no. 1, pp. 62–69, Jan. 1968.

[28] P. J. Dowding and B. Vincent, "Suspension 11olymerization to form polymer beads," *Colloids Surfaces A Physicochem. Eng. Asp.*, vol. 161, no. 2, pp. 259–269, Jan. 2000.

[29] M. Kogan, C. J. Dibble, R. E. Rogers, and M. J. Solomon, "Viscous solvent colloidal system for direct visualization of suspension structure, dynamics and rheology," *J. Colloid Interface Sci.*, vol. 318, no. 2, pp. 252–263, Feb. 2008.

[30] A. L. Rogach, N. A. Kotov, D. S. Koktysh, J. W. Ostrander, and G. A. Ragoisha, "Electrophoretic Deposition of Latex-Based 3D Colloidal Photonic Crystals: A Technique for Rapid Production of High-Quality Opals," *Chem. Mater.*, vol. 12, no. 9, pp. 2721–2726, Sep. 2000.

[31] H. Míguez *et al.*, "Control of the Photonic Crystal Properties of fcc-Packed Submicrometer

SiO2 Spheres by Sintering," *Adv. Mater.*, vol. 10, no. 6, pp. 480–483, Apr. 1998.

[32] A. S. Dimitrov and K. Nagayama, "Continuous Convective Assembling of Fine Particles into Two-Dimensional Arrays on Solid Surfaces," *Langmuir*, vol. 12, no. 5, pp. 1303–1311, Jan. 1996.

[33] H. Zheng and S. Ravaine, "Bottom-up assembly and applications of photonic materials," *Crystals*, vol. 6, no. 5, 2016.

[34] P. Jiang, J. F. Bertone, K. S. Hwang, and V. L. Colvin, "Single-Crystal Colloidal Multilayers of Controlled Thickness," *Chem. Mater.*, vol. 11, no. 8, pp. 2132–2140, 1999.

[35] P. A. Kralchevsky and N. D. Denkov, "Capillary forces and structuring in layers of colloid particles," *Curr. Opin. Colloid Interface Sci.*, vol. 6, no. 4, pp. 383–401, 2001.

[36] I. D. Hosein and C. M. Liddell, "Convectively assembled asymmetric dimer based colloidal crystals," *Langmuir*, vol. 23, no. 25, pp. 10479–10485, 2007.

[37] H. Cong and W. Cao, "Colloidal crystallization induced by capillary force," *Langmuir*, vol. 19, no. 20, pp. 8177–8181, Sep. 2003.

[38] J. Zhang, Z. Sun, and B. Yang, "Self-assembly of photonic crystals from polymer colloids," *Curr. Opin. Colloid Interface Sci.*, vol. 14, no. 2, pp. 103–114, 2009.

[39] L. V. Woodcock, "Entropy difference between the face-centred cubic and hexagonal close-packed crystal structures," *Nature*, vol. 385, no. 6612, pp. 141–143, Jan. 1997.

[40] A. D. Bruce, N. B. Wilding, and A. J. Ackland, "Free energy of crystalline solids: A lattice-switch monte carlo method," *Phys. Rev. Lett.*, vol. 79, no. 16, pp. 3002–3005, Oct. 1997.

[41] S. Wong, V. Kitaev, and G. A. Ozin, "Colloidal Crystal Films: Advances in Universality and Perfection." *Journal of the American Chemical Society*, 125.50 (2003): 15589-15598.

[42] Y.-H. Ye, F. LeBlanc, A. Haché, and V.-V. Truong, "Self-assembling three-dimensional colloidal photonic crystal structure with high crystalline quality," *Appl. Phys. Lett.*, vol. 78, no. 1, pp. 52–54, Jan. 2001.

[43] T. Liu, B. Vansaders, S. C. Glotzer, and M. J. Solomon, "Effect of Defective Microstructure and Film Thickness on the Reflective Structural Color of Self-Assembled Colloidal Crystals," *ACS Appl. Mater. Interfaces*, vol. 12, no. 8, pp. 9842–9850, Feb. 2020.

[44] E. Özbay, "Layer-by-layer photonic crystals from microwave to far-infrared frequencies," *J. Opt. Soc. Am. B*, vol. 13, no. 9, p. 1945, 1996.

[45] J. F. Galisteo-López, E. Palacios-Lidón, E. Castillo-Martínez, and C. López, "Optical study of the pseudogap in thickness and orientation controlled artificial opals," *Phys. Rev. B*, vol. 68, no. 11, p. 115109, Sep. 2003.

[46] C. J. R. Sheppard, “Approximate calculation of the reflection coefficient from a stratified medium,” *Pure Appl. Opt. J. Eur. Opt. Soc. Part A*, vol. 4, no. 5, pp. 665–669, Sep. 1995.

[47] I. Goldstein, Joseph and H. Yakowitz, “Practical scanning electron microscopy: electron and ion microprobe analysis,” *Springer Sci. Bus. Media*, 2012.

[48] R. T. Tan, “Specularity, Specular Reflectance,” in *Computer Vision*, Springer US, 2014, pp. 750–752.

[49] A. K. R. Choudhury, “Object appearance and colour,” in *Principles of Colour and Appearance Measurement*, Elsevier, 2014, pp. 53–102.

[50] G. Piszter, K. Kertész, Z. Balint, and L. P. Biró, “Variability of the structural coloration in two butterfly species with different prezygotic mating strategies,” *PloS One*, vol. 11, no. 11, p. e0165857, Nov. 2016.

[51] T. Smith and J. Guild, “The C.I.E. colorimetric standards and their use,” *Trans. Opt. Soc.*, vol. 33, no. 3, pp. 73–134, Jan. 1931.

[52] M. Shaw and M. Fairchild, “Evaluating the 1931 CIE color-matching functions,” *Color Res. Appl.*, vol. 27, no. 5, pp. 316–329, Oct. 2002.

[53] C. L. Hardin, “Why color?,” in *Perceiving, Measuring, and Using Color*, 1990, vol. 1250, no. 1, pp. 293–300.

[54] International Telecommunication Union, *Parameter values for the HDTV standards for production and international programme exchange Opto-electronic conversion*. 2002.

[55] Mansencal, Thomas, Mauderer, Michael, Parsons, Michael, Shaw, Nick, Wheatley, Kevin, Cooper, Sean, … Hill, Stephen. (2020, January 25). Colour 0.3.16 (Version 0.3.16). Zenodo. http://doi.org/10.5281/zenodo.3757045.

[56] M. P. Allen, “Liquid crystal systems." *Computational soft matter: from synthetic polymers to proteins*, vol. 23, 2004.

[57] S. Jabbari-Farouji and E. Trizac, “Dynamic Monte Carlo simulations of anisotropic colloids,” *J. Chem. Phys.*, vol. 137, no. 5, p. 54107, Aug. 2012.

[58] S. L. Manoto, C. Mabena, R. Malabi, S. Ombinda-Lemboumba, and P. Mthunzi-Kufa, “Design and FDTD simulation of photonic crystal based sensor for biosensing applications,” in *Frontiers in Biological Detection: From Nanosensors to Systems XI*, 2019, vol. 10895, p. 35.

[59] O. Hess, C. Hermann, and A. Klaedtke, “Finite-difference time-domain simulations of photonic crystal defect structures,” *Phys. Status Solidi Appl. Res.*, vol. 197, no. 3, pp. 605–619, 2003.

Chapter 2 Effect of Defective Microstructure and Film Thickness on the Reflective Structural Color of Self-Assembled Colloidal Crystals

2.1 Abstract

Structural color arises from geometric diffraction; it has potential applications in optical materials because it is more resistant to environmental degradation than coloration mechanisms that are of chemical origin. Structural color can be produced from self-assembled films of colloidal size particles. While the relationship between the crystal structure and structural color reflection peak wavelength is well studied, the connection between assembly quality and the degree of reflective structural color is less understood. Here, we study this connection by investigating the structural color reflection peak intensity and width as a function of defect density and film thickness using a combined experimental and computational approach. Polystyrene microspheres are self-assembled into defective colloidal crystals via solvent evaporation. Colloidal crystal growth via sedimentation is simulated with molecular dynamics, and the reflection spectra of simulated structures are calculated by using the finite-difference time-domain algorithm. We examine the impact of commonly observed defect types (vacancies, stacking fault tetrahedra, planar faults, and microcracks) on structural color peak intensity. We find that the reduction in peak intensity scales with increased defect density. The reduction is less sensitive to the type of defect than to its volume. In addition, the reflectance of structural color increases as a function of the crystal thickness, until a plateau is reached at thicknesses greater than about 9.0 μm. The maximum reflection is 78.8 ± 0.9%; this value is significantly less than the 100% reflectivity

predicted for a fully crystalline, defect-free material. Furthermore, we find that colloidal crystal films with small quantities of defects may be approximated as multilayer reflective materials. These findings can guide the design of optical materials with variable structural color intensity.

This chapter was adapted from a publication: Tianyu Liu, Bryan VanSaders, Sharon C. Glotzer, and Michael J. Solomon. "Effect of Defective Microstructure and Film Thickness on the Reflective Structural Color of Self-Assembled Colloidal Crystals." *ACS applied materials & interfaces* 12, no. 8 (2020): 9842-9850. Tianyu Liu and Michael J. Solomon conceived the research and designed the experiments. Tianyu Liu conducted the experiments. Bryan VanSaders and Sharon C. Glotzer designed the computer simulation. Bryan VanSaders performed the simulations.

2.2 Introduction

Structural color is the brilliant iridescence found in organisms and natural materials such as the wings of butterflies,[1] the feather of peacocks,[2] and opals[3]. This kind of color arises due to light diffraction from periodically ordered structures at submicron scale[4]. Structurally colored materials can have better stability than conventional pigments such as dyes because they can be made from materials which are less susceptible to environmental degradation. Inspired by these biological systems, scientists have sought to study and mimic various bio-structures developed through evolution, so as to synthesize artificial structures for optical applications such as coatings[5],[6] and sensors [7],[8]. Various microfabrication methods have been applied to create submicron ordered structures, including colloidal self-assembly[9]–[15], lithography[16], [17], and layer-by-layer deposition [18], [19]. Among those fabrication methods, colloidal self-assembly is of interest because of its simplicity and scalability. To accommodate colloids of different

material functionality, a variety of self-assembly methods have been considered to achieve the desired ordering, such as evaporative deposition,[9] electrophoretic deposition,[10], [11],[13] sedimentation[12], and dip deposition[14], [15]. In addition, computer simulation has been used as a powerful tool to predict the process of self-assembly [20]–[22].
At the same time, experimental tools such as light scattering as well as direct visualization by confocal microscopy enable the characterization of crystal microstructure, and the kinetics of self-assembly [23]–[26].

Studies of structural color in self-assembled colloidal crystals have primarily focused on controlling the wavelength of peak reflection [27]–[31]. The connection between assembly, microstructural properties, and reflective color intensity is a related question that also warrants investigation. Self-assembled colloidal crystals usually contain defects [32], [33]. Reflection properties are likely mediated by the defect microstructure of the film. However, a quantitative relationship between defect type/density and the reflectance of structural color remains unclear.

The purpose of this study is therefore to establish the relationship between microstructural properties of the colloidal crystals and the reflectance of their structural color. We investigate the effect of crystal defect and crystal thickness on film reflection using a combined experimental and computational approach. Quantitative prediction of reflective color requires that the impact of defects on the optical response be considered. To that end, we prepared model systems via molecular dynamics (MD) simulation and calculated reflection spectra using finite-difference time-domain (FDTD) calculation of Maxwell's equations. Beyond simulating the self-assembly process of films formed from a dispersed colloidal state, we also produced simulated films with defects which had been intentionally introduced. This approach quantifies the specific contribution of commonly

observed colloidal crystal defects to the overall reflection properties. We find that defect density correlates strongly with loss of reflectivity.

Film thickness is an important parameter in engineering optical coatings. There have been several studies which investigated the thickness dependence of the stop band in the transmission spectra of artificial opals with superior quality [34], [35]. Attaining high crystal quality in a colloidal film can be challenging, especially when a high film growth rate is desired. Rapidly grown films may contain a variety of defects and is currently unknown to what extent these defect species impact the optical properties of the film. To investigate the role of defect-laden crystal thickness on reflection properties, we produce a series of films by means of the fast evaporation deposition method. By controlling the initial volume fraction of the suspension, the deposition method produces flat crystal films of variable thickness. The reflective color of a self-assembled film is a function of the reflection peak intensity and width, above that of diffuse background scattering. These are measured using white-light reflection spectroscopy. We use molecular dynamics to simulate colloidal crystal growth via sedimentation to validate and explain the experimental results. Additionally, we find that the representation of colloidal films as multilayer materials yields a good approximation of film reflection as a function of thickness.

This work produces an understanding of the relationship between crystal microstructure and structural color intensity; this understanding can guide the design of spectral materials and support defect engineering in colloidal crystals.

2.3 Materials & Methods

2.3.1 Fabrication of colloidal crystals

Polystyrene spheres (Polysciences) of diameter 200 ± 20 nm were dispersed in ethanol at volume fractions ranging from 1% to 26% to study the effect of crystal film thickness. Self-assembly was performed on glass slides that were cleaned with a UVO-cleaner (Model 42, Jelight) for 5 minutes. Adhesive silicone isolators (Grace Bio-Labs) with 20 mm diameter and 0.5 mm depth were applied onto the glass slides to define the area available for evaporative self-assembly. 25 μL of the dispersion of polystyrene colloids was placed into an isolator and evaporated at room temperature. During the evaporation process, colloidal spheres self-assembled into regions of high density, thereby yielding three-dimensional lattices. The uniformity of the crystal film is affected by humidity and temperature **[**36]**.** The surface area of these crystals is approximately 314 mm^2. We select samples of uniform thickness across this surface area (approximately 90% of all samples) to study the relationship between crystal thickness and reflectance. Their thickness depends on the initial volume fraction of the solution from which they are self-assembled.

2.3.2 Characterization of colloidal crystals

The thickness of the colloidal crystal films produced by self-assembly was measured using a stylus profilometer (Dektak XT). The microscopic quality of the colloidal crystals was investigated by scanning electron microscopy (Tescan MIRA3 FEG SEM). The samples were sputtered coated with a thin layer of gold before imaging to reduce the charging effects. To analyze cross sections of the crystals, samples on glass slides were snapped with a diamond scribe pen. Optical properties of colloidal crystals were characterized by measuring their reflection spectra at 8 ° incidence relative to the normal plane, using a Thermo Scientific Evolution 600 UV-Vis spectrophotometer equipped with

a Spectralon® integrating sphere (DRA-EV-600) which collects all light reflected into the backward hemisphere.

2.3.3 Computer simulations

Colloidal films were simulated via molecular dynamics (MD) using the package HOOMD-Blue [37],[38]. All simulations were performed under the Langevin thermostat and hard particle interactions were simulated using the shifted Weeks-Chandler-Anderson (WCA) potential. Particles with a distribution of diameters were simulated; this distribution matched that of the experimental system, which was characterized via SEM.

Systems prepared by molecular dynamics were later used for FDTD calculation of film reflection. Therefore, system size was limited by the high memory requirements of the FDTD electromagnetic calculation method. For simulated sedimentation, approximately 8000 particles were initialized in a periodic box. A repulsive (WCA potential) lower boundary was introduced to act as the sedimentation surface. A constant force (representing fluid drag during evaporation) was applied antiparallel to the wall normal. Sedimentation simulations were begun at sufficient temperatures to fluidize the dispersion, then cooled (at various rates, mimicking the experimental preparation procedure) to very low temperatures. Particles were assigned a local crystal structure (face-centered cubic, hexagonal close-packed, or disordered) by Adaptive Common Neighbor Analysis (aCNA) [39].

Films with intentionally introduced defects were prepared similarly but prevented from initially melting. The starting configuration was a close-packed face-centered cubic (FCC) crystal, with the [111] crystal direction antiparallel to the gravity force and the [1-10] and [11-2] directions aligned with the periodic box edge normal. Samples with stacking faults were produced by the shifting of close-packed (111) planes of a perfectly crystalline film. Samples with dispersed

vacancies were produced by random deletion of particles. Samples with clustered vacancies were produced by deletion of particles to form a spherical void. Samples with stacking fault tetrahedra (SFTs) were produced by the deletion of a planar triangular cluster of particles in a (111) plane. Samples with microcracks were allowed to thermally relax while the box direction aligned with the [1-10] and [11-2] crystal directions were slowly expanded. Microcracking simulations were larger than other defect simulations (approximately 24,000 particles) to reduce the influence of the periodic box boundaries on the cracks that were formed. Additionally, mild short-range particle attraction was added so as to permit the opening of cracks. This attraction represents the adhesion forces present in the dry assembled film. A finite-difference time-domain (FDTD) algorithm as implemented in the commercially available code Lumerical FDTD Solutions™ was used to solve the Maxwell equations and calculate the reflectance of the simulated crystals. The refractive index was matched with the properties of polystyrene. The angle of the incident light was the same as that in the experiment, 8°. The FDTD method yields simulated spectra that can be directly compared to the experimental measurements to develop functional relationships between crystal properties measures and reflective structural color.

As an alternative to full-particle electromagnetic simulation, multilayer material reflection spectra were computed using the transfer matrix method (TMM) [40]. In these multilayer calculations, the colloidal crystal was approximated by an alternating sequence of high and low dielectric layers. The thickness of these layers is set as ½ the [111] plane spacing in the ideal FCC crystal. The refractive index of these layers was computed as a dielectric mixture based on the volume fraction of air and polystyrene in the high and low index layers [41]. The description of MD simulation and TMM calculation was adapted from our publication.

2.4 Results and Discussions

Images of colloidal crystals fabricated by evaporative assembly are reported in Figure 1a. The color of the specimen changes during the 7-min evaporation process. During the late stages of drying, there is a thin layer of liquid film on the sample surface which exhibited interfacial color (as shown in photos at 4 – 7 minutes in Figure 1a). After the ethanol is completely evaporated from the dispersion, the final colloidal crystal film exhibited blue color, as indicated in the last panel of the image series. A cross section showing film microstructure after crystallization is presented in Figure 1b. The SEM image suggests that this colloidal crystal exhibits a close-packed crystal structure. Figure 1c shows a simulated film after sedimentation. Particles were colored by their local environment, with green particles having FCC nearest neighbor shells, red particles having hexagonal close-packed (HCP) neighbor shells, and white particles having disordered shells. FCC is the dominant crystal type observed both in our experimental and simulated structures. This FCC preference is explained by the relative free energies of the FCC and HCP crystal structures.[42] Figure 1d shows the reflection spectra measured in the experiment and calculated from the simulation. An initially disordered colloidal suspension does not show Bragg scattering, whereas the colloidal crystal shows a Bragg reflection peak located at 473 nm. The peak of the simulated spectra – at 476 nm – matches the experiments, corroborating that long-range crystalline order is the origin of the structural color. The wavelength of this peak can be estimated from the Bragg equation [9], [43]

$$m\lambda = 2d_{hkl}({n_a}^2 - sin^2\theta)^{1/2} \quad (1)$$

where m is the diffraction order, λ is the wavelength of the reflected light, n_a is the mean refractiveindex of the crystal, d_{hkl} is the interlayer spacing along the [hkl] direction, and θ is the angle between the incident light and the normal to the (hkl) planes (here equal to 8°).

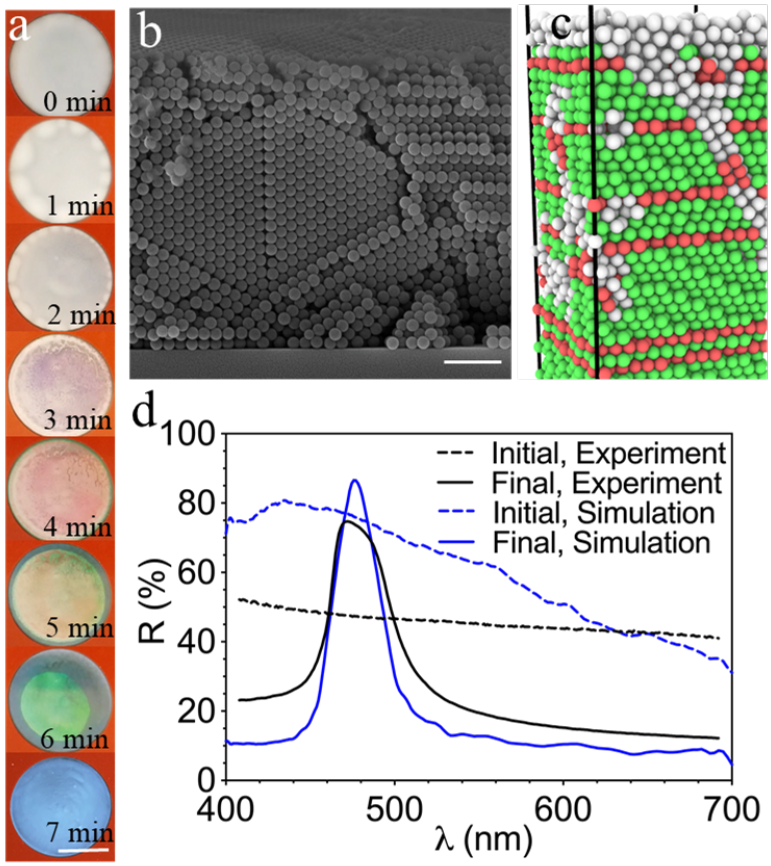

Figure 2-1. Photographs, SEM, simulation structure, and reflection spectra of colloidal crystals fabricated by evaporative assembly to produce structural color. (a) Reflective structural color of colloidal crystals of polystyrene spheres undergoing evaporative self-assembly; images are spaced at 1 min intervals. (b) Cross-sectional SEM image of the colloidal crystal after evaporation; the structure is one that leads to the structural color apparent in the last image of (a). (c) Simulated structure, after the completion of self-assembly, with particles colored by local environment (green=FCC, red=HCP, white=disordered), contributed by Bryan VanSaders. (d) initial and final state reflection spectra as measured by experiment and computed by simulation. Scale bar in (a) is 10 mm; (b) is 1 μm.

n_a is calculated by the relation $n_a{}^2 = \emptyset n_{ps}{}^2 + (1 - \emptyset) n_{air}{}^2$, where $\emptyset$ is the volume fraction of particles (here $\emptyset = 0.74$) and n_{ps} is the refractive index of polystyrene particles.[41], [44] For the spacing of the [111] planes of close-packed crystal structures, $d_{hkl} = 0.82d$, where d is the diameter of particles. The calculated peak location is 476 nm, which agrees well with the experimental reflection peak at 473 nm and the simulated reflection peak at 476 nm.

We compared the crystal structures prepared by experiment, the simulated sedimented samples, and perfect FCC crystals. Figure 2a shows that experimental crystals contain defects including vacancies, stacking fault tetrahedra (SFT), and microcracks. The size of these defect features is similar to the wavelength of peak structural color reflection. In large-area surveys of experimentally prepared films, we find no evidence of sample cracking wider than $1\mu m$ (Figure S1). The influence of such sub-wavelength features with complex geometries likely requires full electromagnetic wave calculations such as those pursued here, so as to accurately capture diffraction effects. This situation differs from an alternative scenario, not observed here, in which wide and deep cracks would allow light rays to transmit through the specimen unhindered, without interacting at all with the dielectric material. Thus, modeling how light diffracts in the defect-rich crystal is essential to explain the reflectivity properties measured in the experiments.

For the structure produced by simulated sedimentation (Figure 2b), the defect analysis shows that planar stacking faults, HCP domains, and dislocations are common defects. These naturally arise during sedimentation, consistent with literature reports.[33] For comparison, Figure 2c shows a perfect FCC structure without defects.

We produced these three kinds of crystal structures at a constant thickness of 7.4 μm and further compared their reflection spectra. Figure 2d shows that the perfect FCC crystal is capable of 100% reflectance. With the presence of defects, experimentally produced films, as well as the

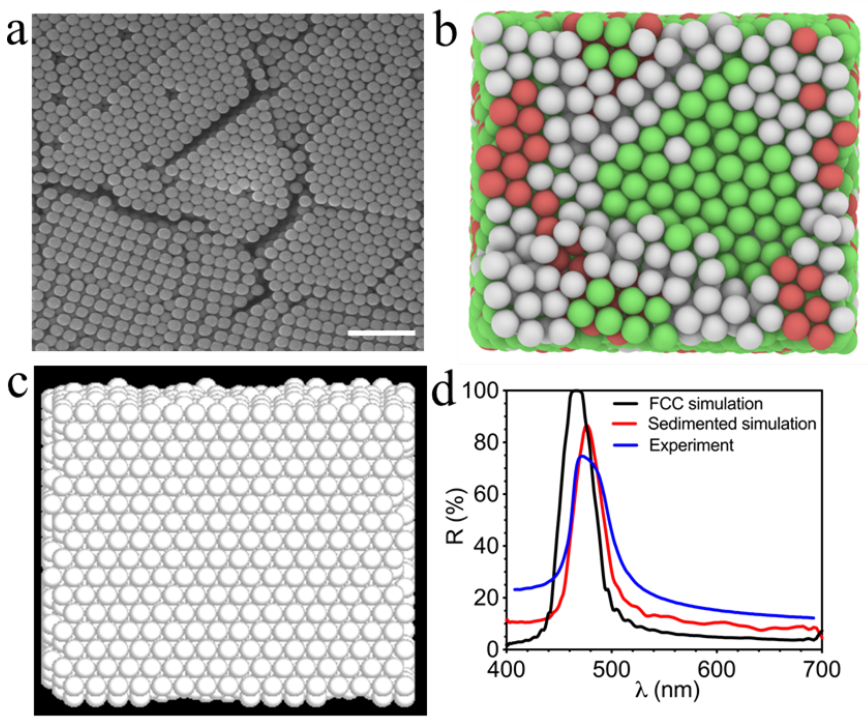

Figure 2-2. Comparison of crystal structures and reflection spectra by experiment, MD simulation, and FCC crystal. a) A typical SEM image of the top surface of a colloidal crystal film; Scale bar is 1 μm. (b) A simulated structure from sedimentation, with particles colored by local environment (green=FCC, red=HCP, white=disordered. (c) A perfect FCC crystal without defects.), (c) and (d) were produced by Bryan VanSaders. (d) The spectra for a pure FCC crystal, a simulated crystal, and an experimentally produced one; each is of the same 7.4 μm thickness.

models prepared by simulated sedimentation, have lower peak reflectance values and slightly larger peak wavelength. The difference in peak wavelength between the perfect crystal and the simulated or experimental systems is because defects typically increase the interlayer space, which results in an increase in the peak wavelength, as per the Bragg equation. Therefore, the peak wavelength of the FCC theory is smaller than the experimental and simulation structures. The difference in peak reflection is also likely caused by the defect microstructure of these films, which we now explore by computer simulation.

The microstructure of sedimented films can be broken down into short-range features – e.g. vacancies – as well as long-range features – e.g. stacking faults, dislocations, and grain boundaries. Reflective structural color intensity is a function of these different defect types, each of which has been observed in SEM studies of the film surface (Figure 2a). Surface microcrack patterns display triangular symmetry, implying the existence of stacking fault tetrahedra (SFTs) in sedimented films. (Figure 3c inset shows the geometry of an SFT.) SFTs are clusters of vacancies which can form in crystals with low stacking fault energy. Pronk and Frenkel[45] have shown that hard spheres have very low stacking fault energies, and so we also examine the effect of SFT clusters on structural color.

Figure 3a-e shows the reflection spectra of simulated films prepared with different concentrations of dispersed vacancies, clustered vacancies, SFTs, planar stacking faults, and microcracks, respectively. The insets show representative geometries of each defect type. Specifically, the number fraction of deleted particles is varied in Figure 3a-c, leading to dispersed vacancies, clustered vacancies, and stacking fault tetrahedra (SFTs), respectively; The number of planar faults is varied in Figure 3d; The uniaxial strain, as a percentage, is varied in Figure 3e, resulting in the microcracks. Figure 3a demonstrates that increasing the dispersed vacancy content decreases peak reflection intensity. Dispersed vacancies also increase the level of background

reflection at off-peak wavelengths. This is a consequence of diffuse, wavelength-independent scattering from the sub-wavelength local density changes caused by dispersed vacancies. When vacancies are collected into a spherical void, the increasing volume fraction of the void causes a reduction in the peak reflection and a small increase in background reflection (Figure 3b). Introducing SFT vacancy clusters has some effect on peak intensity, with a less pronounced effect on the broad-spectrum background (Figure 3c). That is, dispersed vacancies have a larger effect on background reflection than vacancy clusters. Planar stacking faults have a minimal effect on the peak reflection intensity (Figure 3d). Lastly, Figure 3e shows that in-plane stretching produces microcracks which cause a reduction of peak intensity.

To explore how these defect types, contribute to structural color reflectivity, we plot their peak reflectance values as a function of the defect density ρ_d (Figure 3f). Here we define defect density as the ratio of empty volume (added to the system as a result of the introduction of that particular defect) and total crystal volume. For SFTs and vacancies containing samples, the defect volume is the volume of the deleted particles. Planar stacking faults, which have no defect volume, cannot be considered on a per-volume basis. For strained samples with microcracks, this is the volume added due to the stretching.

We find that a general trend exists which relates the defect density to the reflection peak intensity (Figure 3f). The defect volume is the dominant factor predicting the reflectance; the type of defect volume is a secondary factor. However, different kinds of defects (which correspond to different ways of organizing defect volume) do generate modestly different trends in the reflectance vs. volume relation, indicating that some species of defects are more efficient at disrupting structural color given a similar defect density and within certain defect volume ranges.

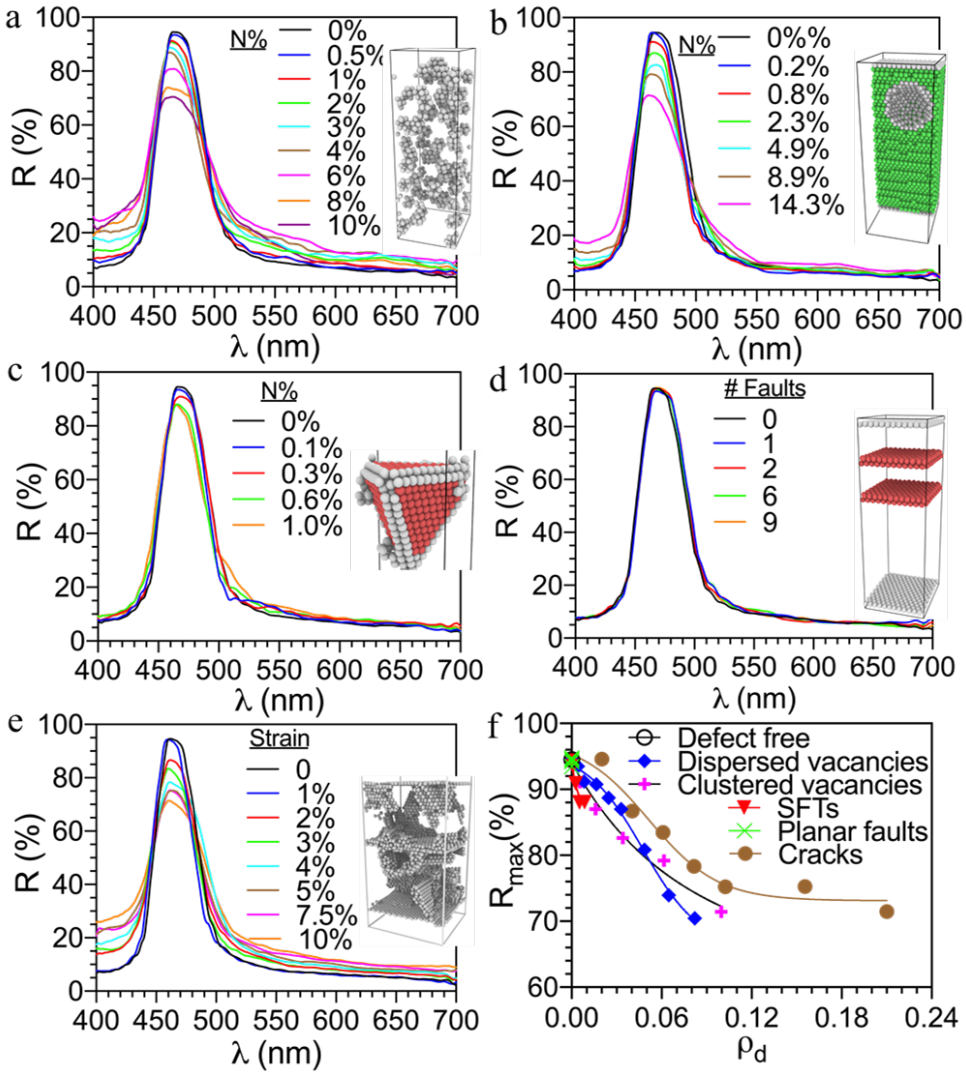

Figure 2-3. Reflection spectra of simulated films prepared with different concentrations of vacancies, SFTs, planar stacking faults, and microcracks, respectively. (a) Reflection spectra of crystal structures with different number fraction of dispersed vacancies in sedimented films. (b) Reflection spectra of crystal structures with different number fractions of clustered vacancies forming a spherical void in sedimented films. (c) Reflection spectra of crystal structures with different number fractions of deleted particles, leading to stacking fault tetrahedra (SFT). (d) Reflected light intensity and wavelength are nearly independent of the number of planar stacking faults present. (e) Reflection spectra of crystal structures subjected to different amounts of biaxial strain, leading to microcracks. Each inset shows the geometry of dispersed vacancies (a), clustered vacancies (b), an SFT (c), stacking faults (d), and microcracks (e), respectively, generated by Bryan VanSaders. Particles are colored by local environment (green=FCC, red=HCP, white=disordered). For voids, a cut-away of the film structure is shown. Otherwise, only particles with defective environments are shown. (f) Compilation of peak reflectance R_{max} as a function of defect density ρ_d added to the system for the set of defect types studied.

Specifically, we find that dispersed vacancies at low concentrations are less efficient at disrupting structural color, on a per unit volume basis, than clustered vacancies. The optical scattering from a single isolated vacancy is diffuse, as the vacancy has a size comparable to the wavelength of the incident light. At low vacancy concentrations, they behave as a dilute solution of diffuse, low contrast scatters; they only weakly perturb film reflection. A small amount of dispersed vacancies has a less negative effect on reflection compared with when those vacancies form into a spherical vacancy cluster. As vacancy concentration is increased, however, the trend reverses; in this defect volume range dispersed vacancies become more damaging to the optical properties of the film than vacancy cluster. This effect is thought to be due to the interaction of multiple vacancies (vacancy clusters) and the subsequent formation of larger-sized defects that generate additional scattering.

The way of organizing small defect volume which is most detrimental to structural color is in an SFT. The peak reflection dramatically decreases with a small defect density (Figure 3e). This is understood because the edges of the SFT also act as weak scattering planes, and for a given vacancy cluster size the SFT formed has a larger surface area than when those vacancies are collected into a spherical cluster. The extended nature of SFTs limits our study to small defect volume fractions; the highest defect concentration shown here for SFTs (~1%) represents SFTs which cover the entire area of the film by touching corner-to-corner. As the number of vacancies is increased, Figure 3f shows that the derivative of the vacancy defect density curve becomes more similar to that of the SFT curve, a result of vacancy cluster (and/or SFT) formation from the coalescence of multiple vacancies.

Finally, biaxial stretching, which leads to microcracks, is found to be less detrimental to the reflectivity than vacancies are. The peak reflection of cracked films decreases most rapidly for

in-plane strains of 2-5%. For these strains, many defects are produced as the film is cracked. For larger strains, few additional defects are created because the films have cracked completely. An asymmetric sigmoidal function approximates this behavior well. For large concentrations of vacancies (>5%) we find that vacancies are close enough to consolidate into other structures such as vacancy clusters or dislocation lines during the initial stages of model preparation. These consolidated structures share similarities to the defect microstructures produced by in-plane stretching. These results indicate that the long range non-planar faults produced by stresses in the film or vacancy clusters have a strong negative effect on reflection quality.

We now turn to the effect of film thickness on the peak properties (intensity and width) of structural color reflection. We produce by experiment and simulation a series of colloidal crystals with thicknesses ranging from 1.4 μm to 16.1 μm. The film thicknesses in the experiment are controlled by the initial volume fraction of the colloidal suspension that is evaporated and the diameter of those colloids. Given the close-packed layer thickness of 0.164 μm, these crystals vary from about 8 to 97 layers. Due to the large memory requirements of the FDTD method, all the simulated film thicknesses are less than 13.0 μm, which corresponds to 79 layers.

The measured reflection spectra of the experimentally produced structures are shown in Figure 4a. For the experimental crystal structures, thin films yield low peak reflectivity and broad reflections. As the film thickness increases, the reflectivity peak intensity increases and the peak width narrows. Finally, the thickest films no longer increase in reflectivity; there is also a broadband increase in background reflection at off-peak wavelengths. The optical calculations are performed both for crystals produced via simulated sedimentation (Figure 4b) and for a perfect FCC structure (Figure 4c). Both are produced under conditions analogous to the experiments. The simulated structures yield reflection properties that agree with the

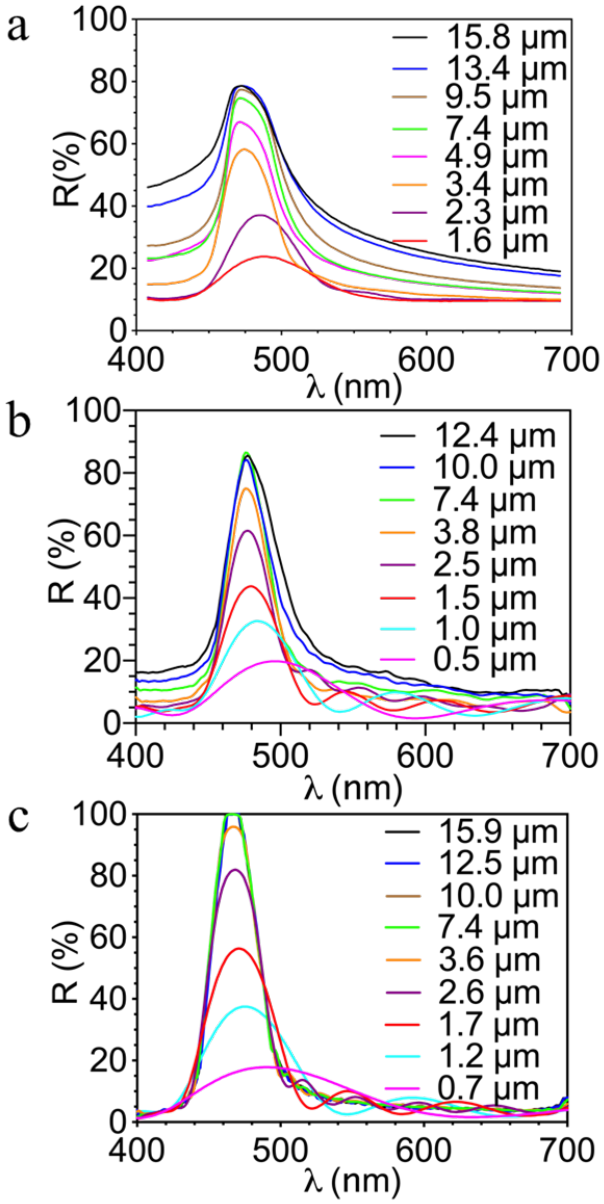

Figure 2-4. Reflection spectra of colloidal crystal films with different thicknesses produced by experiment, MD simulation, and for an FCC crystal. (a) Measured reflection spectra of colloidal crystal films with different thicknesses. (b) Simulated reflection spectra of films of colloids grown via sedimentation and containing defects. (c) Simulated reflection spectra of the perfect FCC structure with increasing crystal film thicknesses.

experimental results. Increasing film thickness yields greater peak reflectivity accompanied by band narrowing. For the perfect FCC structure, a band of complete reflectivity is observed for the thickest samples. Off-peak wavelengths show oscillating reflectivity. These small, oscillating peaks on the shoulders of the primary reflection for the perfect FCC crystal are interference fringes; they are obscured by diffuse scattering in real films, as generated by both defects and polydispersity in particle diameter.

To understand why the reflectance varies with thickness as observed, we compare these results to the theory of multilayer reflectors. In this theory, the material is represented as a set of alternating layers of high and low refractive index. The thickness of each layer is equal to half the interlayer spacing of a defect-free hard-sphere crystal. The high and low refractive indices are computed from the volume fill fraction of each layer. This model is a one-dimensional approximation of the three-dimensional periodic structure of the colloidal crystal.[40] Figure 5a shows the change in multilayer reflection as the total stack thickness is increased. This reflectance trend shows a close similarity with the results obtained from FDTD simulation of a perfect FCC crystal (c.f. Figure 4c). We compare this theory to the peak reflectivity measured for different crystal film thickness by experiment, simulation, and the perfect FCC crystal in Figure 5b.

The multilayer reflection theory captures the optical behavior of the perfect FCC crystal, displaying the same trends for reflectance peak intensity as a function of film thickness. Similar trends are also seen in the results derived from the experiment and sedimented simulation. Specifically, in the limit of small film thickness, the intensity of the reflection peak increases approximately linearly with the thickness of crystal films, ultimately reaching reflection saturation. Saturation occurs for film thicknesses greater than 5.9 μm (35 layers) for the multilayer calculation and the FCC simulation, greater than 8.0 μm (48 layers) for the sedimented simulation, and greater

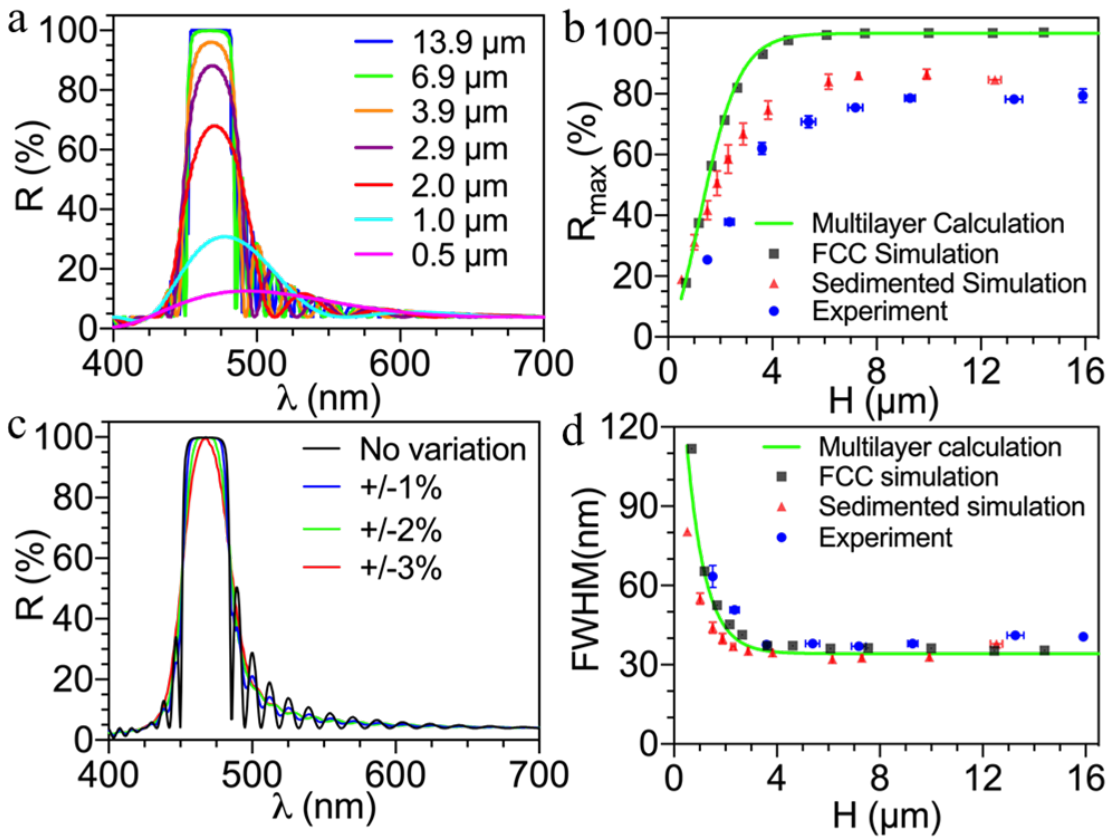

Figure 2-5. Effect of crystal thickness on reflection peak intensity and peak width. (a) Theoretical reflection spectra of the multilayer material as a function of total stack thickness. (b) The relationship between crystal thickness (H) and reflection peak intensity (R_{max}) for a perfect FCC crystal, for a crystal formed by simulated sedimentation, and for an experimentally produced crystal. The curve is the prediction of the multilayer reflector theory. (c) Reflection spectra of multilayer materials with Gaussian distributions of layer thicknesses. The values of standard deviation σ are 0.5%, 1%, and 1.5% of layer thickness, respectively, calculated by Bryan VanSaders. (d) The effect of crystal thickness on full width at half maximum (FWHM) of the reflectance.

than 9.0 μm (54 layers) for the experiment. Saturation thickness for each case was calculated by fitting data with an exponential plateau function. We consider this curve saturated if a reflection value reaches 98% of maximum reflection. Although the difference between the experiment and simulation saturation thicknesses is minimal, the difference between these and the other two theoretical cases indicates that defect-rich structures require additional colloidal crystal layers to achieve saturation of the reflectivity. For sufficiently thick films, the penetration of light through the full stack is negligible;[46] the top layers of the film dominate the optical response. This suggests that excessive crystal thickness minimally affects the reflective structural color intensity. For the FDTD simulation based on the perfect FCC structure, the reflection saturation also reaches 100%. The experimental structure and simulated structures from sedimentation have defects in the crystals, which cause the reflection value to instead saturate at 78.8% ± 0.9%. The effect of such defects was previously discussed in Figure 3, which explains the difference in saturation reflection between defective structures and FCC perfect crystal. The small discrepancy between experimental and simulated structures is most likely caused by system size effects. Specifically, the surface area of simulated structures is constant at 7.9 μm^2, to accommodate the significant memory requirements of the FDTD calculation. Large-scale defect structures spanning several microns cannot be incorporated into such small periodic domains. In the experiments, the surface area of samples is much larger: 3.1×10^8 μm^2. Defect structures of lateral dimension greater than 7.9 μm^2 are therefore cutoff in the simulation, leading to slightly greater reflectivity. Generally, the results from the sedimentation simulation agree with experimental data, suggesting that this simulation method would be useful to predict the reflection intensity of colloidal crystal films. Figure 5c shows how the multilayer reflector model can account for the experimentally observed Gaussian peak

shape. The total reflectance from a multilayer stack with a Gaussian distribution of layer separations was computed. The values of standard deviation, σ, are 0.5%, 1%, and 1.5% of the layer thickness, respectively. Variation in layer thickness is Gaussian distributed, as opposed to the stopband of the multilayer model, which has uniform layer thickness. Including this heterogeneity of layer thickness into the multilayer model yields reflectance peaks that are similar in shape to the peaks observed in the experiments. This congruence suggests that heterogeneity in layer thickness induced by e.g. particle polydispersity and crystal distortions could be responsible for the peak shape observed in the experiments. Figure 5d shows the dependence of reflection peak width on film thickness. As the film approaches the saturation thickness, the full width at half maximum (FWHM) of the reflection peak decreases until reaching a saturation value of 38.8 nm ± 0.5 nm at the crystal thickness of 3.9 μm. This trend holds for the experiment, simulation, and theory. This is again a consequence of constructive interference; as more layers are added, the reflection spectra approach the ideal behavior of a perfect Bragg reflector.[47] This narrowing effect prior to saturation is similar to the Debye-Scherrer effect in crystals (in which the X-ray diffraction peak width narrows in inverse proportion to the number of lattice planes).[48] In addition, the overall trend of peak width of defective structures (experiment and sedimented simulation) is close to results from perfect crystals (multilayer calculation and FCC simulation). This indicates that defects have little impact on the peak width of structural color.

Figure 5b shows that the reflection saturation occurs at 9.0 μm thickness for experimental polystyrene/air structures. This saturation thickness depends on the refractive contrast between the particles and their surrounding environment[49]. Figure 6a provides guidance as to the peak reflectance expected from different refractive index contrasts of common colloid-matrix

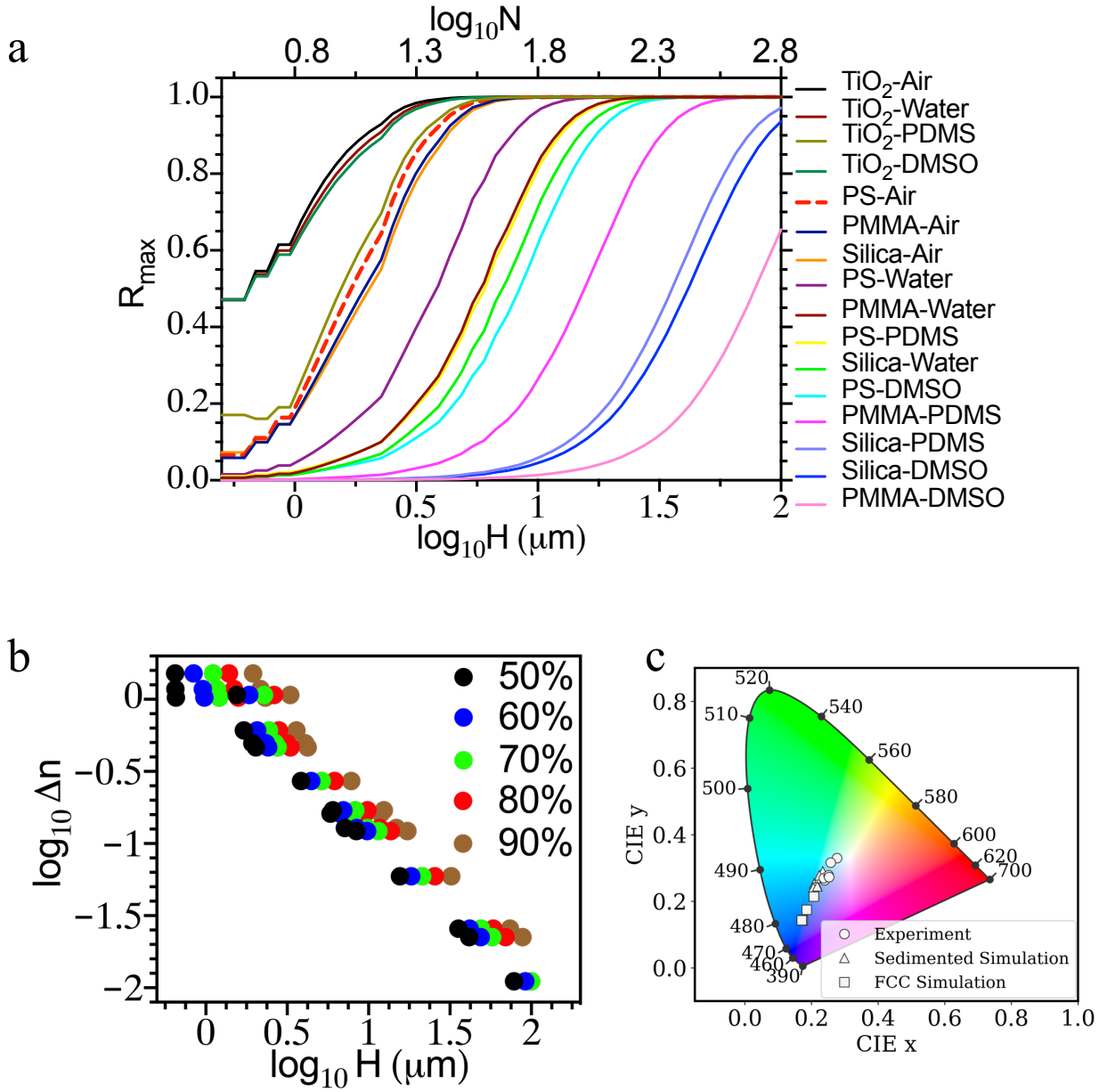

Figure 2-6. Relationship between film thickness and reflection peak intensity for particle-matrix pairs of different refractive index contrast, and structural color quality of polystyrene colloidal crystals films with different thickness determined by 1931 CIE chromaticity diagram. (a) Effect of film thickness (H) and the number of layers (N) on the reflection peak intensity for particle-matrix pairs of different refractive index contrast. (b) The required refractive index contrast to achieve a particular peak reflectance at different crystal thicknesses, calculated by Bryan VanSaders. (c) 1931 CIE chromaticity diagram of polystyrene colloidal crystals films with different thickness produced by experiment, sedimentation simulation, and the pure FCC crystal.

pairs in structural color materials applications. The results shown in Figure 6a and 6b are calculated from the theory of multilayer reflectors. It is clear that an increased refractive index contrast results in saturation at lower stack thicknesses. This insight is useful for engineering structural color films; when the colloid and matrix refractive index contrast is low, thicker layers must be used to achieve intense structural color. Conversely, the total film thickness (and therefore material used) can be reduced by using colloidal particles with higher refractive index contrasts. For example, TiO_2-Air has very high refractive index contrast (1.51), a film of only 2.9 μm (17 layers) is needed to reach saturation; PMMA-PDMS has low refractive index contrast (0.06) and so a film of 41.7 μm (254 layers) is needed to reach saturation. Figure 6b shows that the relationship between refractive index contrast and the thickness required to achieve a given peak reflectance value (based on the multilayer reflector model) is linear on a log-log scale.

Crystal defect and film thickness influence the color quality of film reflection, which can be determined by using 1931 International Commission on Illumination (CIE) chromaticity diagram. The corresponding color coordinates x and y are calculated from the reflection spectra in Figure 4 by using color matching functions[50] and plotted on the CIE chromaticity diagram. In Figure 6c, as the thickness of colloidal crystal film increases from 1.5 μm to 13.4 μm, the color coordinate moves towards the edge of the plot, suggesting an increase in the color quality. Additionally, the color coordinates of the experimental structures are closer to the center of the plot than either the sedimented simulation or theoretical FCC structures, which indicates that experimental structures have less intense color. This confirms our previous conclusions that defects are detrimental to structural color intensity.

2.5 Conclusions

We address – specifically and quantitatively – how structural color intensity depends on different microstructural features of colloidal crystals. This study shows that microscopic crystal properties are a principal determinant of the structural color response of self-assembled colloids. The paper produces an understanding of the relationships among self-assembly, colloidal crystal properties, and the optical properties of structural color. Our approach of measuring the dependence of macroscopic structural color on microscopic properties of the self-assembled structure (defect content and crystal thickness) is useful because it generates new kinds of data sets for simulation and modeling, as well as suggests mechanisms by which reflective structural color can be controlled and designed for at the microscopic scale. Taken together, these scientific results show that: (i) microscopic crystal defects and film thickness are principal determinants of the structural color response of self-assembled colloids; (ii) commonly observed colloidal defects which reduce crystal density such as SFTs, vacancies, and microcracks reduce structural color intensity; (iii) defects which do not reduce crystal density, such as planar stacking faults and twin boundaries, do not impact structural color intensity; (iv) the tools of scanning electron microscope (SEM), simulation and structural color reflection can be coordinated to discover new features of the complex relationship between self-assembly microstructure and the macroscopic, functional optical response; and, (v) the results generated here can be translated into a range of different conditions of particle size and refractive index contrast. With these new findings and tools in hand, scientific questions about the role that crystalline structures play in determining structural color response can be identified and addressed.

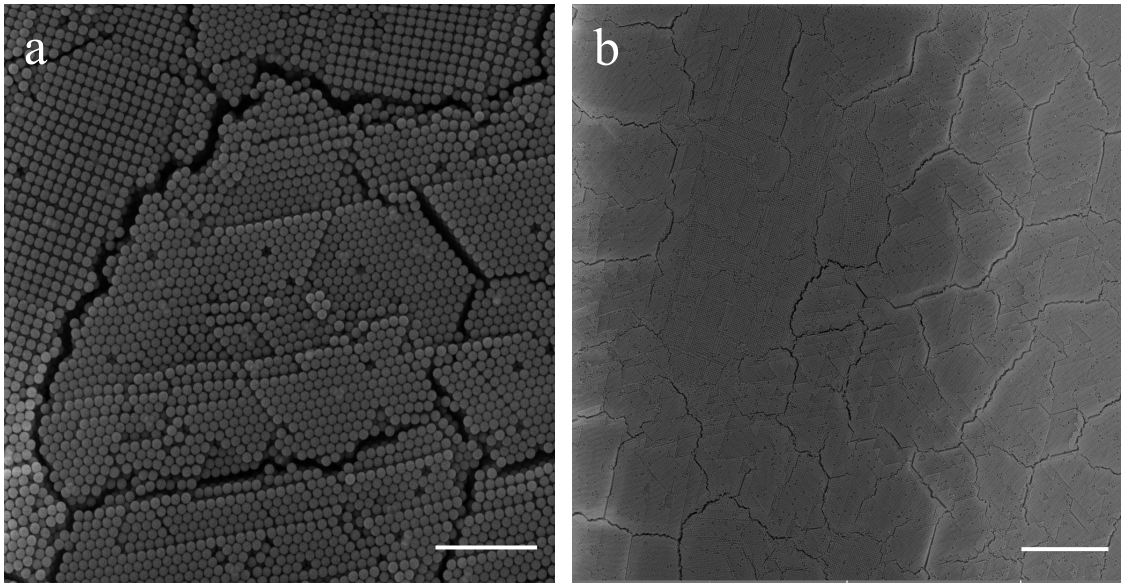

Figure 2-S1. SEM images of the self-assembled colloidal crystals show microcracks of width less than 1 μm. Scale bar in (a) 2 μm, (b) 10 μm.

2.6 References

[1] V. Saranathan *et al.*, "Structure, function, and self-assembly of single network gyroid (I4132) photonic crystals in butterfly wing scales," *Proc. Natl. Acad. Sci.*, vol. 107, no. 26, pp. 11676–11681, Jun. 2010.

[2] J. Zi *et al.*, "Coloration strategies in peacock feathers.," *Proc. Natl. Acad. Sci. U. S. A.*, vol. 100, no. 22, pp. 12576–8, Oct. 2003.

[3] J. V Sanders, "Diffraction of Light by Opals," *Acta Cryst. Acta Cryst. Los Alamos Scientific Lab. Reports Acta Cryst. A24 Acta Cryst*, vol. 22, no. 17, pp. 3056–421, 1967.

[4] S. Kinoshita, S. Yoshioka, and J. Miyazaki, "Physics of structural colors," *Reports Prog. Phys.*, vol. 71, no. 7, p. 076401, 2008.

[5] H. Cong, B. Yu, S. Wang, L. Qi, J. Wang, and Y. Ma, "Preparation of iridescent colloidal crystal coatings with variable structural colors," *Opt. Express*, vol. 21, no. 15, p. 17831, 2013.

[6] F. Meng, M. M. Umair, K. Iqbal, X. Jin, S. Zhang, and B. Tang, "Rapid Fabrication of Noniridescent Structural Color Coatings with High Color Visibility, Good Structural Stability, and Self-Healing Properties," *ACS Appl. Mater. Interfaces*, vol. 11, no. 13, pp. 13022–13028, Apr. 2019.

[7] S. Zhu *et al.*, "Synthesis of Cu-doped WO3 materials with photonic structures for high performance sensors," *J. Mater. Chem.*, vol. 20, no. 41, p. 9126, Oct. 2010.

[8] S. Banisadr, A. Oyefusi, and J. Chen, "A Versatile Strategy for Transparent Stimuli-Responsive Interference Coloration," *ACS Appl. Mater. Interfaces*, vol. 11, no. 7, pp. 7415–7422, Feb. 2019.

[9] H. Fudouzi and Y. Xia, "Colloidal crystals with tunable colors and their use as photonic papers," *Langmuir*, 2003.

[10] A. L. Rogach, N. A. Kotov, D. S. Koktysh, J. W. Ostrander, and G. A. Ragoisha, "Electrophoretic deposition of latex-based 3D colloidal photonic crystals: A technique for rapid production of high-quality opals," *Chem. Mater.*, vol. 12, no. 9, pp. 2721–2726, 2000.

[11] J. J. Juárez, S. E. Feicht, and M. A. Bevan, "Electric field mediated assembly of three dimensional equilibrium colloidal crystals," *Soft Matter*, vol. 8, no. 1, pp. 94–103, Jan. 2012.

[12] H. Míguez *et al.*, "Control of the Photonic Crystal Properties of fcc-Packed Submicrometer SiO2 Spheres by Sintering," *Adv. Mater.*, vol. 10, no. 6, pp. 480–483, Apr. 1998.

[13] M. Echeverri, A. Patil, M. Xiao, W. Li, M. D. Shawkey, and A. Dhinojwala, "Developing

Noniridescent Structural Color on Flexible Substrates with High Bending Resistance," *ACS Appl. Mater. Interfaces*, vol. 11, no. 23, pp. 21159–21165, Jun. 2019.

[14] A. S. Dimitrov and K. Nagayama, "Continuous Convective Assembling of Fine Particles into Two-Dimensional Arrays on Solid Surfaces," *Langmuir*, vol. 12, no. 5, pp. 1303–1311, Jan. 1996.

[15] Y. Meng, J. Qiu, S. Wu, B. Ju, S. Zhang, and B. Tang, "Biomimetic Structural Color Films with a Bilayer Inverse Heterostructure for Anticounterfeiting Applications," *ACS Appl. Mater. Interfaces*, vol. 10, no. 44, pp. 38459–38465, Nov. 2018.

[16] A. Pimpin and W. Srituravanich, "Review on Micro- and Nanolithography Techniques and their Applications," *Eng. J.*, vol. 16, no. 1, pp. 37–56, Jan. 2012.

[17] Y. K. R. Wu, A. E. Hollowell, C. Zhang, and L. Jay Guo, "Angle-insensitive structural colours based on metallic nanocavities and coloured pixels beyond the diffraction limit," *Sci. Rep.*, vol. 3, 2013.

[18] M. E. Calvo, S. Colodrero, T. C. Rojas, J. A. Anta, M. Ocaña, and H. Mı´guez, "Photoconducting Bragg Mirrors based on TiO_2 Nanoparticle Multilayers," *Advanced Functional Materials*, vol.18, no.18, Sep. 2008.

[19] C. Jiang and V. V. Tsukruk, "Freestanding Nanostructures via Layer-by-Layer Assembly," *Adv. Mater.*, vol. 18, no. 7, pp. 829–840, Apr. 2006.

[20] S. N. Fejer and D. J. Wales, "Helix self-assembly from anisotropic molecules," *Phys. Rev. Lett.*, vol. 99, no. 8, Aug. 2007.

[21] A. S. Keys, C. R. Iacovella, and S. C. Glotzer, "Characterizing complex particle morphologies through shape matching: Descriptors, applications, and algorithms," *J. Comput. Phys.*, vol. 230, no. 17, pp. 6438–6463, Jul. 2011.

[22] A. C. Stelson, W. A. Britton, and C. M. Liddell Watson, "Photonic crystal properties of self-assembled Archimedean tilings," *J. Appl. Phys.*, vol. 121, no. 2, Jan. 2017.

[23] A. Somwangthanaroj, E. C. Lee, and M. J. Solomon, "Early Stage Quiescent and Flow-Induced Crystallization of Intercalated Polypropylene Nanocomposites by Time-Resolved Light Scattering," *Macromolecules*, vol. 36, no. 7, Apr., 2003.

[24] M. Ganesan and M. J. Solomon, "High-density equilibrium phases of colloidal ellipsoids by application of optically enhanced, direct current electric fields," *Soft Matter*, vol. 13, no. 20, pp. 3768–3776, May 2017.

[25] J. A. Ferrar and M. J. Solomon, "Kinetics of colloidal deposition, assembly, and crystallization in steady electric fields," *Soft Matter*, vol. 11, no. 18, pp. 3599–3611, 2015.

[26] B. Bharti and O. D. Velev, "Assembly of Reconfigurable Colloidal Structures by Multidirectional Field-Induced Interactions," *Langmuir*, vol. 31, no. 29, pp. 7897–7908, Jul. 2015.

[27] T. Endo, Y. Yanagida, and T. Hatsuzawa, "Colorimetric detection of volatile organic compounds using a colloidal crystal-based chemical sensor for environmental applications," *Sensors Actuators B*, vol. 125, pp. 589–595, 2007.

[28] K. Sano *et al.*, "Photonic water dynamically responsive to external stimuli," *Nat. Commun.*, vol. 7, p. 12559, 2016.

[29] T. S. Shim, S. H. Kim, J. Y. Sim, J. M. Lim, and S. M. Yang, "Dynamic modulation of photonic bandgaps in crystalline colloidal arrays under electric field," *Adv. Mater.*, vol. 22, no. 40, pp. 4494–4498, 2010.

[30] F. Wang, X. Zhang, Y. Lin, L. Wang, and J. Zhu, "Structural Coloration Pigments based on Carbon Modified ZnS@SiO_2 Nanospheres with Low-Angle Dependence, High Color Saturation, and Enhanced Stability," *ACS Appl. Mater. Interfaces*, vol. 8, no. 7, pp. 5009–5016, Feb. 2016.

[31] J. G. Park, S. H. Kim, S. Magkiriadou, T. M. Choi, Y. S. Kim, and V. N. Manoharan, "Full-spectrum photonic pigments with non-iridescent structural colors through colloidal assembly," *Angew. Chemie - Int. Ed.*, vol. 53, no. 11, pp. 2899–2903, 2014.

[32] R. Rengarajan, D. Mittleman, C. Rich, and V. Colvin, "Effect of disorder on the optical properties of colloidal crystals," *Phys. Rev. E*, vol. 71, no. 1, p. 016615, Jan. 2005.

[33] Y.-H. Ye, F. LeBlanc, A. Haché, and V.-V. Truong, "Self-assembling three-dimensional colloidal photonic crystal structure with high crystalline quality," *Appl. Phys. Lett.*, vol. 78, no. 1, pp. 52–54, Jan. 2001.

[34] J. F. Bertone, P. Jiang, K. S. Hwang, D. M. Mittleman, and V. L. Colvin, "Thickness Dependence of the Optical Properties of Ordered Silica-Air and Air-Polymer Photonic Crystals," *Phys. Rev. Lett.*, vol. 83, no. 2, pp. 300–303, Jul. 1999.

[35] J. F. Galisteo-López, E. Palacios-Lidón, E. Castillo-Martínez, and C. López, "Optical study of the pseudogap in thickness and orientation controlled artificial opals," *Phys. Rev. B*, vol. 68, no. 11, p. 115109, Sep. 2003.

[36] G. Q. Liu, Z. S. Wang, and Y. H. Ji, "Influence of growth parameters on the fabrication of high-quality colloidal crystals via a controlled evaporation self-assembly method," *Thin Solid Films*, vol. 518, no. 18, pp. 5083–5090, Jul. 2010.

[37] J. A. Anderson, C. D. Lorenz, and A. Travesset, "General purpose molecular dynamics simulations fully implemented on graphics processing units," 2008.

[38] J. Glaser *et al.*, "Strong scaling of general-purpose molecular dynamics simulations on GPUs," *Comput. Phys. Commun.*, vol. 192, pp. 97–107, Jul. 2015.

[39] A. Stukowski, "Structure identification methods for atomistic simulations of crystalline materials," *Model. Simul. Mater. Sci. Eng.*, vol. 20, no. 4, p. 045021, Jun. 2012.

[40] S. J. Byrnes, "Multilayer optical calculations," *arXiv:1603.02720 [physics.comp-ph]*, Mar. 2016.

[41] C.-C. Lee and C.-J. Tang, "TiO2-Ta2O5 composite thin films deposited by radio frequency ion-beam sputtering," *Appl. Opt.*, vol. 45, no. 36, p. 9125, Dec. 2006.

[42] L. V. Woodcock, "Entropy difference between the face-centred cubic and hexagonal close-packed crystal structures," *Nature*, vol. 385, no. 6612, pp. 141–143, Jan. 1997.

[43] A. Richel, N. P. Johnson, and D. W. McComb, "Observation of Bragg reflection in photonic crystals synthesized from air spheres in a titania matrix," *Appl. Phys. Lett.*, vol. 76, no. 14, pp. 1816–1818, Apr. 2000.

[44] D. E. Aspnes, "Local-field effects and effective-medium theory: A microscopic perspective," *Am. J. Phys.*, vol. 50, no. 8, pp. 704–709, Aug. 1982.

[45] S. Pronk and D. Frenkel, "Can stacking faults in hard-sphere crystals anneal out spontaneously?," *J. Chem. Phys.*, vol. 110, no. 9, pp. 4589–4592, Mar. 1999.

[46] B. Gates, Y. Lu, Z. Y. Li, and Y. Xia, "Fabrication and characterization of photonic crystals with well-controlled thickness and stop-band attenuation," *Appl. Phys. A Mater. Sci. Process.*, vol. 76, no. 4, pp. 509–513, Mar. 2003.

[47] M. Bass, E. W. Van Stryland, D. R. Williams, W. L. Williams, *Handbook of Optics Volume I Fundamentals, Techniques*, Second. New York: McGraw-Hill, INC, 1995.

[48] W. H. Zachariasen, "A general theory of X-ray diffraction in crystals," *Acta Crystallogr.*, vol. 23, no. 4, pp. 558–564, Oct. 1967.

[49] B. Osting, "Bragg structure and the first spectral gap," *Appl. Math. Lett.*, vol. 25, no. 11, pp. 1926–1930, Nov. 2012.

[50] T. Smith and J. Guild, "The C.I.E. colorimetric standards and their use," *Trans. Opt. Soc.*, vol. 33, no. 3, pp. 73–134, Jan. 1931.

Chapter 3 Effect of Particles of Irregular Size on the Microstructure and Structural Color of Self-Assembled Colloidal Crystals

3.1 Abstract

Self-assembled colloidal crystals can exhibit structural colors, a phenomenon of intense reflection within a range of wavelengths caused by constructive interference. Such diffraction effects are most intense for highly uniform crystals, however in practice colloidal crystals may include particles of irregular size, which can reduce the quality of the crystal. Despite their importance in realizing high-quality structural color, a quantitative relationship between particles of irregular size, crystal quality, and the resultant structural color response remains unclear. In this study we systematically and quantitatively investigate the effect of adding particles of irregular size on the microstructural quality and structural color reflectivity of colloidal crystals formed by evaporative self-assembly via experiment and simulation. We examine two sizes of irregular particles, 4.2 times larger or 0.4 times smaller than the host crystal. We find that small irregular particles are more detrimental to crystal quality and structural color reflectivity than large irregular particles. When incorporated with 10% volume fraction of irregularly sized particles, the reflectivity of crystal films with large (small) irregularly sized particles decreases by 18.4% ± 5.6% (27.5 ± 5.8%), and a measure of crystal quality derived from FFT analysis of SEM images reduced by 40.0 ± 4.5% (48.8 ± 6.0%). By modeling colloidal films incorporated with irregular particles via molecular dynamics simulation and computing the reflection spectra of the modeled crystals

via the finite-difference time-domain method, we find that the peak reflectivity of the assembled structures increases monotonically with crystallinity, and that crystallinity is correlated with the volume fraction of incorporated irregular particles. The quantitative relationships developed in this study can be applied to predict the level of irregularly sized particles that can be tolerated in colloidal films before significant degradation in crystal quality and reflectivity occurs.

This chapter was adapted from a manuscript: Tianyu Liu, Bryan VanSaders, Jacob T. Keating, Sharon C. Glotzer, and Michael J. Solomon. " Effect of Particles of Irregular Size on the Microstructure and Structural Color of Self-Assembled Colloidal Crystals", in preparation. Tianyu Liu and Michael J. Solomon conceived the research and designed experiments. Tianyu Liu and Jacob T. Keating conducted the experiments. Bryan VanSaders and Sharon C. Glotzer desgined the computer simulations. Bryan VanSaders performed the simulations.

3.2 Introduction

The technique of self-assembly offers a simple and low-cost approach to produce large-area colloidal crystals,[1] which exhibit optical properties such as structural color. Structural color is the enhanced reflection of light of specific wavelengths due to submicron dielectric periodicity in a material.[2] Unlike coloring due to pigments, it is not prone to degradation by light and heat.[3], [4] The environmental stability of structural color is well aligned with the needs of a variety of optical applications such as coatings[5], sensors[6], and filters[7]. A potential limitation of using colloidal self-assembly to produce structural color materials is that standard syntheses of colloids – materials such as silica or polymer latex – are imperfect, with finite size polydispersity. Polydispersity can manifest as a distribution of sizes, or as bimodal distributions with a fraction of ‘irregular’ particles with sizes distinctly different from the intended product. For example, secondary seeds – which are smaller spheres than the primary monosized fraction – can form

during silica regrowth. Contamination of the seeds with large spheres can also be observed during particle synthesis.[8] Previous studies have demonstrated that an increase of polydispersity leads to higher free energy for crystal nucleation of colloidal suspensions,[9] and that more polydisperse particles self-assemble into structures with greater amorphous character, which exhibits a broader and less intense spectral response [10].

Similar to polydispersity, significant populations of irregularly sized particles can perturb the quality of self-assembly by disrupting how colloids pack. Previous studies have found that added irregularly sized spheres generate defects; these defects are detrimental to the structural periodicity of colloidal crystals.[8] Moreover, the presence of defects may also lead to degradation in the optical properties of colloidal crystals[11], especially structural color reflectivity[12]. However, a quantitative and systematic study that correlates the effects of size irregularity with crystal quality and optical reflectivity is lacking.

Quantitatively understanding the effects of irregularly sized particles could have a number of positive effects on materials development and performance. This understanding could inform the specification of size uniformity required in the synthesis of a particular colloidal system so as to achieve a particular structural color reflectivity. Alternatively, the introduction of irregularly sized particles as dopants could be deployed as a tool to control reflectivity. Thus, in order to guide the design of optical materials from colloidal crystals, it is useful to understand how the presence of particles of irregular size affects microstructure, structural order, and optical properties.

Herein, we systematically evaluate the role of irregularly sized particles in determining crystal quality and structural color reflectivity by experiment and simulation. Specifically, we employ evaporative self-assembly and molecular dynamics simulation to produce structures in

which different amounts of added irregular species are incorporated. A major advantage of evaporative self-assembly over other methods is that it allows us to control the level of irregularly sized particles by introducing different sizes and volume fractions of particles. In addition, evaporative self-assembly and other associate evaporative deposition processes offer industry promise because they are scalable to large-scale fabrication of coatings, and the technique is compatible with existing manufacturing processes.[13]

In the experiment, we introduce specific quantities of irregularly sized microspheres into monosized colloidal suspensions. These particles of irregular size are of two types; they are spheres either with either a larger or smaller diameter than the base colloids. In order to avoid the formation of binary colloidal crystals, the relative size ratio of the two mixed particle components is greater than 1.7 in the case of the larger particles and less than 0.58 in the case of the smaller particles.[14] Through evaporative self-assembly, these particles of irregular size are incorporated into three-dimensional colloidal crystals, which exhibit varying degrees of crystal quality. We quantify this crystal quality by processing images from scanning electron microscopy (SEM) acquired at a resolution that resolves defects such as vacancies and stacking faults. In addition, we measure the reflection spectra of the self-assembled films. The volume fraction, crystal quality, and crystal reflectivity are quantitatively correlated to understand their interrelationship. Special attention is paid to comparing the effects of irregularly sized particles that are larger than and smaller than the primary particle from which the crystal has been self-assembled.

We additionally study the self-assembly of colloidal films with incorporated irregular particles by Molecular dynamics (MD)[15]. Simulations of film formation by with ~10^5 particles are carried out with various quantities of irregular particles. For experimental films prepared by evaporative deposition, crystallization and densification are driven by the motion of the liquid-air

interface as drying proceeds. This process was approximated in simulation by interface-driven crystallization between a pair of planes. When studying the formation of microstructural features such as grain boundaries, large system sizes are required to ensure defect distributions are not strongly perturbed by system size effects. Polycrystalline films obtained by simulation are compared with SEM cross-sections of the experimentally derived films.

To quantitatively compare with the measured reflectivity of colloidal films, the optical reflection spectra of the structures assembled through MD are computed with the finite-difference time-domain (FDTD) method. This method is the most widely used approach to model how light interacts with micro and nano-scale structures by solution of Maxwell's equations in the time domain.[16] The reflection spectra are obtained by Fourier transformation to the calculation of the electromagnetic fields.[17] The combination of MD self-assembly simulation and FDTD calculation of the optical response complements the experimental work by allowing auxiliary observation of the relationship between the underlying microstructural properties that mediate the effect of the added irregular particles on the optical reflectivity.

The aim of this study is therefore to quantify the sensitivity of crystal quality and reflectivity to size and volume fraction of irregularly sized particles. If these correlations are available, then, for example, the reflectivity of the colloidal crystal films might be tunable by introducing controlled quantities of irregularly size particles. The results furthermore reveal the importance of size uniformity in achieving high-quality structural color reflectivity in self-assembled colloidal crystals.

3.3 Materials & Methods

3.3.1 Preparation of colloidal crystals containing added irregular particles

Different-sized polystyrene microspheres in 2.6 vol% aqueous dispersions were obtained from Polysciences, Inc. and used as received. The host particles have a diameter of 198 nm ± 8 nm, and the irregular particles have a diameter of 88nm ± 10 nm or 372 ± 10 nm. These mean size and standard deviation values were determined by scanning electron microscopy (SEM) and image analysis. To prepare a specific volume fraction of irregular particles in the mixture of colloidal dispersions (48 μL), a desired volume of 2.6 vol% dispersion of irregular particles was added to a 2.6 vol% colloidal dispersion of host particles. The relative volume ratio of dispersions of host and irregular particles was varied for different samples. The dispersion mixture was sonicated for 5 min to ensure a uniform distribution of particles. The water in the mixed dispersion was removed by centrifugation (14,000 rpm for 10 mins). Then the colloids were dispersed into ethanol (Decon Laboratories, Inc.). The total volume fraction of particles (host + irregular) in the mixed dispersion was kept constant at 5.0% when the different amounts of irregularly sized particles were added.

To produce the device for evaporative self-assembly, a circular silicone isolator (Grace Bio-Laboratories) of 20 mm diameter and 0.5 mm depth was applied to a glass slide substrate, which was cleaned with a UVO cleaner (Model 42, Jelight) for 5 min. Twenty-five μL of the colloidal dispersion was dispensed into the isolator. After evaporation at room temperature, host colloids and the added irregularly sized colloids were assembled into thin-film crystals. We produced a series of thin-films crystals from 3 μm to 9 μm for each volume fraction of irregular particles. To compare the effect of irregular particles on reflectance, we used the linear interpolation method [18] to compute the reflectance values of films at 5.7 μm (35 layers) with different volume fractions of irregular particles (Figure S-1). The evaporative assembly took 8 mins to produce uniform structural color after all ethanol had been evaporated.

3.3.2 Characterization of crystal microstructure and optical properties

A morphological study of the evaporatively assembled microstructure was carried out by scanning electron microscopy (Tescan MIRA3 FEG SEM) imaging of surfaces and cross-sections of the crystals. For the cross-sectional analysis, the samples were cut using a diamond scribe pen to reveal a plane of the assembled film normal to the substrate. The surfaces of the samples were sputtered with thin layers of gold before SEM imaging. The thickness of the films was measured by a stylus profilometer (Dektak XT). The reflection spectra of the assembled microstructures were measured using an Evolution 600 UV–Vis spectrophotometer (Thermo Scientific) at an 8° angle of incidence. The spectrophotometer is equipped with a diffuse reflectance accessory (Labsphere, DRA-EV-600), which is an integrating sphere capable of total reflectance measurement.

3.3.3 Computation of summation of peak prominence

To quantify crystal quality, we analyzed SEM images with the open-source image processing software Fiji (version 2.1.0, downloaded from ImageJ website)[19]. An unsharp mask was applied to the SEM images, and a conjugate image was then produced by Fast Fourier Transform. The FFT image reports the spatial frequency distribution of crystal periodicity, as shown by the bright regions and rings of the image. The azimuthal variation in the intensity profile was then calculated in the following way: the pixel intensities in the FFT image were summed over an angular interval of 1° between 0° and 360°, where 0° is arbitrarily located. This intensity profile varies with angle as per the location of diffraction peaks. To assess this variability, we determine the intensity over a radial region (ring) that spans the width of the diffraction peaks. For the first order diffraction this ring includes six peaks; for the second order diffraction there are twelve peaks. We focus on the second order ring for analysis here, because the first order ring is often compromised by high background. We set the radial width of the second order diffraction

ring to be 28 pixels to include the full width of all twelve peaks. The intensity profile as a function of angle shows multiple peaks. For SEM images taken under different brightness, we removed the baseline of each intensity profile for the comparison of different structures. The peak prominence in the intensity profile of an FFT image is defined as the difference between the peak maximum and the peak base. On each side of the peak, there is a nearest local minimum. The higher one of the two local minima is the peak base. The peak base is the higher one of two local minima near the peak.[20] The summation of peak prominence is the sum of the peak prominence of all twelve peaks of the second order diffraction.

A hexagonal FFT pattern from structures with no added irregular particles (Figure 1A) has 12 peaks in the second-order diffraction ring. The corresponding intensity profile shows intense peaks (Figure 1C), indicating high structural order. On the other hand, the system with 10% irregular particles incorporated generates an FFT pattern that is more radially symmetric (Figure 1B), and with less intense and broader peaks (Figure 1C). The summation of peak prominence for each intensity profile is frequency-space characterization of the crystal quality of the structure.

3.3.4 Molecular dynamics simulation and optical reflectivity calculation

Colloidal films were simulated via molecular dynamics (MD) using the package HOOMD-Blue (v2.9).[21], [22] Particles were modeled as repulsive spheres using the Shifted Lennard-Jones potential:

$$V_{SLJ}(r) = \epsilon\left[\left(\frac{\sigma}{r-\Delta}\right)^{12} - \left(\frac{\sigma}{r-\Delta}\right)^{6}\right] \quad (1)$$

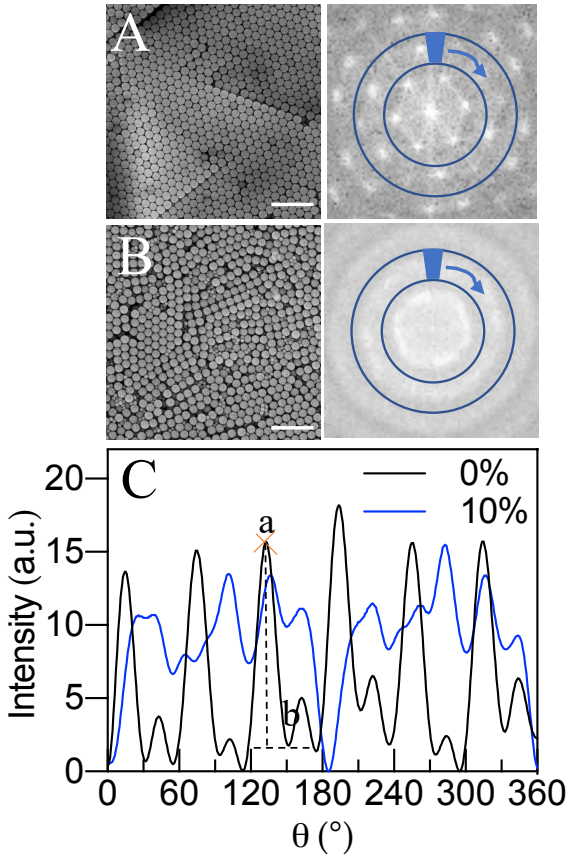

Figure 3-1. Method to compute the summation of peak prominence from SEM images. Representative SEM and FFT images of monosized crystal (A) and structures with added 10% of 88 nm sized irregular particles (B). The scale bars in (A) and (B) are 1 μm. In the FFT image, the pixels in the highlighted ring (covering the second-order diffraction pattern) were summed over an angular interval of 1° between 0° and 360°. Their azimuthal intensity profiles are shown in (C). The prominence of a peak is the difference between the peak maximum (a) and the peak base (b). The summation values of peak prominence for the monosized crystal and the structure with added 10% 88 nm sized irregular particles are 102.1 and 50.0, respectively.

For $r < r_{cut} + \Delta$, and 0 otherwise. $\Delta = (d_i + d_j)/2$, where d_i and d_j are the diameters of the particles being considered. For pure repulsive interactions, r_{cut} was set to $\sigma 2^{\frac{1}{6}}$, and the potential was shifted in energy by ϵ. σ was set to 0.5, and ϵ to 1. d_i were chosen so as to produce a distribution of sizes consistent with the experimental distribution of particle sizes. Fractions of larger or smaller diameter particles – corresponding to the levels used in the experiments – were also included.

In order to model crystal formation by solvent evaporation, domains of $\approx 350k$ particles were simulated with a Langevin integrator in a simulation box with periodic x and y boundaries, but repulsive walls confining the sample in the z-direction. After initial fluidization (with $\frac{kT}{\epsilon} = 1$), the temperature was gradually reduced to zero as the top confining wall was incrementally lowered, pinning the fluid in a gradually diminishing gap. This process represents the boundary-driven densification of the colloidal suspension, corresponding to conditions in which colloids are packed into denser configurations as the liquid surface retreats due to evaporation. In the simulation, the maximum viral pressure experienced by particles was capped at a fixed value ($\frac{P\sigma^3}{kT_{fluid}} = 1.25$). If system pressure exceeded this value, lowering of the top wall was halted and only resumed if system pressure dropped.

Like the experiments, the molecular dynamics simulations are time-dependent, and densification rate is a critical parameter of the protocol. Correspondence between simulated rates and experimental rates is determined by choice of simulation units. Self-consistent simulation units are mapped to SI units by three fundamental conversion factors, indicating the relationship between simulated distances, masses, and energies and their SI counterparts, denoted D, M, and E. In this study, we equated particles simulated by the shifted Lennard-Jones potential to

polystyrene nanoparticles of diameter 200 nm and density 1.04g/cm^3. For the energy unit, we used the gravitational potential energy of such a particle immersed in water lifted by its own diameter. With these units established, the simulation time conversion factor is expressed as $T = \sqrt{MD^2/E}$. Time steps have a value of $dt = 3.25 \times 10^{-5}\ s$.

In addition to the hard-core repulsion between particles, at the later stages of sample drying weak adhesive interactions arise between particles because they are compressed into close contact. To represent this, a shifted Lennard-Jones potential with $r_{cut} = 2.5\sigma$ and $\epsilon = 1$ was added (in addition to the purely repulsive potential already discussed). This potential resulted in weak interparticle adhesion. To accommodate any contraction that resulted from this interparticle adhesion, the system was allowed to reduce the x and y extent of the periodic domain in order to maintain constant internal virial pressure. Once a relaxed dense configuration was reached, a final expansion of the simulation box in the x and y directions was used to crack the sample in a manner consistent with observed film shrinkage, as discussed in the results. In order to assess the crystal quality of the formed layers, particles were assigned a local crystal structure (face-centered cubic, hexagonal close-packed, or disordered) by adaptive common neighbor analysis (aCNA).[23] System crystallinity is the fraction of particles with identifiable crystalline environments (i.e. not disordered). The description of MD simulation was adapted from our manuscript.

A finite-difference time-domain (FDTD) method was used to compute the reflection spectra of simulated structures. The FDTD method is a well-developed computational approach to modeling how light interacts with micro and nano-scale dielectric structures. By breaking up the object and the space surrounding it into small cells, the method solves the Maxwell equations to determine the electromagnetic (EM) field as a function of time. The outputs include spectral responses in reflection and transmission, both of which can be obtained from a single

simulation.[24] The FDTD method is particularly suitable for stimulating structures with submicron-sized features.[25] The simulation was performed with a commercial simulation software package (Lumerical FDTD Solutions). The structures simulated by HOOMD-Blue were inputs to the optical simulation. The refractive index in the computation was set to match the properties of polystyrene. The light source is a pulsed Gaussian beam with a plane wave spatial support. The angle of the incident light was 8°, which is consistent with the integrating sphere experimental configuration. The dimensions of simulation box were x = 20 μm, y = 20 μm, z = 8 μm. The directions parallel to the boundary (x and y axes) satisfied periodic boundary conditions, and the wall normal direction (z-axis) satisfied perfect matched layer (PML) boundary conditions, since the structure has a finite thickness in this direction.

3.4 Results and Discussions

To investigate how added irregular particles generate disorder in structural color colloidal crystals, we prepared, as per the methods, self-assembled structures in which spheres of size larger and smaller than the base (host) colloids were incorporated and compared these to the structures formed with base colloids only. Figure 2 shows SEM images (top view and cross section) for the three cases. In Figure 2A, the colloidal crystal comprised solely of base particles displays highly regular order. Figure 2B reports results at the same self-assembly conditions but with 10 vol% of large irregular particles incorporated. Because of their large size, the irregular particles substitute for several base colloids in the lattice. Visually, the structural order is only modestly affected, although some vacancies and stacking faults are observed. The comparable results for added 10 vol% small (88 nm) irregular particles are reported in Figure 2C, which shows a more amorphous particle packing. Comparison of the SEM images indicates that at fixed volume fraction, small irregularly sized particles generate more disruption of the structural periodicity than the larger

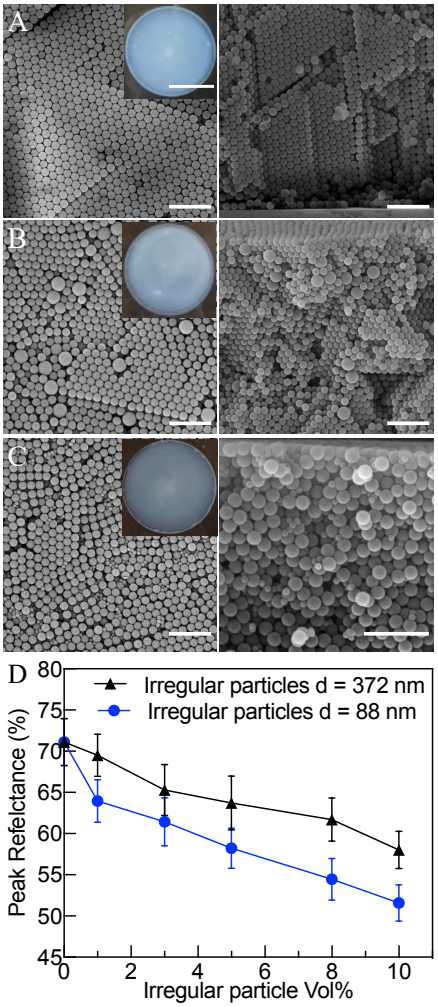

Figure 3-2. Surface view (left), cross-sectional SEM images (right), and photographs (inset) of colloidal crystals without irregular particles, with large irregular particles, and with small irregular particles. (A) Colloidal crystals formed from monodispersed polystyrene spheres of 198 nm diameter. (B) Imperfect crystals formed from 198 nm polystyrene spheres with 10% volume fraction of 372 nm polystyrene spheres added. (C) Imperfect crystals formed from 198 nm polystyrene spheres with 10% volume fraction of 88 nm polystyrene spheres added. Scale bars of SEM images are 1 μm, the scale bar of inset photographs is 10 mm. (D) Peak reflectance of colloidal crystals as a function of added irregular particle volume fraction.

particles do. The difference appears related to the fact that at a fixed volume fraction the number of small irregular particles is more than 75 times greater than that of the large irregular particles. An amorphous structure is produced as a consequence. The photographs of specimens (insets in Figure 2A-C) are consistent with their microstructures that the amorphous colloidal film with 10% small irregular particles displays the lowest brilliance of structural color.

We compared the effect of irregular particle volume fraction on the reflectivity of colloidal films for the larger and smaller additives (Figure 2D). The experimental results show that increasing the concentration of irregularly sized particles leads to a monotonic decrease in reflectance. Small irregular particles have a more significant influence on optical properties than the larger ones. For instance, upon adding 10% small particles the reflectance is decreased by 27.5 ± 5.8%; upon adding 10% large irregular particles, it is decreased by 18.4% ± 5.6%. Thus, structural disorder resulting from irregular particles reduces the reflectivity of colloidal crystals by up to about 20%; particles smaller than the base lattice have a greater effect than those which are larger. In addition, we compared the reflection spectra of films at thickness 5.7 ± 0.6 μm with different volume fractions of large (Figure S-2A) and small irregular particles (Figure S-2B). We find that the full width at half maximum (FWHM) generally increases with the increasing volume fraction of irregular particles. Taken together, these results show that irregular particles disrupt both the intensity and purity of structural color.

To evaluate the microstructural order, we transform top-view SEM images into FFT images and further compute the summation of peak prominence from the FFT intensity profiles. We use this quantity to study the relationship among irregular particle concentration, structural order, and reflectivity. The measure characterizes FFT peak intensity relative to baseline in a particular radial ring of diffraction peaks; it has been used in a number of instances[26], [27] to quantity order from

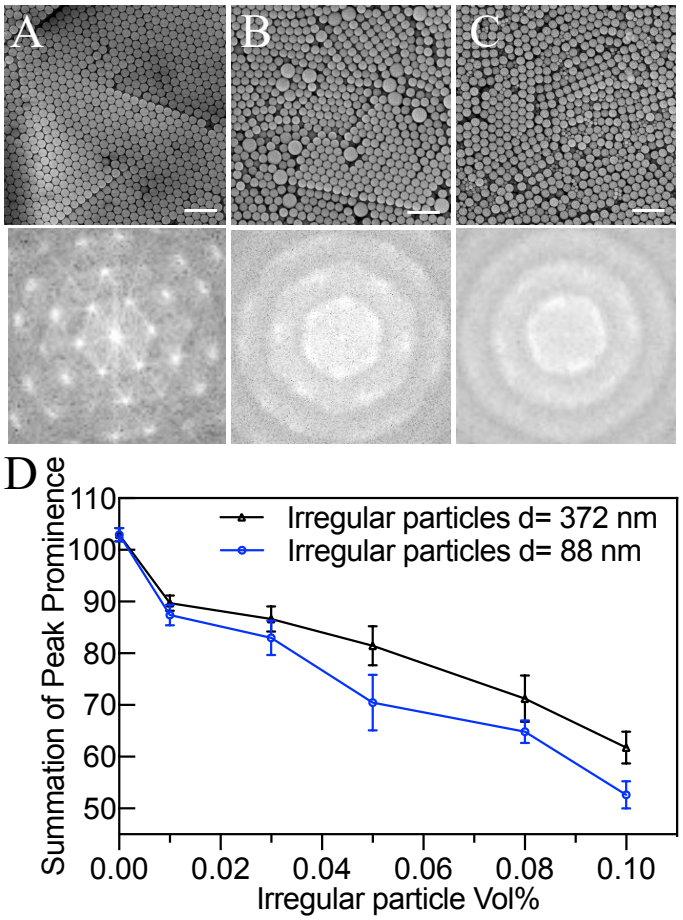

Figure 3-3. SEM images, FFT images, and summation of peak prominence of different structures formed from different amounts of added irregular particles by experiment. SEM (top) and FFT (bottom) images of assembled structures from (A) monosized 198 nm polystyrene spheres, (B) 198 nm polystyrene spheres with 10 vol % of 88 nm polystyrene spheres added, (C) 198 nm polystyrene spheres with 10 vol % of 372 nm polystyrene spheres added. The scale bars in SEM images are 1 μm. (D) Summation of peak prominence (arbitrary units), computed as in the methods, of the FFT intensity profiles as a function of added irregular particle volume fraction.

FFT images.

Figure 3A-C reports SEM images and FFT images of different structures formed from different amounts of added irregular particles. The FFT power spectrum of the crystals of just the base particle size shows a six-fold diffraction pattern in the first ring and a twelve-fold pattern in the second ring. These are characteristic of close-packed, monodomain ordering (Figure 3A). Structures with added irregular particles are less visually ordered, as per the SEM images. The FFT images likewise exhibit rings that are more diffuse relative to the base crystal's diffraction pattern (Figure 3 B, C). Thus, the intensity of the FFT diffraction peaks is correlated with crystal quality. We quantity the former with the summation of peak prominence measure, computed as described in the Materials and Methods section.

Figure 3D shows that the summation of peak prominence computed from the FFT images of the self-assembly crystals deteriorates progressively as the volume fraction of irregularly sized particles increases. This direct relationship was quantified for structures with either large or small particles of irregular size. At a fixed volume fraction of irregularly sized particles, the small particles lead to a lower summation of peak prominence than large ones. At the highest volume fraction (10%), the deviation is 9.1 ± 4.1. The difference is not statistically significant ($p = 0.057$). We note that although the small particles trend below, the difference between the two curves is statistically modest. The error bars on the plot are the result of five replicates of structures for each volume fraction of irregular particles.

To understand how added irregular particles generate reduced crystal quality and structural color reflectivity, we simulated self-assembly with molecular dynamics at the same size and volume fraction of base and irregular particles as the experiments. Figure 4 shows the top view of

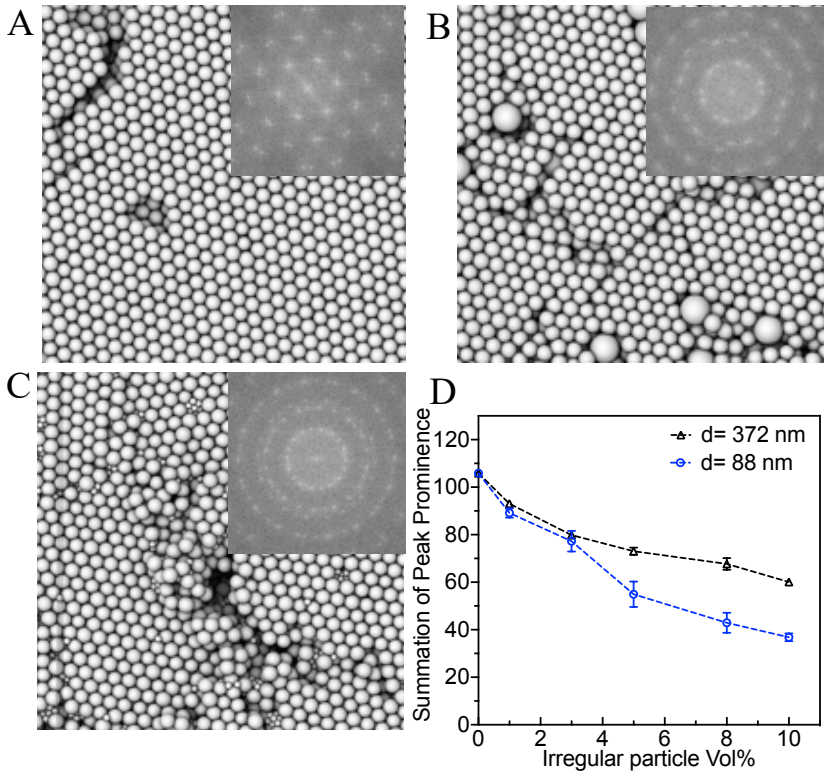

Figure 3-4. Simulated microstructures, FFT images, and summation of peak prominence of structures with different amounts of irregular particles. Simulated crystals consist of 198 nm spheres with (A) no added irregular particles, (B) 10 vol % of added 372 nm spheres, and (C) 10 vol % of added 88 nm spheres. The structures were generated by Bryan VanSaders. (D) Summation of peak prominence of the FFT intensity profiles of simulated structures with different added volume fractions of irregular particles.

simulated structures with solely monosized particles (A), with a 10% volume fraction of large particles of irregular size (B), and with 10% volume fraction of small particles of irregular size (C). The simulation images were analyzed with the same image analysis method as the experiments to determine the summation of peak prominence, the measure of overall crystal quality. In the simulations, the difference of summation of peak prominence between structures with small and large particles of irregular size is about the same at low volume fraction but grows larger as the volume fraction of irregular particles is increased. The summation of peak prominence of the simulations decreased by 43.3 ± 1.2 % and 65. 2 ± 4.6% after the structures were added with 10 vol% large and small particles, respectively. The trends in the simulations agree well with the experimental results. In both experimental and simulation results, we find that crystal quality (quantified by summation of peak prominence) was affected by both the volume fraction and size of irregular particles.

Particles of irregular size in colloidal systems introduce structural disorder into the structures produced by molecular dynamics, which causes their simulated reflectivity to decline. In Figures 5A and 5B, we correlate the volume fraction of irregularly sized particles with the peak reflectance of structures. Here we include a kinetic analysis, which shows that the molecular dynamics results tend to the results of the experiments for comparable rates of film formation. For structures generated at a particular simulation time, peak reflectance decreases as the volume fraction of irregularly sized particles increases for systems with large irregularly sized particles (Figure 5A) and small irregularly sized particles (Figure 5B). As the simulation film formation time is increased from 3 secs to 8 mins (the same as in the experiment), the peak reflectance of simulated structures approaches the experimental value. Figure 5 establishes additional congruence of the simulations and experiments; not only do trends in the summation of peak

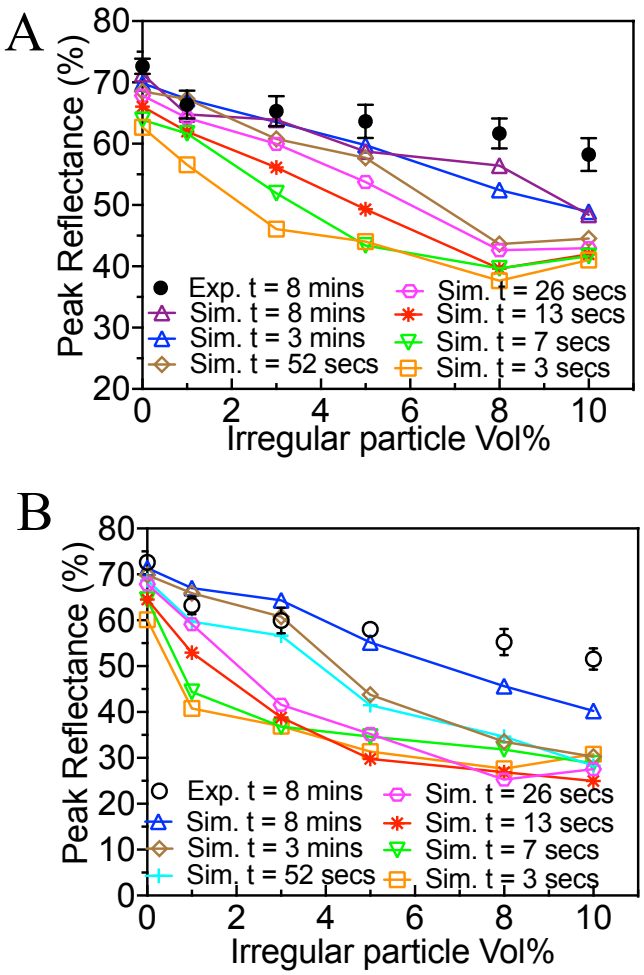

Figure 3-5. Time-dependence of simulated peak reflectance of colloidal crystals with large (A) and small (B) irregular particles. In (A) and (B), experimental values are also plotted.

prominence agree (Figure 4), but simulated particle configurations also exhibit structural color are comparable to experimental values (Figure 5). Figure 6 plots peak reflectance versus crystallinity in the simulated self-assembled systems. The plot generates a master curve that is monotonically increasing. (Crystallinity was computed by common neighbor analysis, as described in the method.) The simulations allow the crystalline fraction of the self-assembled structures to be measured in a way that is not possible in the experiments, since SEM can only be performed on the surface and in the cross section. The crystallinity of simulated structures was tuned by simulation time (Figure S3, Supporting Information). The crystallinity of the self-assembled structures increases with simulation time. The simulations at all the time points and all volume fractions of irregular particles were aggregated, and the crystallinity and reflectivity of each were computed. Figure 6 plots these data, yielding a number of findings. First, reflectivity and crystallinity are directly correlated. This result holds for particles of irregular size that are both large and small. Second, the curves for each irregular particle volume fraction progressively shift to lower reflectivity and lower crystallinity as the volume fraction of irregularly sized particles increases. Third, irregular particles of smaller size yield lower reflectivity at fixed crystallinity fraction relative to the irregular particles of large size. For example, when compared at fixed irregular particle volume fraction, systems with small irregularly sized particles (black curve for 5% irregular particle) have peak reflectance values that are about 8.1% lower than those with large irregularly sized particles (blue curve, also for 5%). These results may indicate that small irregular particles can fill the void space of crystal structure, and thus the refractive index contrast between layers decreases. According to the multilayer reflection theory, a decrease in refractive index contrast leads to a lower reflectance.[28]

Although, as discussed previously, the crystallinity of the experimental samples could not be measured, the summation of peak prominence is available from both experiment and simulation.

The trends in the summation of peak prominence in Figure 2D (experiment) and in Figure 3D (simulation) are comparable. The comparison suggests that the difference in the peak prominence of the experiments is also due to the different crystallinity of the materials with different volume fractions of irregular particles. Since peak prominence and structural color reflectivity are also strongly correlated, the degree of crystallinity is by inference a critical factor in determining the optical properties of the self-assembled materials. Therefore, taking the findings of Figure 5 and Figure 6 together, the presence of irregularly sized particles leads to a decay in the reflectance of assembled structures, and small irregularly sized particles have a more profound influence on optical properties than larger ones. The irregular particles generate their effects on reflectivity by impacting crystal quality, as measured by the intensity of crystal diffraction. This effect on crystal quality is the consequence of the irregular particles reducing the crystallinity of the base structure.

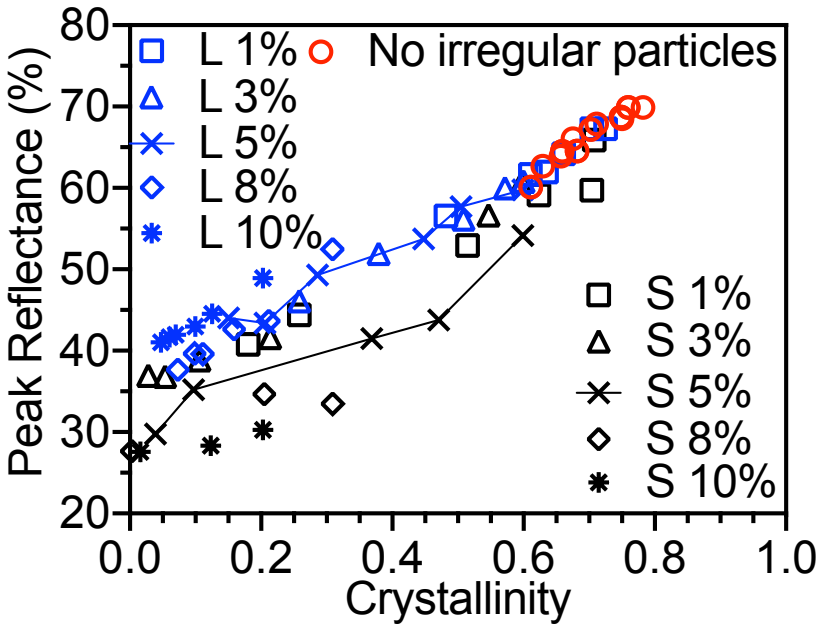

Figure 3-6. Master curve of peak reflectance versus crystallinity for all simulated crystals with different volume fractions of irregular particles ("S" refers to small irregular particles, "L" refers to large irregular particles).

3.5 Conclusions

We have quantitatively studied the influence of irregularly sized particles on structural order and optical properties of self-assembled colloidal films. These findings can guide the design of optical reflectivity in colloidal systems containing particles of irregular size. These irregularly sized particles, which are incorporated during the process of evaporative assembly, lead to less intense structural color reflectivity. The loss of reflectivity is correlated with a loss of crystal quality, as measured by the prominence of diffraction peaks in the FFT of real space SEM images. Simulations confirm that the diffraction peak prominence is a function of the crystallinity of the self-assembled crystals. Thus, mechanistically, irregular size particles decrease the crystalline fraction of the base colloidal crystal. This decrease is apparent in the diffraction peak prominence, which itself correlates with the measured structural color reflectivity. In addition, irregular particles of small size create more defects than large irregular particles, and therefore, at fixed volume fraction, they are more detrimental to the optical reflectivity. This study has discovered and verified design rules that relate structural color reflectivity to the underlying quality of the crystal structure that produces the color. The crystal quality can be controlled by varying the volume fraction and the size of irregularly sized particles. The results can yield a road map applicable to the design of new optical materials with tailored reflectivity.

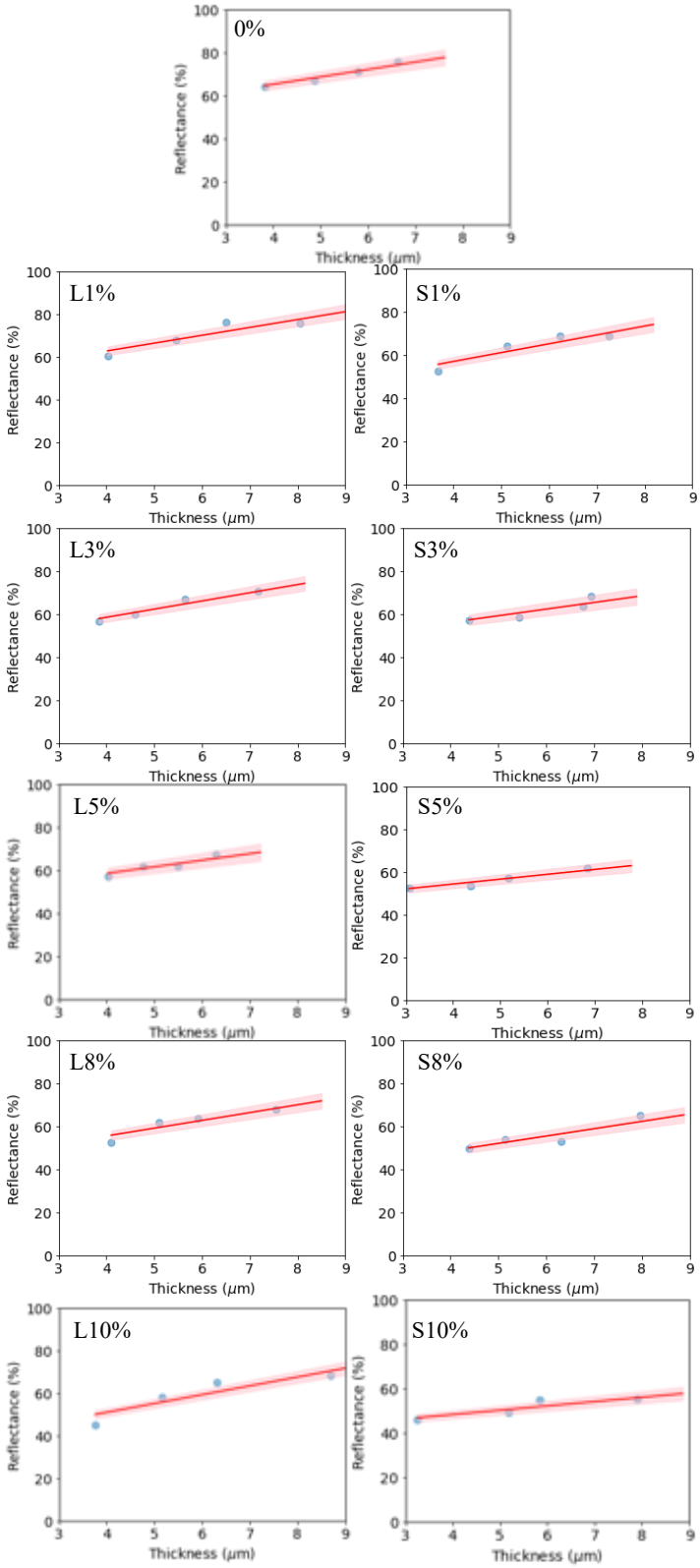

Figure 3-S1. Reflectance of 5.7 μm-thick colloidal films with different volume fractions of irregular particles was computed using linear interpolation. “L” and “S” refer to large and small irregular particles, respectively.

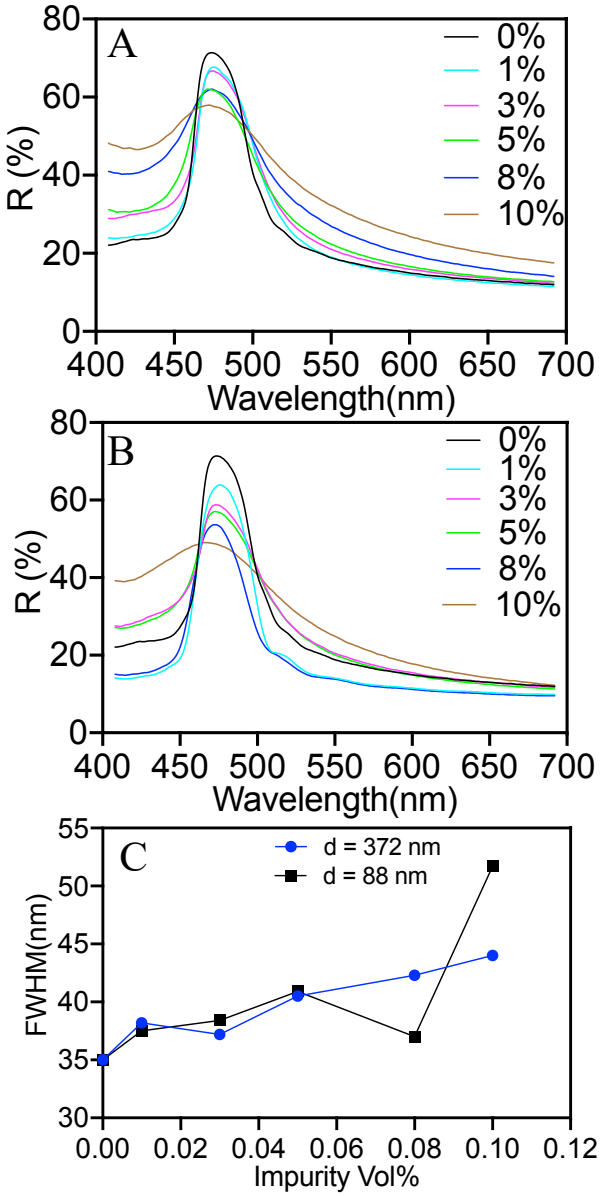

Figure 3-S2. Reflection spectra and full width at half maximum of colloidal films with different volume fractions of irregular particles. Reflection spectra of colloidal films with different volume fractions of large (A) and small (B) irregular particles. The thicknesses of these films are 5.7 ± 0.6 µm. (C) Full width at half maximum (FWHM) of the reflection spectra shown in (A) and (B).

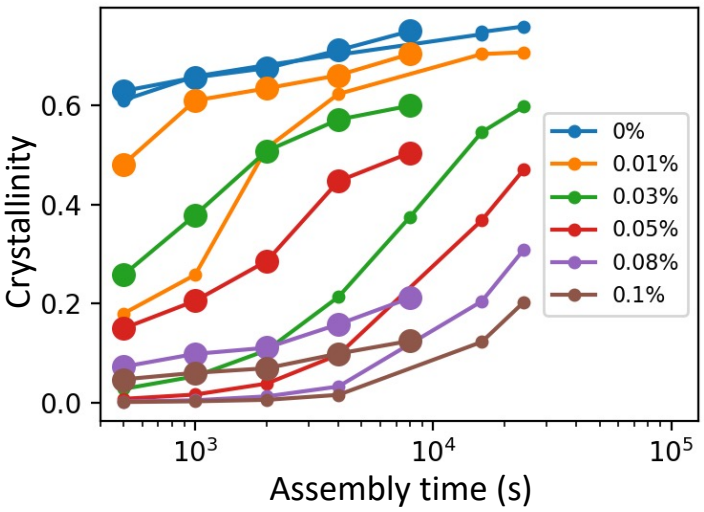

Figure 3-S3. The correlation of crystallinity and simulation time of colloidal systems with different volume fractions of irregular particles, produced by Bryan VanSaders. The curves with larger (smaller) dots represent the system added with 372 nm (88nm) spheres.

3.6 References

[1] B. Hatton, L. Mishchenko, S. Davis, K. H. Sandhage, and J. Aizenberg, "Assembly of large-area, highly ordered, crack-free inverse opal films.," *Proc. Natl. Acad. Sci. U. S. A.*, vol. 107, no. 23, pp. 10354–9, Jun. 2010.

[2] G. Jacucci, S. Vignolini, and L. Schertel, "The limitations of extending nature's color palette in correlated, disordered systems," *PNAS*, vol. 117, p. 2020, 2010.

[3] P. Liu *et al.*, "Self-assembled colloidal arrays for structural color," *Nanoscale Adv.*, 2019.

[4] Y. Zhao, Z. Xie, H. Gu, C. Zhu, and Z. Gu, "Bio-inspired variable structural color materials," *Chem. Soc. Rev.*, vol. 41, no. 8, p. 3297, 2012.

[5] K. Katagiri, Y. Tanaka, K. Uemura, K. Inumaru, T. Seki, and Y. Takeoka, "Structural color coating films composed of an amorphous array of colloidal particles via electrophoretic deposition," *NPG Asia Mater.*, vol. 9, no. 3, pp. 1–4, 2017.

[6] L. Shang, W. Zhang, K. Xu, and Y. Zhao, "Bio-inspired intelligent structural color materials," *Mater. Horizons*, 2019.

[7] N. Suzuki, E. Iwase, and H. Onoe, "Micropatterning of Multiple Photonic Colloidal Crystal Gels for Flexible Structural Color Films," *Langmuir*, vol. 33, no. 24, pp. 6102–6107, Jun. 2017.

[8] S. Wong, V. Kitaev, and G. A. Ozin, "Colloidal Crystal Films: Advances in Universality and Perfection," *J. Am. Chem. Soc.*, vol. 125, no. 50, pp. 15589–15598, 2003.

[9] S. Auer and D. Frenkel, "Suppression of crystal nucleation in polydisperse colloids due to increase of the surface free energy," *Nature*, vol. 413, no. 6857, pp. 711–713, 2001.

[10] R. Rengarajan, D. Mittleman, C. Rich, and V. Colvin, "Effect of disorder on the optical properties of colloidal crystals," *Phys. Rev. E*, vol. 71, no. 1, p. 016615, Jan. 2005.

[11] R. D. Pradhan,, I. I. Tarhan, and G. H. Watson. "Impurity modes in the optical stop bands of doped colloidal crystals." *Physical Review B*, vol. 54, no. 19, pp. 13721, Nov. 1996.

[12] T. Liu, B. Vansaders, S. C. Glotzer, and M. J. Solomon, "Effect of Defective Microstructure and Film Thickness on the Reflective Structural Color of Self-Assembled Colloidal Crystals," *ACS Appl. Mater. Interfaces*, vol. 12, no. 8, pp. 9842–9850, Feb. 2020.

[13] H. Li, P. Wu, G. Zhao, J. Guo, and C. Wang, "Fabrication of industrial-level polymer photonic crystal films at ambient temperature Based on uniform core/shell colloidal particles," *J. Colloid Interface Sci.*, vol. 584, pp. 145–153, Feb. 2021.

[14] J. L. Russell, G. H. Noel, J. M. Warren, N.-L. L. Tran, and T. E. Mallouk, "Binary Colloidal Crystal Films Grown by Vertical Evaporation of Silica Nanoparticle Suspensions," *Langmuir*, vol. 33, no. 39, pp. 10366–10373, Oct. 2017.

[15] B. Vansaders, "Reconfiguring Colloidal Solids with Defects Using Active Matter," *Reconfiguring Colloid. Solids with Defects Using Act. Matter*, 2019.

[16] S. L. Manoto, C. Mabena, R. Malabi, S. Ombinda-Lemboumba, and P. Mthunzi-Kufa, "Design and FDTD simulation of photonic crystal based sensor for biosensing applications," in *Frontiers in Biological Detection: From Nanosensors to Systems XI*, vol. 10895, p. 35, 2019.

[17] O. Hess, C. Hermann, and A. Klaedtke, "Finite-difference time-domain simulations of photonic crystal defect structures," *Phys. Status Solidi Appl. Res.*, vol. 197, no. 3, pp. 605–619, 2003.

[18] Scikit-learn: Machine Learning in Python, Pedregosa et al., JMLR 12, pp. 2825-2830, 2011.

[19] J. Schindelin *et al.*, "Fiji: An open-source platform for biological-image analysis," *Nature Methods*, vol. 9, no. 7. Nature Publishing Group, pp. 676–682, Jul. 2012.

[20] P. Virtanen, R. Gommers, T. E. Oliphant, M. Haberland, T. Reddy, D. Cournapeau, ... & P. van Mulbregt, (2020). SciPy 1.0: fundamental algorithms for scientific computing in Python. *Nature methods*, vol. 17, no. 3, pp. 261-272, Mar. 2020.

[21] J. A. Anderson, C. D. Lorenz, and A. Travesset, "General purpose molecular dynamics simulations fully implemented on graphics processing units," *J. Comput. Phys.*, vol. 227, no. 10, pp. 5342–5359, May 2008.

[22] J. Glaser *et al.*, "Strong scaling of general-purpose molecular dynamics simulations on GPUs," *Comput. Phys. Commun.*, vol. 192, pp. 97–107, Jul. 2015.

[23] A. Stukowski, "Structure identification methods for atomistic simulations of crystalline materials," *Model. Simul. Mater. Sci. Eng.*, vol. 20, no. 4, p. 045021, Jun. 2012.

[24] S. D. Gedney, *Introduction to the Finite-Difference Time-Domain (FDTD)) method for electromagnetics*, vol. 27. 2011.

[25] A. C. Taflove Susan Hagness and B. I. London, "Computational Electrodynamics The Finite-Difference Time-Domain," *Artech House,* 3*,* Jun. 2000.

[26] and J. A. J. Shang, Shuhuan, Fang Yang, Xiangrong Cheng, X. Frank Walboomers, "The effect of gesture on persuasive speech," *Eur. Cells Mater.*, vol. 19, pp. 180–192, 2010.

[27] M. S. Sidhu, P. Munjal, and K. P. Singh, "High-fidelity large area nano-patterning of silicon with femtosecond light sheet," *Appl. Phys. A Mater. Sci. Process.*, vol. 124, no. 1, pp. 1–5, 2018.

[28] C. J. R. Sheppard, "Approximate calculation of the reflection coefficient from a stratified medium," *Pure Appl. Opt. J. Eur. Opt. Soc. Part A*, vol. 4, no. 5, pp. 665–669, Sep. 1995.

Chapter 4 Structural Color Spectral Response of Dense Discoid Packings Generated by Evaporative Self-Assembly

4.1 Abstract

Structural color – optical response due to light diffraction or scattering from submicron scale dielectric periodicity – is a promising candidate for sustainable coloration in materials and coatings. To explore the scope for expanding the functionality of this spectral response, we introduce shape anisotropy into the dielectric building blocks, and characterize how the reflection peak intensity and spectral bandwidth of structural color can be engineered. Uniaxial compression of spheres is used to prepare a set of discoidal particles with homologous variation in shape anisotropy and particle size. The discoids are self-assembled into thin films (thickness = 1.5 μm) by means of evaporation. We examine the effect of discoid aspect ratio and find that the structural color of the self-assembled films displays a component due to diffuse backscattering and one due to multilayer reflection. As the discoids become more anisotropic, the reflection peak height becomes progressively smaller and the bandwidth broader. Decreasing the aspect ratio of the discoid also results in a more disordered structure, as observed by electron microscopy and Monte Carlo simulation. This disorder suppresses the multilayer reflection peak, resulting in structural color that is predominantly from diffuse backscattering. We further show that structural color can be shifted from blue to red when produced from packings of discoids of fixed aspect ratio but variable size. Finally, we find that structural color produced from discoid structures has a low

angular dependence, which is consistent with the disordered packings of discoids. We corroborate our results by comparing the experimentally determined microstructures with Monte Carlo simulations as well as the reflection spectra calculated by finite-difference time-domain simulation. Our findings demonstrate that the two tunable geometries of discoid particles – size and aspect ratio – generate different effects on the spectral response and therefore can function as independent design parameters which expand possibilities for producing non-iridescent structural color by means of colloidal assembly.

This chapter was adapted from a manuscript: Tianyu Liu, Tianyu Liu, Fengyi Gao, Sharon C. Glotzer, and Michael J. Solomon. "Structural Color Spectral Response of Dense Discoid Packings Generated by Evaporative Self-Assembly", in preparation. Tianyu Liu and Michael J. Solomon conceived the research and designed experiments. Tianyu Liu and Tianyu Liu conducted the experiments. Fengyi Gao and Sharon C. Glotzer designed the computer simulations. Fengyi Gao performed the simulations.

4.2 Introduction

Structural color arises from the physical interactions of light with submicron structures. In living systems, such coloration is often produced by means of building blocks that are packed into layered structures. Examples in the natural world include butterflies[1], beetles[2], and cephalopods[3]. Numerous studies have recapitulated structural color in artificial systems.[4]–[8] Structural color is potentially applicable to materials and coatings because this coloration mechanism is more durable and poses a lower environmental burden than pigments and dyes that are conventionally used.[9] There are also additional optical applications for materials displaying structural colors, such as for paints[10], [11], and inks[12].

Structural color can be produced by a variety of mechanisms, including additive manufacturing[13], lithography[14], [15], and self-assembly[16]–[18]. Self-assembly is defined as the spontaneous organization of building blocks and can be accomplished with a variety of materials, including block-copolymers and colloids. Colloids can be assembled into compact packings using a variety of methods such as evaporation[19], electrophoretic deposition[16], sedimentation[17], and dip coating[18]. Compared with other assembly methods, evaporative self-assembly is a simple and cost-effective method to generate dense-packed structures on a large scale.[20]

Colloids can be produced in a variety of shapes, and particle shapes can affect packing structures and the functionality of those structures.[21] Spherical building blocks have been used for structural color in many studies, [22]–[25] while only a few studies have explored structural color using anisotropic colloids[26], [27]. Given the fact that structural color in living systems is often produced from anisotropic building blocks, anisotropic colloidal particles offer strong potential for constructing biomimetic structures. In addition, the particle shape of anisotropic particles can be used as a design parameter additional to particle size for the design of self-assembly and structural color.

One promising type of anisotropic particle to self-assemble for structural color is the discoid particle, which is an oblate spheroid with two long axes of equivalent length. Discoid particles possess simple and well-controlled geometries characterized by two parameters – size and aspect ratio. This kind of anisotropic building block is a good mimic of plate-like proteins found in organisms such as cephalopods, which produce iridescent structural color.[3] Other representative examples of discoid particles include red blood cells[28], drug delivery carriers[29], and encapsulation systems[30].

The packings of discoid particles have been studied by simulation. Disordered packings of discoids can yield a packing density as great as 0.71, which is greater than that for a random close packing of spheres (0.64)[31], [32]. However, it is still unclear how what the spectral responses of such disordered discoid packings are. To address these questions, we produce discoid packings by self-assembly and study their optical reflectivity using both experimental and computational approaches. This study can provide guidance about how to use discoid particles as building blocks to engineer structural colors of particular spectral response.

In this study, we fabricate highly uniform discoid particles by uniaxial compression of spheres embedded in polymers films. The homogeneous deformation caused by the application of controlled compression enables the initially spherical particles to transform into discoids of reproducible aspect ratio. The discoid particles are organized into densely packed films by evaporative assembly. Compared to structures assembled with spheres, the discoid arrays are relatively disordered and therefore have lower structural color intensity; however, the spectral response displays two contributions which are strongly size and aspect ratio dependent in ways that are complex that of spheres, whose response is only size dependent. We use scanning electron microscope (SEM) and UV-Vis spectrophotometry to characterize how discoid aspect ratio and particle size affect the packing and structural color reflectivity of the self-assembled thin films. Reducing the aspect ratio of the discoids results in more disordered structures with different proportions of the diffuse backscattering and multilayer reflectivity contributions to the spectral response. Increasing particle size furthermore leads to a redshift in the reflective spectral response. We demonstrate that the discoid structure also has a low angular dependence of the measured reflectivity due to its disordered packing.

In addition, Monte Carlo (MC) simulations[33]–[35] are used to approximate the conditions of the evaporative assembly of the discoids. The simulated structures are compared to the results of SEM imaging of the thin films and used as inputs for optical simulation by means of the finite-difference time-domain method. The simulated reflection spectra agree well with the experiment and identify the degree of disorder in the discoid packings as the origin of the variable intensity and spectral width of the thin film structural color produced by the discoid packings.

Our work demonstrates that discoid particles and their packings produced by self-assembly are of potential interest as a flexible platform to produce non-iridescent structural colors. The near angular independence of their spectral response is of practical interest for applications such as coatings and paints. The intensity and spectral purity of the structural color may be engineered by controlling the size and aspect ratio of the discoid in ways that are more flexible than for spherical particles.

4.3 Experimental and Simulation Methods

4.3.1 Discoid synthesis

The discoidal particles used in this study were synthesized by uniaxial compression of polystyrene (PS) spheres embedded in polyvinyl alcohol (PVA) films by a Carver benchtop standard heated press（Model 3912) [36]. The unfunctionalized PS spheres (with the size of 215 nm, 258 nm, 286 nm, and 358 nm, standard deviation = 10 nm) were supplied from Bangs Laboratories, Inc. at 10 wt% solid suspension in de-ionized (DI) water with surfactant and sodium azide. Particles in the suspension were washed three times by DI water to remove any remaining stabilizers and soluble impurities. To disperse colloidal spheres into a PVA film, we loaded 0.6 ml of 10% particle suspension into 6.6 ml of 10 wt% aqueous PVA (Mw = 30,000 – 70,000, Sigma-Aldrich, Cat. #P8136). Then the well-mixed PS-PVA solution was transferred to a 35 mm Petri

dish (Fisher Scientific, Cat. #08757100A) and placed in an oven held at 40°C. The PS-PVA composite film was formed by evaporation of the water. A 35 mm dry PS-PVA film was placed between two silicone rubber sheets (Marian, Chicago) and then pressed in the Carver Press at 120 °C (above the glass transition temperature of both PVA and PS) for 25 minutes, resulting in a deformation of spherical particles to discoidal shape. We controlled the aspect ratio of discoids by varying the applied force ranging from 4,450 to 13,300 newton. The squeezed film was allowed to cool to room temperature, and then dissolved in a water/isopropanol mixture (7:3, w/w). Finally, to remove residual PVA, the discoid particles were cleaned five times in DI water by centrifugation. The discoid particles were suspended in water to make dilute suspensions, which were stored at 2-8°C and used within a week. The dimension of the discoid particles was measured by analyzing SEM images with an open-source image processing software Fiji[37]. The major axes (a) of 25 discoid particles were measured. Based on a constant volume assumption, the minor axes (c) were calculated[35]. The dimensions of all the specimens in this study are summarized in Table S1 in the supporting information section.

4.3.2 Discoid evaporative self-assembly

Evaporative deposition was used to assemble the synthesized discoids into thin films. Typically, a glass substrate was pretreated with ultraviolet (UV) light for 7 minutes in a UVO cleaner (Model 42, Jelight). This treatment resulted in the hydrophilic modification that enabled the colloidal suspension to spread uniformly on the substrate. A silicone isolator (Grace Bio-Laboratories) with 13 mm diameter and 0.5 mm thickness was sealed onto the glass substrate to define a solution chamber. The particle suspension was diluted to a volume concentration of 1.0 %, which was determined by hemocytometer counts using confocal laser scanning microscopy. 15 μL of 1.0 vol% discoid suspension in water was loaded into the chamber. Then the sample was placed

Original Sphere Diameter (nm)	Discoid a = b (nm)	c (nm)	Aspect Ratio
215 ± 3	126 ± 1	78 ± 1	0.62 ± 0.01
258 ± 6	148 ± 2	98 ± 1	0.66 ± 0.02
286 ± 8	162 ± 5	112 ± 3	0.69 ± 0.03
286 ± 8	181 ± 4	90 ± 2	0.50 ± 0.02
286 ± 8	210 ± 3	67 ± 1	0.32 ± 0.01
358 ± 10	205 ± 4	137 ± 2	0.67 ± 0.02

Table 4-1. Comparison of discoid particle information. The original sphere size, aspect ratio, length of the major axis (a) and minor axis (c) of the discoid particle used in the experiment are included in this table.

on a leveled table; evaporative assembly occurred at room temperature. After 20 minutes, a dry film consisting of packed discoids was produced.

4.3.3 Microstructural characterization of discoid films

To characterize the microstructural properties of the discoid films, we inspected them using a scanning electron microscope (Tescan MIRA3 FEG SEM). Samples were sputtered with gold before imaging. Coated samples were positioned horizontally on the sample stage. For cross-sectional imaging, samples were cut along their diameter into two pieces and positioned vertically. The electron beam voltage was set at 8kV to achieve the best image quality.

4.3.4 Optical measurement of discoid films

A UV/Vis Spectrometer (model Ocean-HDX-Vis-NIR) was used to measure the reflection spectra of discoid samples. A Tungsten halogen light source (HL-2000-FHSA-LL) coupled with optical fibers and collimating lens, was employed to create a beam of unpolarized and parallel incident light with a beam diameter of 4 mm. The total reflection spectrum was measured by an integrating sphere (ISP-30-6-R) with 8° light incidence relative to the normal plane. This measurement allowed us to collect both specular and diffusive reflection signals. In addition, we used a reflection probe (QR400-7-UV-Vis), with a 6-fiber leg connected to a light source and a 1-fiber leg connected to the spectrometer. This instrumentation allows us to measure the angular dependence of structural color by capturing the diffusive reflection signal at various angles. Reflection spectra of samples were normalized with the total reflection of a polytetrafluoroethylene diffuse reflection standard (WS-1) (The description of optical measurement was adapted from our manuscript). The peak prominence and full width at half maximum (FWHM) values were computed using the scipy.signal.find peaks algorithm.[38] This

algorithm is used to find the local maximum and local minimum by comparison of neighboring values. The peak prominence measures the vertical distance between the peak height (local maximum) and peak base (local minimum). FWHM is the peak width at half the prominence height. In addition, photographs of the discoid specimens were captured under the illumination of a D65 lamp (Philips, TL-D 90), with a 30 cm relative distance and a fixed light incident angle of 8°.

4.3.5 Derivation of color images from measured reflection spectra

The colors consistent with the experimental and simulation reflection spectra were derived via an open-source Python package Colour-Science.[39] Briefly, the computational method is the following: colors perceived by the human eye depend on illumination and receptor cells.[40] To represent a displayed color, the measured reflectance R(λ) is modulated by the illumination spectrum of the D65 Standard Illuminant, as published by the Commission Internationale de l'Eclairage (CIE). The resulting spectrum is transformed to a point in the normalized CIE xyY color space (x and y values define the color hue, and the Y value is the color luminance) via color matching functions. The CIE color matching functions are spectral sensitivity curves of three light detectors which numerically describe the chromatic response of the standard observer.[41] To derive a color image characteristic of a measured reflection spectrum, the CIE xyY point is finally converted to the RGB color space.

4.3.6 Monte Carlo simulation

We perform Monte Carlo simulations of hard anisotropic particles using the hard particle Monte Carlo (HPMC) module of HOOMD-Blue.[42], [43] Specifically, we simulate systems comprised of discoids with different geometries (sizes and aspect ratios) consistent with the materials used in the experiments. We consider only hard interactions between discoids, i.e.,

overlapping particle configurations are forbidden ($U = +\infty$). The system is therefore purely entropic.

In order to model discoid assembly driven by solvent evaporation, domains of $\approx 250k$ particles were simulated using an NVT ensemble in a box with periodic x and y boundaries, and two walls confining the sample in the z-direction. We initialized the systems for self-assembly in a dilute, well-mixed configuration of the particles. We then compressed the systems along the z-direction to a target packing fraction $\phi = 61\%$, representing a process of boundary-driven densification of the colloidal suspension. The target packing fraction was determined to produce a density consistent with the experimental observation that between 5-10 particle layers (for different discoid aspect ratios) were localized in a ~1.5 um-thick film.

Once the target packing fraction was reached, we further equilibrated the systems for at least a million HPMC steps and calculated the normalized packing density profiles afterward. The normalized Z-density profile was evaluated by calculating the packing density of particles in a bin with thickness ΔZ = 10 nm in the Z-direction, normalized by the bulk density. In addition, we characterized the orientational order of the assembled structures by computing the nematic order parameter using the open-sourced freud analysis library.[44] The nematic order parameter is defined as $S = \frac{1}{2}(3\langle\cos^2\theta\rangle - 1)$, in which θ measures the angle between the discoid short axis and the z-axis. The computational workflow and data management for this publication are supported by the signac data management framework.[45] OVITO software is utilized for system visualization.[46] The description of MC simulation was adapted from our manuscript.

4.3.7 Finite difference time domain simulation

The Finite Difference Time Domain (FDTD) method was used to simulate the reflection spectra of the final structures produced by the Monte Carlo simulation. The FDTD simulation was

performed with a commercial software package Lumerical FDTD (Ansys, Inc.). A plane wave with an 8° incident angle was illuminated into a unit simulation cell. X and y directions satisfied periodic boundary conditions, and z-direction was set with perfect matched layer (PML) boundary conditions, since the structure has a finite thickness in the z-direction. By solving the Maxwell equations, the electromagnetic field reflected by the simulation cell was calculated and further transformed into reflection spectra.[47]

4.4 Results and Discussion

Discoid particles were produced from spheres by thermomechanical compression, as shown schematically in Figure 1A and discussed in the methods. Figure 1B shows the SEM image of the synthesized discoids. The dimension of the discoid is characterized by the radius of the major axis (a) and the radius of the minor axis (c). The aspect ratio (l) is defined as the ratio of c/a. Characteristic results of the evaporative self-assembly are reported in Figure 1D; the initial suspension of discoids has a milky white color prior to evaporation. After the solvent evaporates, a dry film consisting of discoids is formed. The dry film of Figure 1D was assembled from discoids with $a = 181 \pm 4$ nm and $l = 0.50 \pm 0.02$. The film displays a blue structural color. The effective measurement area (6 mm in diameter, beam size of spectrophotometer) is labeled with a dashed circle in Figure 1D.

We inspected the microstructure of the film by taking top view and cross-sectional SEM images (Figure 2A). The top view image indicates that the top layer of the discoid packing has local order. However, as shown by the cross-sectional SEM image, discoid particles below the top layer are tilted relative to each other, displaying less orientational ordering.

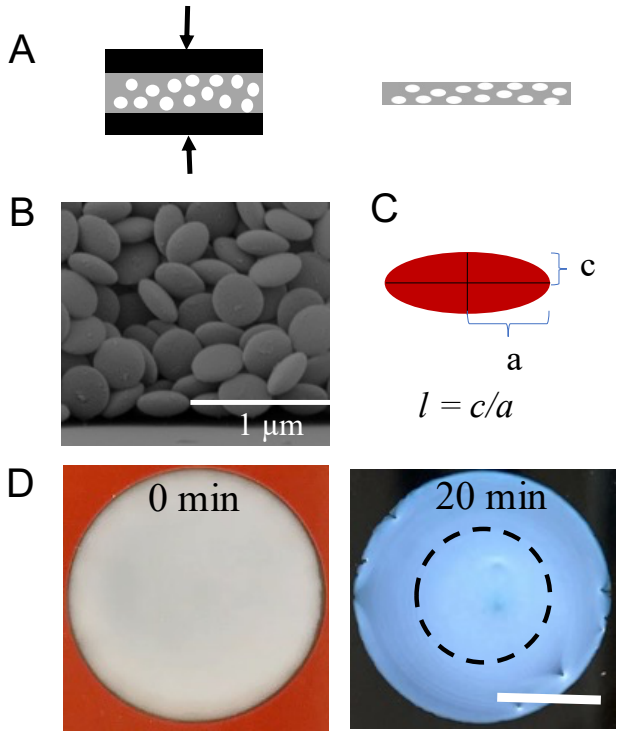

Figure 4-1. Fabrication and self-assembly of discoid particles. (A) Schematic of the fabrication of colloidal discoids by applying a uniaxial compression to polystyrene spheres embedded in a PVA film. (B) Representative SEM image of polystyrene discoids produced by the method. (C) The aspect ratio (l) of a discoid particle is the ratio of the radius of the minor axis (c) and the radius of the major axis (a). (D) Images of discoid sample undergoing self-assembly (a = 181 ± 12 nm, l = 0.50) before and after evaporation. The dotted circle illustrates the effective measurement area of the spectrophotometer. The scale bar is 5 mm.

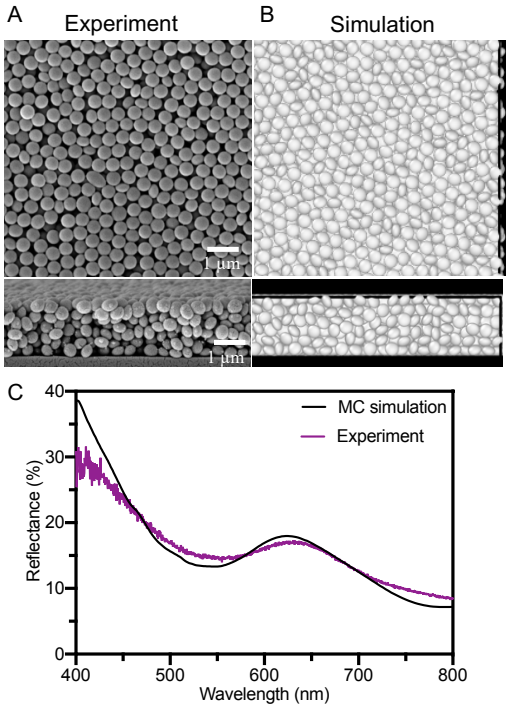

Figure 4-2. Comparison of microstructures and reflection spectra of discoid films produced by experiment and simulation. Top and cross-sectional views of a discoid film (a = 162 ± 12 nm, l = 0.69) produced by evaporative self-assembly. (A) SEM images of the experimental specimen. (B) The comparable structure was generated by MC simulation of the self-assembly, produced by Fengyi Gao. (C) Comparison of the reflection spectra measured by spectrophotometry for the structure in (A) and simulated using the FDTD method for the structure in (B).

Figures 2B reports the results of the Monte Carlo simulations at conditions that yield discoid packing structures that appear similar to those of the experimental SEM images. We computed nematic order parameter of the simulated system and found S = 0.15, indicative of low orientational order. (The value of completely disordered structures is S = 0; a fully aligned packing has S = 1. The nematic order parameter indicates that most of the discoids in the assembled structures are orientationally disordered, with only a few aligned horizontally. These features are consistent with the experimental structures, characterized by SEM.

In Figure 2C, the measured and simulated reflection spectra for the experiments and simulations are reported. The correspondence between the two spectra is high. Both spectra show strong scattering intensity as the wavelength is decreased into the range of 400 nm – 500 nm. At higher wavelengths, both spectra show a peak. For the experiment it is located at 631 nm; for the simulated structure it is at 625 nm. This good agreement between the experiment and simulation spectrum indicates that the combination of MC and FDTD simulation is a good model of the experimental conditions.

To examine the effect of aspect ratio on structural color reflection, we fabricated discoid particles with aspect ratios $l = 0.69 \pm 0.03$, 0.50 ± 0.02, and 0.32 ± 0.01 and compared to the results for spheres. After the sphere or discoid suspensions were evaporatively assembled into thin films, their reflection spectra were measured; results are reported in Figure 3A. Compared with the sphere crystal, discoid packings with higher anisotropy (smaller value of aspect ratio) shows relatively smaller and broader peak reflectivity. The peak prominence and full width at half maximum (FWHM), each computed as per the methods, are reported in Table 2. Color images were derived from the reflection spectra (Figure 3B). These derived colors compare favorably with images of the specimens taken under equivalent, standard illumination (Figure 3C). Decreasing the aspect

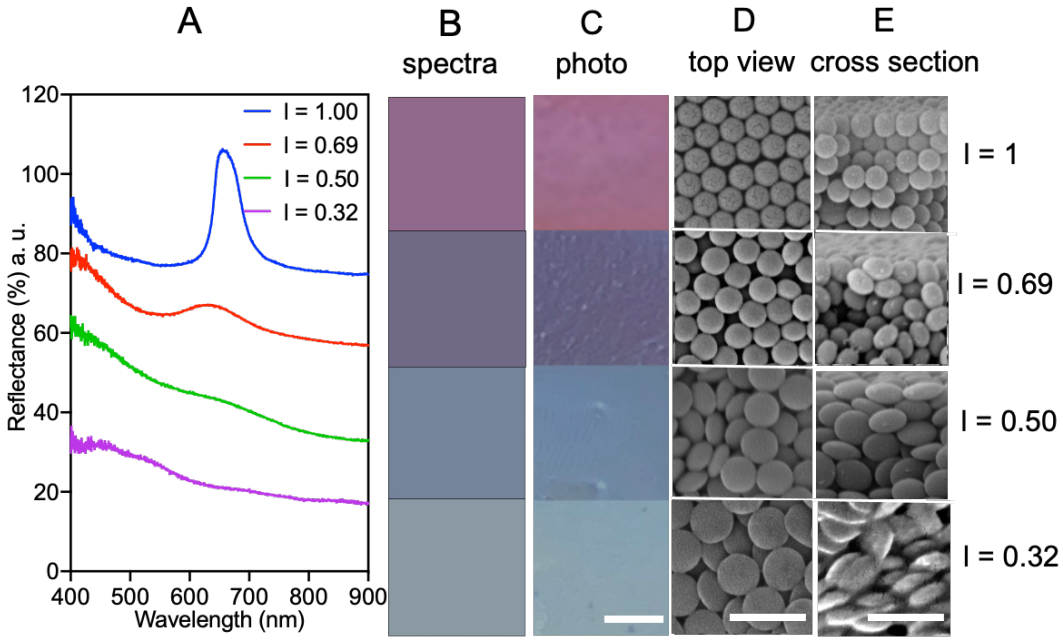

Figure 4-3. Effect of aspect ratio on structural color and microstructures, examined by reflection spectra, photographs, and SEM images. (A) Reflection spectra of the sphere crystal (l = 1) and discoid films with an aspect ratio of 0.61, 0.42, or 0.27, measured by Tianyu Liu. The volume of particles with different aspect ratios is constant, 0.012 μm^3, which corresponds to an initial sphere size of d = 286 nm. (B) Colors derived from the measured reflection spectra in (A). (C) Images of the specimens under the D65 lamp illumination, took by Tianyu Liu; scale bar is 1 mm. The top view (D) and cross section (E) SEM image of discoid films assembled from discoids with different aspect ratios. The scale bar is 1 μm.

Aspect ratio	Wavelength (nm)	Reflection Peak Prominence (%)	FWHM (nm)
1.00	660 ± 3	30 ± 2	53 ± 5
0.61	643 ± 2	4.7 ± 0.4	104 ± 7
0.50	651 ± 7	0.60 ± 0.03	111 ± 6
0.32	ND	ND	ND

Table 4-2. Comparison of peak wavelength, prominence, and full width at half maximum (FWHM) for assembled structures from discoids with different aspect ratios.

ratio of particles results in color shifting from red to purple and finally to blue. Figure 3D and 3E show the top-view and cross-section images for the corresponding aspect ratios. Upon decreasing the aspect ratio, particles become flatter in shape and tend to pack into as a more disordered structure. For the particle size studied (d = 286 nm), light at low wavelengths is strongly scattering due to the nature of disordered particle packing. The backscattering contributes to the blue color of the color image. The peaks with wavelengths at 640-660 nm due to multilayer reflection in the discoid packing contribute to the red color. We will discuss the theoretical calculation of the peak wavelength of multilayer reflection in the section of Figure 5. These results indicate that particle anisotropy affects the relative prominence of the multilayer reflection (red) and backscattering (blue) contributions. The spectral response reveals the origin of the color shift as the aspect ratio is changed. That is, the multilayer reflection peak becomes less intense as the aspect ratio decreases. The purplish hue apparent in the color images is the consequence of the mixing of these spectral contributions. The hue can be controlled therefore by varying the discoid aspect ratio. For discoids with the smallest aspect ratio (l = 0.32), in the extreme case, only blue color from backscattering is observed after the complete disappearance of the multilayer reflection peak.

To further understand the connections among discoid aspect ratio, packing structure, and optical properties, we simulated the reflection spectra and examined the degree of structural order in the discoid packings by studying their Z-axis density profile. Figure 4 A reports the simulated reflection spectra of discoid packings of different aspect ratios as generated via MC simulation and computed by the FDTD method. Upon decreasing aspect ratio l (that is, as the discoid particles become flatter), the reflection peak becomes smaller and broader until it completely disappears when l = 0.32. The consistency between the experiment (Figure 3A) and the simulation (Figure

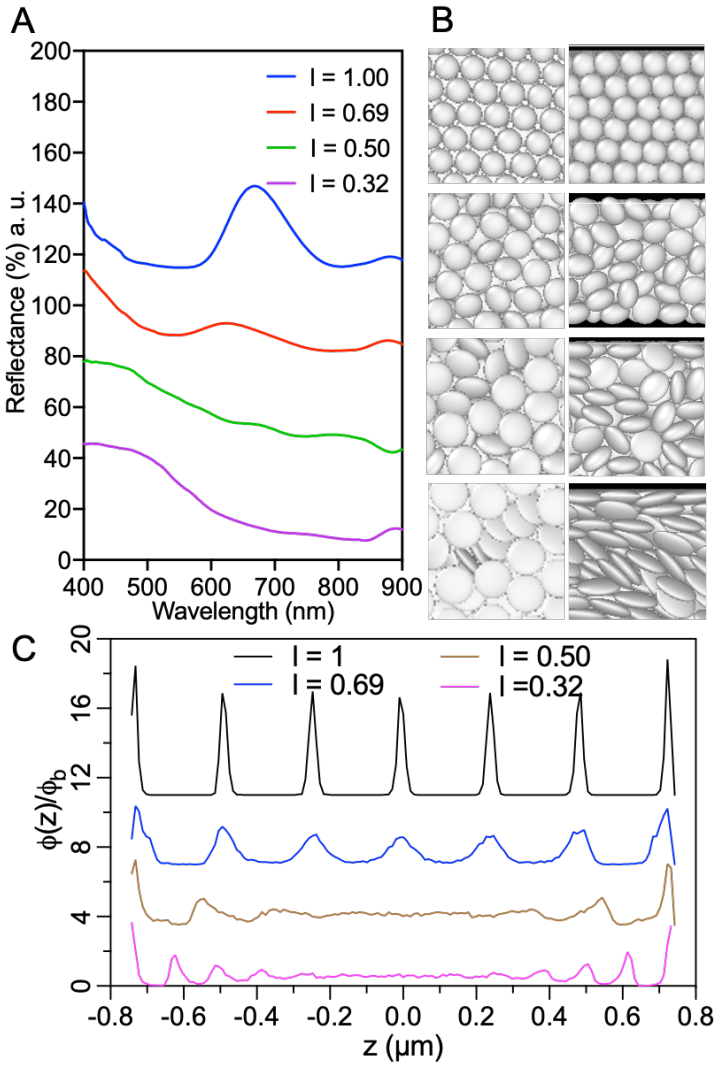

Figure 4-4. Simulated reflection spectra of discoid films consisting of monosized spheres as well as discoids with different aspect ratio (l = 0.69, 0.50, or 0.32). The particle volume is constant at 0.012 μm3 which corresponds to an initial sphere size of 286 nm. (A) Reflection spectra simulated by the FDTD method (B) Snapshots of the Monte Carlo simulation structure used in the FDTD simulation. (C) Normalized and offset Z-density profile of discoid particles confined between two walls for sphere and discoid packings, generated by Fengyi Gao.

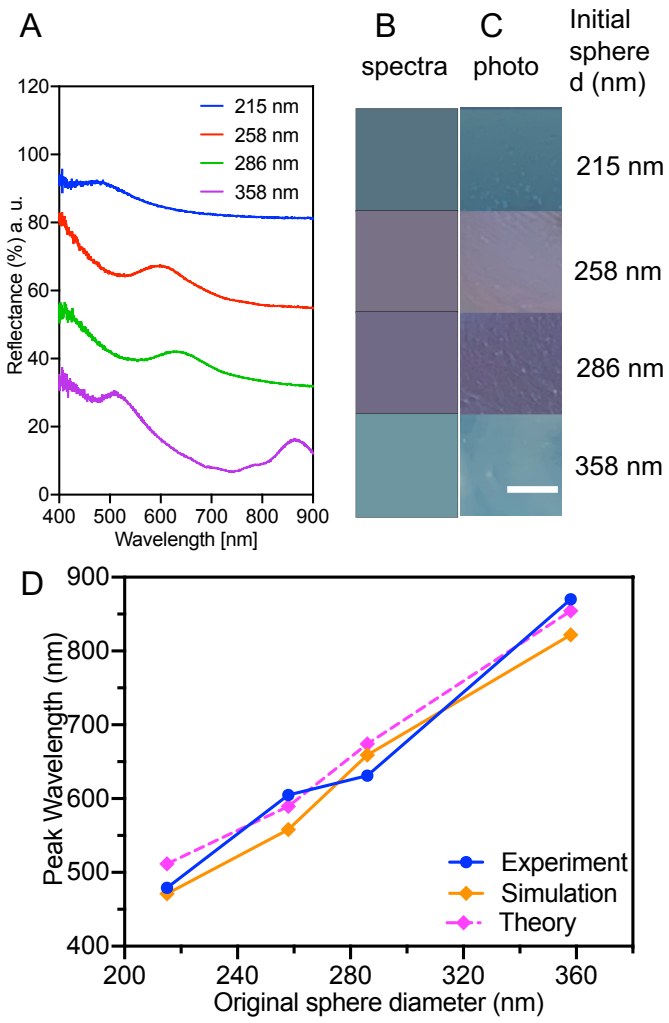

Figure 4-5. Effect of discoid size on structural color, examined by reflection spectra, converted color images, and photographs. (A) Reflection spectra of the dry films of different-sized discoids, synthesized from initial particle diameters of 215 nm, 258 nm, 286 nm, and 358 nm. The aspect ratio of the discoids is 0.69. (B) Colors derived from the measured reflection spectra of A, computed by means of the Methods. (C) Images of sample coloration under illumination with a D65 lamp. The scale bar is 1mm. (D) Experiment, simulation, and theoretical peak wavelengths are compared after being plotted as a function of the initial sphere diameter before deformation.

4A) provides an additional indication that the simulated structures represent experimental structures well.

As shown in the simulation top view and cross-section snapshots (Figure 4B), the discoid microstructures tend to become more disordered as the aspect ratio decreases, consistent with the decrease in the multilayer interference peak of the spectral response. To quantify the structural disorder, we plotted the normalized density profile along the Z-axis for each of the particle aspect ratios studied (Figure 4C). As seen in the Figure, for the structure assembled from spheres and the largest aspect ratio discoid (l = 1.00, l = 0.69), the density profile has multiple peaks with almost equal spacing. This suggests significant positional order along the z-direction, especially for the sphere packing. By contrast, the smaller aspect ratio discoids (l = 0.50, l = 0.32), exhibit a density profile that is almost a flat curve except near the boundaries of the thin film. This finding indicates that the discoid particles are disordered in the center of the film; the only order in the film is in the boundary layers. The constant density profile in the inner region demonstrates that decreasing aspect ratio (increasing anisotropy) leads to a more disordered packing.

We report the effect of discoid size on structural color in Figure 5. Figure 5A shows the reflection spectra of discoid films produced from particles of the same aspect ratio (l = 0.69) but of varying size. The discoids were prepared from spheres of diameters 215 nm, 258 nm, 286 nm, and 358 nm. The curves show contributions from both multilayer reflection and diffuse backscattering, as illustrated previously. The wavelength of the multilayer reflection peak redshifts as the particle size is increased. Additionally, a binary peak was observed size 358 nm discoid sample. In this specimen, the multilayer reflection peak at 870 nm was beyond the range of visible light. The backscattering peak at 520 nm caused by Mie scattering is consistent with the observed cyan color. We derived color images (Figure 5B) under D65 illumination from the measured

spectral response, as per the methods, and compared them to images acquired directly by a camera (Figure 5C). The two sets of images agree well.

In Figure 5D, the peak wavelengths from the experiment, simulation, and Bragg's law model are plotted as a function of the initial sphere diameter. For aspect ratio l = 0.69, discoid packings have distinctive layers with almost equal interlayer spacing (Figure 4C). Thus,. the peak wavelength of discoid packings can be compared to that predicted by Bragg's equation:[19]

$$m\lambda_R = 2d\left[n_{eff}^2 - \sin^2\theta_R\right]^{1/2} \qquad (1)$$

where m is the order of diffraction, λ_R is the reflected wavelength; d is the interplanar spacing; n_{eff} is the effective refractive index, calculated by the relation $n_{eff} = \sqrt{\emptyset n_{ps} + (1-\emptyset)n_{air}}$, where ϕ is volume fraction discoid packing (here ϕ = 0.61 for the simulated discoid packings); and θ_R is the angle of incident light relative to the normal plane. The average interlayer spacing, d, used in eqn (1) for each discoid packing is derived from the simulated density profile in the direction that is perpendicular to the wall, comparable to Figure 4C (the simulation data are reported in Figure S1). First-order diffractions as per eqn (1) are theoretical peak wavelengths of the discoid packings, which agree well with the peak wavelengths measured by the experiment and simulation.

Taken together, Figures 3-5 show that colors of variable hue and intensity can be formed either by varying the size of the discoid and its aspect ratio. We emphasize that the result of varying these two variables is not identical, and this is a direct consequence of the discoid shape. Changing discoid size (at fixed aspect ratio) shifts both the wavelength of the backscattering and multilayer reflection contributions in proportion and keeps their relative magnitudes about the same (Figure 5). Changing discoid aspect ratio (at fixed size) shifts the wavelength only modestly but affects the relative contribution of reflection and backscattering significantly. These are independent

trajectories in the space of the color appearance parameters, and therefore could be combined to create color appearance unavailable if only size alone were available as a design parameter. To further understand and predict the backscattering, future study could use scattering theory to model the aspect ratio and size dependence of discoid particles with disordered and layer structures.

To characterize the angular dependence of the structural color of discoid films, we measured the reflection spectra of films prepared by self-assembly of discoids (l = 0.69, synthesized from the initial spheres with a diameter of 286 nm). As shown in the Figure 6A schematic, we fixed the position of the reflection probe and rotated the sample relative to the probe by angle α. This method is commonly used to measure the diffuse reflection of specimens as a function of viewing angle.[48] Figure 6B shows the reflection spectra for discoid films at angles ranging from 20° to 60°. It can be seen that the reflection intensity drops as the angle α increases. However, the peak wavelength remains almost unchanged, with only a small shift from 641 nm to 626 nm as the angle is changed from 20° to 60°.

The diffuse reflection of the films produced under the same self-assembly conditions with spheres was measured and is reported for comparison with the discoid films (Figure 6C). The peak intensity for sphere films is much stronger than the discoid films. For films of self-assembled spheres, the peak intensity drops significantly with increasing measurement angle. We note that at angles of 20° and above, an interesting dip appears in the reflection spectrum at a wavelength that is between two adjacent local maxima. This local minimum is likely a consequence of the particle ordering in the film, because its position blue shifts from 651 nm to 568 nm as the angle increases from 20° to 60°, consistent with Bragg's law. At this wavelength, most of the incident light propagates out of the sample at Bragg angle; there is thus less light that is scattered diffusively. The reflection spectra in Figure 6C show the diffusive reflection response of spherical crystals by

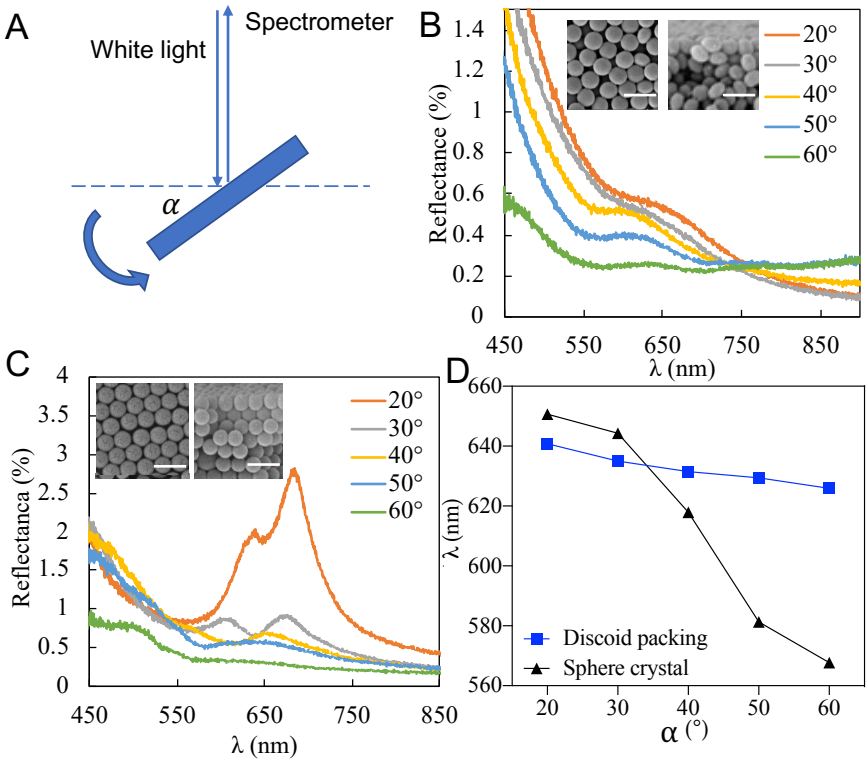

Figure 4-6. Angular dependence comparison between the structural color of discoid films and sphere crystals. (A) Schematic of the experimental device for angular-dependent measurement of diffuse reflectance using a reflection probe with a fixed position. The sample is rotated to accomplish measurements at different angles. The measurement angle α varies from 20 to 60 degrees relative to the plane of the specimen. (B) The reflection spectra for a discoid sample with $l = 0.69$ and (C) for a sphere crystal with $l = 1.00$, measured by Tianyu Liu; both specimens were self-assembled by the same evaporative method. In (B) and (C), the inset images are top view (left) and cross section (right) of SEM images; the scale bar is 0.5 μm; (D) Comparison of angular dependence from the reflection spectra of the self-assembled discoids and spheres.

rotating the sample to different angles. This result shows a similar trend as a previous report of inverse crystals[48].

The quantitative comparison of the angular dependence of the diffusive reflectivity of the sphere and discoid films is shown in Figure 6D. For discoid samples, the relative shift of the measured multilayer reflection peak $\Delta\lambda/\lambda_o$ is only 2% over the angular range probed, whereas the sphere films are shifted by 13%. Thus, the discoid films – which are disordered – display lower angular dependence of the diffusive reflection than spherical films – which are ordered. The ordered crystal planes in the spherical packings reflect light dominantly at the angle identical to the angle of incident light in the opposition direction. The variation in the incident angle relative to certain crystal plane changes, as well as the angle of reflection, leads to high angular dependence of colloidal crystals. However, as characterized by SEM imaging (insets in Figures 6B and 6C), the disordered packing of discoids is nearly isotropic. This feature enables its structural color to be consistent over a wide range of viewing angles. In addition, these results indicate that discoid packings can be used to produce non-iridescent structural color. We note that this feature is an indirect consequence of the discoid shape, rather than a direct consequence. That is, the origin of the angularly independent diffuse scattering is the disordered packing of the discoids. The control sphere film has greater angular dependence because its self-assembled structure is ordered. We would expect similar behavior in both sphere and discoid films if the former were also self-assembled into a disordered structure. The most substantive difference between the discoid and sphere films is therefore the fact that the spectral response of the discoid films shifts with both aspect ratio and size, while that of spheres shifts only with size. Moreover, the functionality of the two shifts in the discoid film spectral response are distinguishable, therefore offering new opportunities to engineer non-iridescent color in thin films produced by colloidal self-assembly.

4.5 Conclusions

In this study, we present facile procedures to synthesize discoid particles with controlled geometries and generate their dense packings by simple evaporation for structural color applications. Similarly, we modeled the experimentally produced structures by Monte Carlo simulation and calculated the reflection spectrum by the FDTD method. Both experiment and simulation approaches were used to examine the effects of aspect ratio and particle size on structural color. We demonstrated that the peak wavelength of structural color increases linearly with increasing discoid size. This peak wavelength is well-approximated by Bragg's law for the average interlayer spacing of the packings, as calculated from the simulated density profile in the wall normal direction. This approximation can be applied to predict the structural color from discoid packings. In addition, we identify that a decrease in aspect ratio (larger anisotropy) results in more broadband multilayer reflection, because the structural color is generated by a relatively increasing contribution from backscattering. These findings indicate that by varying discoid aspect ratio, the multilayer reflection intensity in the structural color response can be tuned independently of the backscattering contribution. This response is ultimately linked to the fact that the layered structure of the packings progressively disappears as the discoid anisotropy increases. The contribution of the backscattering can be understood by applying scattering theory to model aspect ratio and size effects of the anisotropic particles self-assembled into dense thin films. Furthermore, discoid packings are more disordered than spherical crystals produced by the same self-assembly method, and thus produce less angular-dependent structural colors. These non-iridescent structural colors from discoid structures provide color consistency over a wide range of viewing angles, such as required by applications such as coatings and displays. Our study demonstrates that the

tunability of the discoid geometry extends the possibilities for colloidal assembly to create new structures for structural color materials.

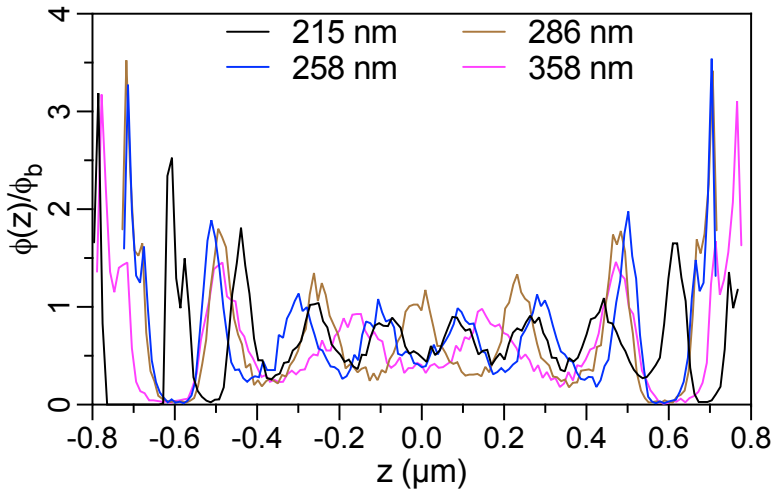

Figure 4-S1. Normalized Z-density distributions of discoid packings from different sized particles confined between two walls, produced by Fengyi Gao.

4.6 References

[1] V. Saranathan *et al.*, "Structure, function, and self-assembly of single network gyroid (I4132) photonic crystals in butterfly wing scales," *Proc. Natl. Acad. Sci.*, vol. 107, no. 26, pp. 11676–11681, Jun. 2010.

[2] A. E. Seago, P. Brady, J. P. Vigneron, and T. D. Schultz, "Gold bugs and beyond: A review of iridescence and structural colour mechanisms in beetles (Coleoptera)," *Journal of the Royal Society Interface*, vol. 6, no. SUPPL. 2. Royal Society, Apr. 2009.

[3] L. M. Mäthger, E. J. Denton, N. J. Marshall, and R. T. Hanlon, "Mechanisms and behavioural functions of structural coloration in cephalopods," *Journal of the Royal Society Interface*, vol. 6, no. SUPPL. 2. Royal Society, Apr. 2009.

[4] H. Fudouzi and Y. Xia, "Colloidal crystals with tunable colors and their use as photonic papers," *Langmuir*, vol. 19, no. 23, pp. 9653–9660, 2003.

[5] J. G. Park, S. H. Kim, S. Magkiriadou, T. M. Choi, Y. S. Kim, and V. N. Manoharan, "Full-spectrum photonic pigments with non-iridescent structural colors through colloidal assembly," *Angew. Chemie - Int. Ed.*, vol. 53, no. 11, pp. 2899–2903, 2014.

[6] Y. Takeoka, "Angle-independent structural coloured amorphous arrays," *J. Mater. Chem.*, vol. 22, pp. 44–45, 2012.

[7] A. A. Shah, M. Ganesan, J. Jocz, and M. J. Solomon, "Direct Current Electric Field Assembly of Colloidal Crystals Displaying Reversible Structural Color," *ACS Nano*, vol. 8, no. 8, pp. 8095–8103, Aug. 2014.

[8] Y. Xia *et al.*, "A New and Straightforward Strategy to Prepare an Optical Hydrogel Film with Dynamic Structural Colors," *J. Phys. Chem. C*, vol. 124, no. 29, pp. 16083–16089, 2020.

[9] Y. Takeoka, "Environment and human friendly colored materials prepared using black and white components," *Chem. Commun.*, vol. 54, no. 39, pp. 4905–4914, 2018.

[10] H. Cong, B. Yu, S. Wang, L. Qi, J. Wang, and Y. Ma, "Preparation of iridescent colloidal crystal coatings with variable structural colors," *Opt. Express*, vol. 21, no. 15, p. 17831, Jul. 2013.

[11] F. Meng, M. M. Umair, K. Iqbal, X. Jin, S. Zhang, and B. Tang, "Rapid Fabrication of Noniridescent Structural Color Coatings with High Color Visibility, Good Structural Stability, and Self-Healing Properties," *ACS Appl. Mater. Interfaces*, vol. 11, no. 13, pp. 13022–13028, Apr. 2019.

[12] J. Ge, J. Goebl, L. He, Z. Lu, and Y. Yin, "Rewritable photonic paper with hygroscopic salt

solution as ink," *Adv. Mater.*, vol. 21, no. 42, pp. 4259–4264, Nov. 2009.

[13] B. M. Boyle, T. A. French, R. M. Pearson, B. G. McCarthy, and G. M. Miyake, "Structural Color for Additive Manufacturing: 3D-Printed Photonic Crystals from Block Copolymers," *ACS Nano*, vol. 11, no. 3, pp. 3052–3058, Mar. 2017.

[14] A. Pimpin and W. Srituravanich, "Review on Micro- and Nanolithography Techniques and their Applications," *Eng. J.*, vol. 16, no. 1, pp. 37–56, Jan. 2012.

[15] Y. K. R. Wu, A. E. Hollowell, C. Zhang, and L. Jay Guo, "Angle-insensitive structural colours based on metallic nanocavities and coloured pixels beyond the diffraction limit," *Sci. Rep.*, vol. 3, 2013.

[16] A. L. Rogach, N. A. Kotov, D. S. Koktysh, J. W. Ostrander, and G. A. Ragoisha, "Electrophoretic Deposition of Latex-Based 3D Colloidal Photonic Crystals: A Technique for Rapid Production of High-Quality Opals," *Chem. Mater.*, vol. 12, no. 9, pp. 2721–2726, Sep. 2000.

[17] H. Míguez *et al.*, "Control of the Photonic Crystal Properties of fcc-Packed Submicrometer SiO2 Spheres by Sintering," *Adv. Mater.*, vol. 10, no. 6, pp. 480–483, Apr. 1998.

[18] A. S. Dimitrov and K. Nagayama, "Continuous Convective Assembling of Fine Particles into Two-Dimensional Arrays on Solid Surfaces," *Langmuir*, vol. 12, no. 5, pp. 1303–1311, Jan. 1996.

[19] H. Fudouzi and Y. Xia, "Colloidal Crystals with Tunable Colors and Their Use as Photonic Papers," *Langmuir*, vol. 19, no. 23, pp. 9653–9660, Nov. 2003.

[20] W. L. Min, P. Jiang, and B. Jiang, "Large-scale assembly of colloidal nanoparticles and fabrication of periodic subwavelength structures," *Nanotechnology*, vol. 19, no. 47, 2008.

[21] S. C. Glotzer and M. J. Solomon, "Anisotropy of building blocks and their assembly into complex structures," *Nat. Mater.*, vol. 6, no. 8, pp. 557–562, 2007.

[22] O. L. Pursiainen, J. J. Baumberg, H. Winkler, B. Viel, P. Spahn, and T. Ruhl, "Nanoparticle-tuned structural color from polymer opals," *Opt. Express*, vol. 15, no. 15, p. 9553, 2007.

[23] Y. Lu, Y. Yin, Z. Y. Li, and Y. Xia, "Colloidal crystals made of polystyrene spheroids: Fabrication and structural/optical characterization," *Langmuir*, vol. 18, no. 20, pp. 7722–7727, 2002.

[24] T. Liu, B. Vansaders, S. C. Glotzer, and M. J. Solomon, "Effect of Defective Microstructure and Film Thickness on the Reflective Structural Color of Self-Assembled Colloidal Crystals," *ACS Appl. Mater. Interfaces*, vol. 12, no. 8, pp. 9842–9850, Feb. 2020.

[25] M. Harun-Ur-Rashid, A. Bin Imran, T. Seki, M. Ishii, H. Nakamura, and Y. Takeoka,

"Angle-independent structural color in colloidal amorphous arrays," *ChemPhysChem*, vol. 11, no. 3, pp. 579–583, 2010.

[26] T. Ding, K. Song, K. Clays, and C.-H. Tung, "Fabrication of 3D Photonic Crystals of Ellipsoids: Convective Self-Assembly in Magnetic Field," *Adv. Mater.*, vol. 21, no. 19, pp. 1936–1940, May 2009.

[27] T. Ding, Z. F. Liu, K. Song, K. Clays, and C. H. Tung, "Photonic crystals of oblate spheroids by blown film extrusion of prefabricated colloidal crystals," *Langmuir*, vol. 25, no. 17, pp. 10218–10222, 2009.

[28] N. Doshi, J. N. Orje, B. Molins, J. W. Smith, S. Mitragotri, and Z. M. Ruggeri, "Platelet mimetic particles for targeting thrombi in flowing blood," *Adv. Mater.*, vol. 24, no. 28, pp. 3864–3869, 2012.

[29] R. Mathaes, G. Winter, A. Besheer, and J. Engert, "Non-spherical micro- and nanoparticles: Fabrication, characterization and drug delivery applications," *Expert Opin. Drug Deliv.*, vol. 12, no. 3, pp. 481–492, 2015.

[30] J. A. Champion, Y. K. Katare, and S. Mitragotri, "Particle shape: A new design parameter for micro- and nanoscale drug delivery carriers," *J. Control. Release*, vol. 121, no. 1–2, pp. 3–9, 2007.

[31] G. Delaney, D. Weaire, S. Hutzler, and S. Murphy, "Random packing of elliptical disks," *Philos. Mag. Lett.*, vol. 85, no. 2, pp. 89–96, 2005.

[32] A. Donev *et al.*, "Improving the Density of Jammed Disordered Packings Using Ellipsoids," *Science (80-.).*, vol. 303, no. 5660, pp. 990–993, 2004.

[33] P. F. Damasceno, M. Engel, and S. C. Glotzer, "Predictive self-assembly of polyhedra into complex structures," *Science (80-.).*, vol. 337, no. 6093, pp. 453–457, 2012.

[34] A. J. Simon *et al.*, "Supercharging enables organized assembly of synthetic biomolecules," *Nat. Chem.*, vol. 11, no. 3, pp. 204–212, 2019.

[35] L. C. Hsiao *et al.*, "Metastable orientational order of colloidal discoids.," *Nat. Commun.*, vol. 6, p. 8507, 2015.

[36] O. Shemi, "Self-Assembly and Self-Propulsion of Colloidal Particles Using Shape and Janus Anisotropy by," 2016.

[37] J. Schindelin *et al.*, "Fiji: An open-source platform for biological-image analysis," *Nature Methods*, vol. 9, no. 7. Nature Publishing Group, pp. 676–682, 28-Jul-2012.

[38] P. Virtanen, R. Gommers, T. E. Oliphant, M. Haberland, T. Reddy, D. Cournapeau, ... & P. van Mulbregt, (2020). SciPy 1.0: fundamental algorithms for scientific computing in

Python. *Nature methods*, vol. 17, no. 3, pp. 261-272, Mar. 2020.

[39] Mansencal, Thomas, Mauderer, Michael, Parsons, Michael, Shaw, Nick, Wheatley, Kevin, Cooper, Sean, … Hill, Stephen. (2020, January 25). Colour 0.3.16 (Version 0.3.16). Zenodo. http://doi.org/10.5281/zenodo.3757045.

[40] C. L. Hardin, "Why color?," in *Perceiving, Measuring, and Using Color*, 1990, vol. 1250, no. 1, pp. 293–300.

[41] M. Shaw and M. Fairchild, "Evaluating the 1931 CIE color-matching functions," *Color Res. Appl.*, vol. 27, no. 5, pp. 316–329, Oct. 2002.

[42] J. A. Anderson, J. Glaser, and S. C. Glotzer, "HOOMD-blue: A Python package for high-performance molecular dynamics and hard particle Monte Carlo simulations," *Comput. Mater. Sci.*, vol. 173, p. 109363, Feb. 2020.

[43] J. A. Anderson, M. Eric Irrgang, and S. C. Glotzer, "Scalable Metropolis Monte Carlo for simulation of hard shapes," *Comput. Phys. Commun.*, vol. 204, pp. 21–30, Jul. 2016.

[44] V. Ramasubramani, B. D. Dice, E. S. Harper, M. P. Spellings, J. A. Anderson, and S. C. Glotzer, "freud: A software suite for high throughput analysis of particle simulation data," *Comput. Phys. Commun.*, vol. 254, p. 107275, Sep. 2020.

[45] C. S. Adorf, P. M. Dodd, V. Ramasubramani, and S. C. Glotzer, "Simple data and workflow management with the signac framework," *Comput. Mater. Sci.*, vol. 146, pp. 220–229, Apr. 2018.

[46] A. Stukowski, "Structure identification methods for atomistic simulations of crystalline materials," *Model. Simul. Mater. Sci. Eng.*, vol. 20, no. 4, p. 045021, Jun. 2012.

[47] S. D. Gedney, "Introduction to the Finite-Difference Time-Domain (FDTD)) method for electromagnetics," *Synth. Lect. Comput. Electromagn.*, vol. 27, pp. 1–250, Jan. 2011.

[48] G. H. Lee, J. Y. Sim, and S. H. Kim, "Polymeric Inverse Glasses for Development of Noniridescent Structural Colors in Full Visible Range," *ACS Appl. Mater. Interfaces*, vol. 8, no. 19, pp. 12473–12480, 2016.

Chapter 5 Conclusions and Future Directions

In this dissertation, we reported the connections between colloidal microstructural properties and structural color. By combining experiment and simulation approaches, we systematically and quantitatively examined the effects of crystal thickness, the density of different defects, irregularity of particle size, and particle shape on structural color properties. These findings provide helpful guidance to tune structural color by controlling colloidal assembly.

In Chapter 2, we addressed how structural color reflectivity quantitatively depended on the film thickness and defect density of different defects in colloidal crystals. We produced colloidal crystals with varying thicknesses by evaporative self-assembly and molecular dynamics simulation. Reflection spectra of experimental crystals and simulated crystals were obtained from UV/Vis spectrophotometry and finite-difference time-domain (FDTD) calculation of optical response. We demonstrated the existence of the critical thickness at which structural color reflectivity reached its maximum. When a crystal film was thinner than the critical thickness, increasing film thickness could efficiently increase reflectivity. In addition, we simulated crystals with particular types of defect structures (vacancies, stacking fault tetrahedra, planar faults, or microcracks). By comparing the reflectivity of structures with different densities of these defects, we found that the reduction of structural color reflectivity was more sensitive to defect density than defect types. Vacancies, stacking fault tetrahedra, and microcracks increased the defect density and further reduced the structural color reflectivity. On the other hand, planar faults led to

no change in defect density and did not impact structural color. This study suggests mechanisms that structural color reflectivity can be designed by controlling crystal thickness and defect density.

Future work could apply this study to increase structural color intensity of colloidal crystals assembled by electrophoretic deposition. Previous studies have reported that a direct current (DC) electric field can be used to assemble colloidal particles into crystals with structural colors. The limitation for structural color by this approach is that the colors are generally faint [1], [2]. Based on our findings that crystal thickness and defects quantitatively affect structural color intensity, it would be of interest to improve structural color by controlling the thickness and defects in colloidal crystals. First, to produce a thick assembled crystal, the initial volume fraction of the colloidal suspension should be increased to a certain level. The applied voltage of direct current should also be optimized correspondingly to ensure enough driving forces. The assembly would take longer due to more particles needing to be packed into crystal structures. Second, the defect density in colloidal crystals could potentially be tuned by controlling the applied voltage during the assembly process. Preliminary results of defect density varied by applied voltages are shown in Figure 5-1. We characterized the assembled structure by a confocal laser scanning microscope. The defect density in a confocal microscope image was computed by counting pixels with zero intensity after the image is binarized (Figure 5-1A-C). Figure 5-1D&E shows that the crystal structure assembled by 2.0V DC field has fewer defects than that by 3.0V. We also plotted defect density as a function of applied voltage in Figure 5-1F. These results suggest that the defect density in an assembled structure could be reduced by applying an optimal voltage. As a result, the structural color intensity would be increased by fabricating a high-quality assembled structure.

In Chapter 3, we quantified the effects of irregularly sized particles on crystal quality and structural color reflectivity of colloidal crystals by experiment and simulation. The irregularly

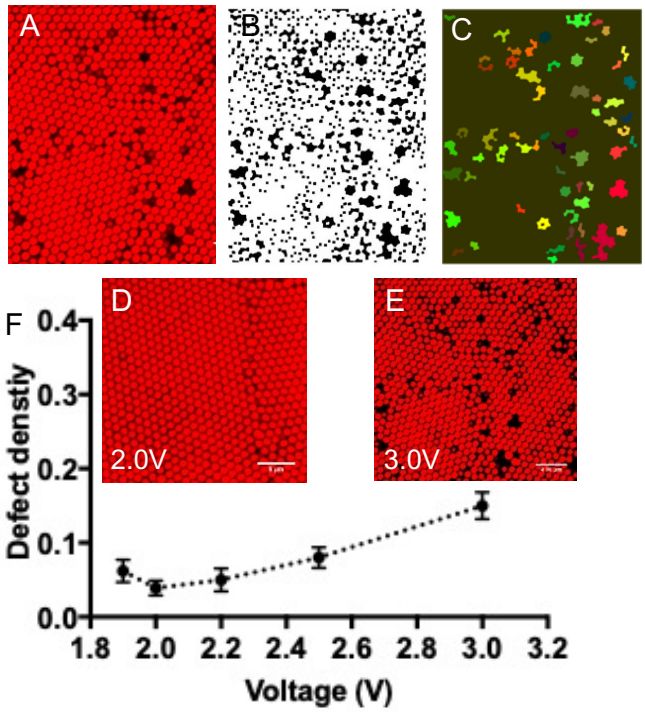

Figure 5-1. Relationship of defect densities of colloidal crystals and the applied voltages of DC electric fields. (A)-(C): computing process of defect density by image analysis; (D)-(E): comparison of defects of the assembled structure at 2.0 V and 3.0 V. The scale bar is 5 μm. (F) The relationship of defect densities of colloidal crystals and the applied voltages of DC electric fields.

sized particles were either smaller or larger than the base colloids of the assembled structures. By varying the amount of introduced irregular particles during the process of evaporative assembly, we fabricated colloidal crystals with different quality, which produced structural color with different reflectivity. Crystal quality was measured by the prominence of diffraction peaks in the FFT of SEM images and rendering images of simulated structures. Both experimental and simulation results showed that irregularly sized particles decreased the crystalline fraction of the assembled structures. Furthermore, irregularly sized particles in the colloidal structures caused degradation in structural color reflectivity, which was measured by spectrophotometry and simulated by the FDTD method. We also compared the effects of large and small irregular particles at fixed volume fractions. Small irregular particles created a more disordered structure and were more detrimental to structural color reflectivity. Our findings provide design rules for structural color by relating it to the underlying quality of colloidal crystals, which can be controlled by volume fraction and size of irregular particles.

To extend this work, the introduced irregular particles could be different materials from base colloids in the assembled structures. Colloidal particles can be synthesized with different material functionality such as core-shell structure [3]–[5]. Core-shell particles include soft polymer shells and hard cores. Future work could characterize how the shells of core-shell particles interact and affect the assembly of base colloids. The introduced core-shell particles may potentially enhance the mechanical properties of crystal film [6]–[8]. By assembling particles above the melting point of shell materials, the shell would form a matrix and hard cores form the crystal structures embedded in the matrix. Thus, the produced crystal films could be flexible and tough with high mechanical strength. In addition, the refractive index contrast of particles and matrix would be changed after the addition of core-shell particles. Then structural color could also be

varied correspondingly based on a similar reflectivity calculation of multilayer materials, which depend on the number of layers and refractive index contrast [9] :

$$R = \left[\frac{n_o(n_2)^{2N} - n_s(n_1)^{2N}}{n_o(n_2)^{2N} + n_s(n_1)^{2N}}\right]^2, \quad (1)$$

where n_0 and n_s are the refractive index of the originating medium and the terminating medium (substrate or backing); n_1 and n_2 are two alternating materials in each layer; N is the number of layers; R is reflectivity. In addition, the effect of varying irregular particle size could be further investigated, since the present work addressed just one irregular size that was larger and another that was smaller.

In Chapter 4, we characterized the particle anisotropy on the microstructure and structural color properties of assembled structures. After synthesizing discoids with different aspect ratios and sizes by uniaxial compression, we produced dense discoid packings by evaporative self-assembly and measured their reflection spectra by spectrophotometry. Similarly, we produced discoid packings by Monte Carlo simulation and simulated their reflection spectra by FDTD simulation. The structural color reflection of a discoid structure could be described as the sum of a backscattering contribution in the short (blue) wavelength range and a multilayer reflection peak at a particular wavelength, typically in the red. By increasing discoid size (radius of major axis) at a fixed aspect ratio, the multilayer peak location was redshifted for a desired wavelength, which could be approximately predicted by Bragg's law with the interlayer spacing of discoid packings. By decreasing the aspect ratio of discoid at a fixed particle size, the multilayer reflection peak could be suppressed. Thus, the structural color was only from backscattering. In addition, we found that structural color produced from discoid structures has a low angular dependence. This non-iridescent structural color meets the needs for some applications such as coatings and displays,

which require color consistency over a wide range of viewing angles. These results demonstrated that two tunable geometries - size and aspect ratio – of anisotropic particles could extend the possibilities of creating a structural color of tailored hue in ways that expand the potential for color engineering.

A challenge of anisotropic assembly is long-range crystallinity. Future work could explore more controllable methods to produce discoids crystals for high structural color intensity. Due to the kinetic effects inherent to the self-assembly process we used, anisotropic particles may be inhibited to reach an ordered state, and that was the case in the present study [10]. One possible approach would be to prefabricate a spherical crystal film first and then deform it into a discoid crystal film [11], [12]. We therefore propose that the following procedures could be used to combine evaporative assembly and discoid synthesis methods: polystyrene (PS) colloidal microspheres are first assembled into spherical crystals onto a glass substrate by the evaporative assembly. The crystal structure is locked using binding proteins such as streptavidin to cross-link neighboring particles. Then the spherical crystal would be infiltrated with an aqueous polyvinyl alcohol (PVA) solution. After water evaporated, a PS/PVA composite film would be obtained. Peeling off the film from the substrate may only take one layer of particles. To create a 3D structure, multiple composite films could be stacked together. The composite films would be pressed with heat above the glass transition temperatures of PS and PVA, and sphere particles in the films would be deformed into discoids. Discoid structures in the PVA matrix do not generate a strong structural color because the refractive contrast of PS and PVA is small, so the PVA matrix would need to be removed. By carefully dissolving the PVA matrix in the mixture of isopropyl alcohol and water, ordered discoid structures could be obtained, but they may be collapsed into

small crystals. After confirming their structural color properties, those discoid fragments would be of interest for applications involving structural color pigments.

5.1 References

[1] A. A. Shah, M. Ganesan, J. Jocz, and M. J. Solomon, "Direct Current Electric Field Assembly of Colloidal Crystals Displaying Reversible Structural Color," *ACS Nano*, vol. 8, no. 8, pp. 8095–8103, Aug. 2014.

[2] W. Wang *et al.*, "Large-scale preparation of size-controlled Fe 3 O 4 @SiO 2 particles for electrophoretic display with non-iridescent structural colors," *RSC Adv.*, vol. 9, no. 1, pp. 498–506, Jan. 2019.

[3] B. Lange *et al.*, "Functional polymer-opals from core-shell colloids," *Macromol. Rapid Commun.*, vol. 28, no. 20, pp. 1987–1994, Oct. 2007.

[4] † Jonathan G. McGrath, ‡ Robert D. Bock, ‡ and J. Michael Cathcart, and † L. Andrew Lyon*, "Self-Assembly of 'Paint-On' Colloidal Crystals Using Poly(styrene-co-N-isopropylacrylamide) Spheres," 2007.

[5] X. Chen *et al.*, "Fabrication of closed-cell polyimide inverse opal photonic crystals with excellent mechanical properties and thermal stability," *J. Mater. Chem.*, vol. 18, no. 19, pp. 2262–2267, Apr. 2008.

[6] T. Ruhl and G. P. Hellmann, "Colloidal Crystals in Latex Films: Rubbery Opals."

[7] J. Wang *et al.*, "Simple fabrication of full color colloidal crystal films with tough mechanical strength," *Macromol. Chem. Phys.*, vol. 207, no. 6, pp. 596–604, Mar. 2006.

[8] B. You, N. Wen, L. Shi, L. Wu, and J. Zi, "Facile fabrication of a three-dimensional

colloidal crystal film with large-area and robust mechanical properties," *J. Mater. Chem.*, vol. 19, no. 22, pp. 3594–3597, Jun. 2009.

[9] C. J. R. Sheppard, "Approximate calculation of the reflection coefficient from a stratified medium," *Pure Appl. Opt. J. Eur. Opt. Soc. Part A*, vol. 4, no. 5, pp. 665–669, Sep. 1995.

[10] I. D. Hosein and C. M. Liddell, "Convectively assembled asymmetric dimer based colloidal crystals," *Langmuir*, vol. 23, no. 25, pp. 10479–10485, 2007.

[11] P. P. Lele and E. M. Furst, "Assemble-and-stretch method for creating two- and three-dimensional structures of anisotropic particles," *Langmuir*, vol. 25, no. 16, pp. 8875–8878, Aug. 2009.

[12] T. Ding, Z. F. Liu, K. Song, K. Clays, and C. H. Tung, "Photonic crystals of oblate spheroids by blown film extrusion of prefabricated colloidal crystals," *Langmuir*, vol. 25, no. 17, pp. 10218–10222, 2009.